

VIBRATION SUPPRESSION IN SIMPLE TENSION-ALIGNED STRUCTURES

By

Tingli Cai

A DISSERTATION

Submitted
to Michigan State University
in partial fulfillment of the requirements
for the degree of

Mechanical Engineering – Doctor of Philosophy

2016

ABSTRACT

VIBRATION SUPPRESSION IN SIMPLE TENSION-ALIGNED STRUCTURES

By

Tingli Cai

Tension-aligned structures have been proposed for space-based antenna applications that require high degree of accuracy. This type of structures use compression members to impart tension on the antenna, thus helping to maintain the shape and facilitate disturbance rejection. These structures can be very large and therefore sensitive to low-frequency excitations. In this study, two control strategies are proposed for the purpose of vibration suppression. First, a semi-active control strategy for tension-aligned structures is proposed, based on the concept of stiffness variation by sequential application and removal of constraints. The process funnels vibration energy from low-frequency to high-frequency modes of the structure, where it is dissipated naturally due to internal damping. In this strategy, two methods of stiffness variation were investigated, including: 1) variable stiffness hinges in the panels and 2) variable stiffness elastic bars connecting the panels to the support structure. Two-dimensional and three-dimensional models were built to demonstrate the effectiveness of the control strategy. The second control strategy proposed is an active scheme which uses sensor feedback to do negative work on the system and to suppress vibration. In particular, it employs a sliding mechanism where the constraint force is measured in real time and this information is used as feedback to prescribe the motion of the slider in such a way that the vibration energy is reduced from the structure continuously and directly. The investigation of the sliding mechanism was performed numerically using the model of a nonlinear beam. Practical issues of this control scheme have been considered and measures such as adding a low-pass filter was taken to ease requirements on the control hardware. It has been shown in simulations that these two control strategies are effective mechanisms to remove energy from a vibrating system.

To validate the control strategies, an experimental setup was built. A 3.66 meter long aluminum beam was placed on a rigid bench with a tension device applied at one end. A belt-driven actuator

carried a slider, which moved axially along the surface of the beam. On the sliding interface, the slider imposed a constraint on the beam to maintain zero transverse displacement. Rotation at the sliding contact point, controlled by an electromagnetic brake, could be fixed instantaneously, or allowed to vary freely. The slider was equipped with strain gauges and an encoder to measure the constraint force from the beam. The sensor data was fed back and processed in real-time by a control algorithm implemented on a DSP board. Different control strategy combinations have been experimented on the system. Results showed that, with light material damping present in the structure, the two control strategies effectively redistributed the vibration energy into the high-frequency modes, where it was dissipated naturally and quickly.

Copyright by
TINGLI CAI
2016

ACKNOWLEDGEMENTS

I would like to express my deepest appreciation to the two dear advisors of mine, Dr. Ranjan Mukherjee and Dr. Alejandro R. Diaz.

TABLE OF CONTENTS

LIST OF TABLES	ix
LIST OF FIGURES	x
CHAPTER 1 INTRODUCTION TO TENSION-ALIGNED STRUCTURES	1
CHAPTER 2 VIBRATION SUPPRESSION THROUGH STIFFNESS VARIATION	5
2.1 A two-DOF illustrative example	5
2.2 Stiffness variation in multi-DOF systems	9
2.3 Model of a two-dimensional simple tension-aligned structure	13
2.3.1 Nonlinear dynamic model of the support structure	13
2.3.2 Static equilibrium configuration of the support structure	15
2.3.3 Linear dynamic model of the support structure	16
2.3.4 Hinged panel array model	19
2.3.5 Methods of stiffness variation	20
2.3.6 Numerical simulation	21
2.4 Model of a three-dimensional tension-aligned structure	26
CHAPTER 3 VIBRATION SUPPRESSION USING A SLIDING MECHANISM	29
3.1 Sliding mechanism description	29
3.2 Equations of motion for a nonlinear beam with a fixed slider	30
3.3 Numeric simulation of the sliding mechanism of a nonlinear beam	34
3.3.1 Finite element discretization using adaptive mesh	34
3.3.2 Numeric issue of computing the constraint force: Lagrange multiplier vs. penalty method	40
3.4 Feedback control design of the slider motion	41

3.4.1	Preliminary design of the slider motion control	41
3.4.2	Modified control design	44
3.5	Combining slider motion with stiffness variation	47
3.5.1	Simulation of the system undergoing free vibration	48
3.5.2	Simulation of the system employing sliding control only	53
3.5.3	Simulation of the system employing sliding control combined with stiff- ness variation	56
CHAPTER 4	EXPERIMENTAL STUDY OF VIBRATION SUPPRESSION THROUGH STIFFNESS VARIATION AND SLIDING MECHANISM	63
4.1	Experiment design	63
4.1.1	Tension-aligned structure	63
4.1.2	Stiffness variation mechanism	64
4.1.3	Sliding mechanism	65
4.2	Experiment implementation	65
4.2.1	A nonlinear beam	65
4.2.2	Added mass	66
4.2.3	Tension device	66
4.2.4	Sliding motion control	67
4.2.5	Rotational on/off mechanism	68
4.2.6	Slider contact interface	68
4.2.7	Measurement for feedback information and the system status	69
4.2.8	Data acquisition	70
4.2.9	Real-time control and data processing algorithm	71
4.2.10	Initial displacement holder	71
4.2.11	Complete system	72
4.3	Experiment results	72

4.3.1	Free vibration	72
4.3.2	Performance of control employing sliding mechanism only	79
4.3.3	Performance of control employing stiffness variation mechanism only . . .	82
4.3.4	Performance of control combining stiffness variation and sliding mechanism	85
4.3.5	Discussion	89
CHAPTER 5 SUMMARY AND FUTURE WORK		91
BIBLIOGRAPHY		94

LIST OF TABLES

Table 2.1	Parameters used in the 2-DOF simulations	6
Table 2.2	Properties of Simulated Tension-Aligned Structure	22
Table 2.3	First six natural frequencies of the unconstrained and the constrained tension-aligned structure in rad/s.	24
Table 3.1	Properties and geometry of the simulated beam with a sliding constraint.	38
Table 3.2	Properties, geometry and other parameters of the beam system used in the validation simulation.	48
Table 3.3	Comparison of performance of different control strategies. All relative displacements and accelerations are computed using the mass 1 initial status as reference.	62
Table 4.1	Properties and geometry of the beam used in experiment.	66
Table 4.2	Comparison of performance of different control strategies. All relative values were computed using the mass 1 initial acceleration as reference.	89

LIST OF FIGURES

Figure 1.1	A tension-aligned structure comprised of a support structure and a sensor surface - taken from Jones et al. Jones et al. (2008).	2
Figure 2.1	A two degree-of-freedom mass-spring-damper system.	5
Figure 2.2	Total energy and displacements of the Unconstrained system - (a), (b); Total energy and displacements of the Constrained system - (c), (d)	7
Figure 2.3	Switched system: (a) Total energy; (b) energy associated with the low-frequency mode(s); (c) energy associated with the high-frequency mode; (d) displacements of the masses; (e), (f) modal displacements. In all of these figures, "uc" and "c" denote the unconstrained and constrained states of the system. A magnified view of the modal displacement is shown in the constrained states.	8
Figure 2.4	Vibration suppression through energy funneling from low-frequency modes (LFM) into high-frequency modes (HFM).	11
Figure 2.5	A tension-aligned structure formed by connecting a support structure (in compression) to an array of hinged panels (in tension).	12
Figure 2.6	A planar elastica arch	13
Figure 2.7	The array of hinged panels	20
Figure 2.8	Stiffness variation in the tension-aligned structure is realized using two methods: (A) and (B); these are described in section 3.4.	20
Figure 2.9	The eight-panel tension-aligned structure used in simulations.	21

Figure 2.10	Plot of energy for the three cases discussed in Section 4.2.	23
Figure 2.11	Plot of energy for the three cases simulated.	25
Figure 2.12	Plots of the transverse displacements of three points on the hinged panel array (see Fig.2.9), in the case of methods (A) and (B) combined.	26
Figure 2.13	Overview of the tension-aligned three-dimensional structure. 8 panels are connected using 7 hinges and supported by a truss structure.	26
Figure 2.14	Geometry of the three-dimensional structure.	27
Figure 2.15	Plot of energy for cases of controlling different number of joints.	28
Figure 3.1	A pinned-pinned beam with a sliding constraint.	30
Figure 3.2	Plots of the system in free vibration: normalized energy; transverse displacement sampled at $S = 0.75$ or $s = 2.743$ m; material coordinate of the point Q in contact with the slider; constraint force in transverse direction; constraint force in axial direction.	39
Figure 3.3	Preliminary feedback control design.	43
Figure 3.4	Plots of the system applied with direct control: normalized energy of the direct control results in solid line, normalized energy of free vibration in dashed line as reference; transverse displacement sampled at $S = 0.75$ or $s = 2.743$ m; slider position; slider velocity; constraint force in horizontal direction.	44
Figure 3.5	Modified control design with filter.	45

Figure 3.6	Plots of the system applied with direct control: normalized energy of the modified control results in solid line, normalized energy of free vibration in dashed line as reference, normalized energy of the direct control results in dotted-solid line as reference; transverse displacement sampled at $S = 0.75$ or $s = 2.743$ m; slider position; slider velocity; constraint force in horizontal direction after the low-pass filter.	46
Figure 3.7	Simulation of the system under free vibration (time domain). Plots from top to bottom: axial force evaluated on the slider, applied by the beam; slider slope, or rotational displacement; slider position, measured from left end of the beam; displacement of mass 1; displacement of mass 2.	50
Figure 3.8	Simulation of the system under free vibration (frequency domain). Plots from top to bottom: axial force evaluated on the slider, applied by the beam; slider slope, or rotational displacement; displacement of mass 1; displacement of mass 2.	51
Figure 3.9	Simulation of the mass accelerations under free vibration.	52
Figure 3.10	Simulation of the system energy under free vibration.	53
Figure 3.11	Simulation of the system under sliding control only. Plots from top to bottom: axial force measured on the slider, applied by the beam; slider slope, or rotational displacement; slider position, measured from left end of the beam; displacement of mass 1; displacement of mass 2.	54
Figure 3.12	Simulation of the system energy under sliding control only. Solid line shows the total energy of the beam system. Dashed line represents the energy change directly due to the sliding motion.	55

Figure 3.13	Simulation of the system under combined control of stiffness variation and forward sliding mechanism. Plots from top to bottom: axial force measured on the slider, applied by the beam; slider slope, or rotational displacement; slider position, measured from left end of the beam; displacement of mass 1; displacement of mass 2.	57
Figure 3.14	Simulation of the system energy under combined control of stiffness variation and forward sliding mechanism. Solid line shows the total energy of the beam system. Dashed line represents the energy change directly due to the sliding motion.	58
Figure 3.15	Simulation of the system under combined control of stiffness variation and reverse sliding mechanism.	59
Figure 3.16	Simulation of the system energy under combined control of stiffness variation and reverse sliding mechanism. Solid line shows the total energy of the beam system. Dashed line represents the energy change directly due to the sliding motion.	61
Figure 4.1	Belt drive actuator to provide sliding motion.	67
Figure 4.2	The slider carriage that consists of rotational on/off mechanism and encoder to measure the rotation. A slider shaft is to be assembled on to the carriage. . .	68
Figure 4.3	Slider contact interface with force sensors.	69
Figure 4.4	Assembled parts of sliding and rotational mechanism fixed on the support table in contact with the vibrating beam.	70
Figure 4.5	Interface of the real-time control and data processing software.	71

Figure 4.6	Complete experiment system built after design implementation.	72
Figure 4.7	Experiment results of the system in free vibration (time domain). Plots from top to bottom: total force measured on the slider, applied by the beam; slider slope, or rotational displacement; slider position, measured from left end of the beam; acceleration of mass 1; acceleration of mass 2.	73
Figure 4.8	Experiment results of the system in free vibration (frequency domain). Plots from top to bottom: total force measured on the slider, applied by the beam; slider slope, or rotational displacement; acceleration of mass 1; acceleration of mass 2.	75
Figure 4.9	Axial force on slider, post-processed from experiment results of the system in free vibration (time domain).	76
Figure 4.10	Axial force on slider, post-processed from experiment results of the system in free vibration (frequency domain).	77
Figure 4.11	Experiment results of the system under sliding control only. Plots from top to bottom: total force measured on the slider, applied by the beam; slider slope, or rotational displacement; slider position, measured from left end of the beam; acceleration of mass 1; acceleration of mass 2.	78
Figure 4.12	Axial force on slider in time domain, processed from measurements of total force on slider and slider slope	80
Figure 4.13	Slider velocity in time domain, processed from the measurement of slider position.	80
Figure 4.14	Axial force on slider in frequency domain.	82

Figure 4.15	Slider velocity in frequency domain.	83
Figure 4.16	Experiment results of the system under stiffness variation control only. Plots from top to bottom: total force measured on the slider, applied by the beam; slider slope, or rotational displacement; slider position, measured from left end of the beam; acceleration of mass 1; acceleration of mass 2.	84
Figure 4.17	Experiment results of the system under combined control of stiffness variation and forward sliding mechanism. Plots from top to bottom: total force measured on the slider, applied by the beam; slider slope, or rotational displacement; slider position, measured from left end of the beam; acceleration of mass 1; acceleration of mass 2.	86
Figure 4.18	Experiment results of the system under combined control of stiffness variation and reverse sliding mechanism. Plots from top to bottom: total force measured on the slider, applied by the beam; slider slope, or rotational displacement; slider position, measured from left end of the beam; acceleration of mass 1; acceleration of mass 2.	88

CHAPTER 1

INTRODUCTION TO TENSION-ALIGNED STRUCTURES

Large space structures are contemplated for use as space-based radars for imaging and moving object identification and tracking. These radars consist of a large support structure and phased array antennas attached to this structure. The complete system has to be designed so that it can be folded into a compact volume for ease of transport, and so that the phased array antennas can maintain a high degree of accuracy after deployment. A high degree of accuracy is difficult to achieve since these structures are large and sensitive to disturbances that result in vibration. The structure can be modelled and its deformations can be measured and corrected using sensors and actuators in real time, but such systems are extremely challenging to engineer. This is because these structures are designed with numerous and complex joints and mechanisms for folding that introduce nonlinearities such as slipping, backlash and deadband. Model-based control also requires development and identification of a high-dimensional mathematical model that accounts for the nonlinearities and the integration of significant control system hardware into the structure. Vibration suppression in large space structures is a challenging problem and a practical solution needs passive or semi-active control, or an active control scheme using just few sensors and actuators.

To meet the precision requirements of space-based radars, tension-aligned structures have been proposed by Mikulas et al. (2008) and Jones et al. (2008). Similar to a bow with a string, in a tension-aligned structure, the array antennas are attached to the support structure via tensioners at each end (see Fig.1.1); the support structure is used as a compression member to impart tension to the array antennas pinned at each end. The tension in the antenna array helps maintain flatness but, more importantly, increases the stiffness of the array, which is necessary for disturbance rejection (Adler et al., 1998). Other benefits of tension-aligned structures include elimination of the high dimensional accuracy requirements of the support structure, greater flexibility in design (since the support structure and the array antennas can be separately packaged and deployed), and reduced

effect of nonlinearities such as deadband and backlash (Jones et al., 2008); compensation for creep and manufacturing tolerance build-up (Winslow, 1993); and increase in structural damping (Fang & Lyons, 1996) which facilitates vibration suppression. The tension-aligned architecture is equally well-suited for radar designs where the antennas are an array of panels or a flexible membrane (Kemerley & Kiss, 2000; Jeon & Murphey, 2012; Footdale et al., 2012).

To investigate the feasibility of tension-aligned architectures, Jones et al. (2008), Jones et al. (2007) studied the effect of tension on the stiffness of a large aperture antenna. Using the DARPA ISAT¹ as the representative platform, nonlinear finite-element methods were used to compute the system frequencies with sensor surfaces ranging from gossamers to paneled radars. For a free-free support structure, it was shown that it is not possible to find a tension/mass ratio combination that yields a higher or even equivalent peak frequency to that of the structure. This implies that the addition of the sensor surface will only reduce the fundamental frequency of the overall system. This problem can be alleviated by introducing a load offset such that tension adds bending moments on the support structure. However, a load offset increases the deformation of the support structure

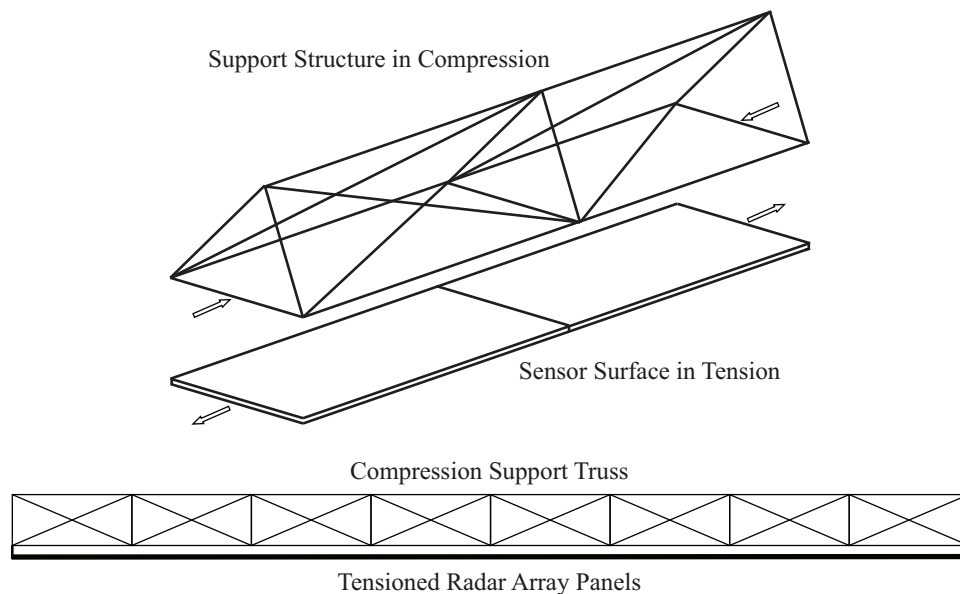


Figure 1.1 A tension-aligned structure comprised of a support structure and a sensor surface - taken from Jones et al. Jones et al. (2008).

¹Innovative Space-based radar Antenna Technology

and the tension required to achieve the same fundamental frequency of ISAT is close to the buckling load. To eliminate problems related to buckling and large deformation, Jones et al. (2008) proposed to introduce intermediate connectors and guy-wires to provide counter-tension.

The tension-aligned architecture proposed by Jones et al. (2008) can be viewed as a passive method for vibration suppression where the location of the intermediate connectors and internal stress in the structure are optimized to attain the same level of structural stiffness as the ISAT platform. This may not be sufficient for meeting the high accuracy requirements of space-based radars since space structures such as the ISAT platform are large and prone to low-frequency excitation. The tension required to achieve the desired level of stiffness is also high and may not be suitable for long-term operation.

To address these challenges, two control strategies for tension-aligned structures are proposed in this paper. Strategy 1 is based on the concept of stiffness variation. This method applies and removes constraints cyclically such that vibration energy is funneled into the high-frequency modes of the structure, where it can be dissipated quickly and naturally due to high rates of internal damping. Strategy 2 employs a slider mechanism which applies moving loads on the surface of the structure. There is a constraint force on the structure applied by the slider. Using this measured constraint force as feedback, the motion of the slider is prescribed such that it does negative work on the controlled structure and vibration therefore is suppressed. Both control strategies require fewer sensors and actuators and eliminates the need for extensive computations based on a mathematical model of the structure, compared to traditional active control, which relies on accurate measurement by sensors, careful compensation by actuators and detailed mathematical modelling of the control system.

Several researchers (Onoda et al., 1991, 1992; Clark, 2000; Corr & Clark, 2001; Ramaratnam & Jalili, 2006) have explored stiffness variation as a method for vibration suppression. In all these works, variable-stiffness elements are placed in a state of high stiffness and energy is stored in them. Once the stored energy reaches a maximum value, the stiffness of the element is switched to a low value to dissipate energy. In the work of Diaz & Mukherjee (2006b, 2008); Issa et al.

(2009), stiffness variation was achieved through application and removal of constraints; and energy dissipation was accomplished through a targeted and purposeful energy redistribution from low-frequency modes to high-frequency modes. This thesis extended those work to a simple tension-aligned structure.

Sliding mechanism in the form of constraints in flexible structures has been investigated by many researchers, especially in areas such as contact mechanics and flexible multibody dynamics, for example in research by Barhorst (2004); Hong & Ren (2011). There are also studies where constraint forces are used to determine the states of the system Sakamoto & Park (2006). However, the idea of directly manipulating the constraint force to reduce system energy has not been proposed. Such an idea is developed in this thesis into a method that is implementable in tension-aligned structures.

The plan of this thesis is as follows. Chapter 2 introduces the control strategy using stiffness variation for application in multi-dof linear systems and define a “modal disparity index”, a metric that can be used to determine the efficacy of our control strategy. Both two-dimensional and three-dimensional models are presented. Chapter 3 considers the sliding mechanism on a nonlinear beam. After modelling the structure and solving for the constraint force, the control scheme was formulated and verified numerically. Chapter 4 presents the experimental study of the two proposed vibration suppression strategies. Chapter 5 summarizes the two methods in different application condition and propose the work to be done as the next step.

CHAPTER 2

VIBRATION SUPPRESSION THROUGH STIFFNESS VARIATION

2.1 A two-DOF illustrative example

Consider the two degree-of-freedom mass-spring-damper system in Fig.2.1. The two masses m_1 and m_2 are connected to fixed supports by springs of stiffness k_1 and k_2 , and to each other by the spring of time-varying stiffness $k_3(t)$. The displacements of the two masses are denoted by x_1 and x_2 and the springs are undeformed when the masses are in their equilibrium configuration, *i.e.*, $x_1 = x_2 = 0$. We assume $(k_1/m_1) \neq (k_2/m_2)$ such that the two masses have different natural frequencies when $k_3(t) = 0$. The equation of motion of the two degree-of-freedom system is given below

$$\begin{bmatrix} m_1 & 0 \\ 0 & m_2 \end{bmatrix} \begin{bmatrix} \ddot{x}_1 \\ \ddot{x}_2 \end{bmatrix} + \begin{bmatrix} k_1 + k_3(t) & -k_3(t) \\ -k_3(t) & k_2 + k_3(t) \end{bmatrix} \begin{bmatrix} x_1 \\ x_2 \end{bmatrix} = \begin{bmatrix} 0 \\ 0 \end{bmatrix} \quad (2.1)$$

Now consider three cases where the stiffness $k_3(t)$ is chosen differently

$$\text{Unconstrained} : k_3(t) = 0$$

$$\text{Constrained} : k_3(t) = k_r$$

$$\text{Switched} : k_3(t) = \begin{cases} 0 & \text{if } t \in [t_i, t_{i+1}) \\ k_r & \text{if } t \in [t_{i+1}, t_{i+2}) \end{cases}, \quad i = 0, 2, 4, \dots \quad (2.2)$$

It is assumed that k_r is large compared to k_1 and k_2 , and times t_n , $n = 0, 1, 2, \dots$, are chosen such that $x_2(t_n) - x_1(t_n) = 0$. This ensures that no energy is removed from the system when the

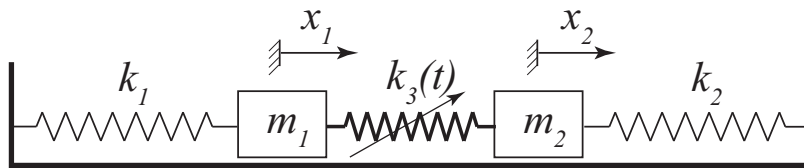


Figure 2.1 A two degree-of-freedom mass-spring-damper system.

stiffness is switched from k_r to 0, or added to the system when the stiffness is switched from 0 to k_r . Assuming modal damping with uniform damping ratio ζ , the equation of motion of the system can be written in modal coordinates as follows:

$$\begin{bmatrix} \ddot{q}_1 \\ \ddot{q}_2 \end{bmatrix} + 2\zeta \begin{bmatrix} \Omega_1(t) & 0 \\ 0 & \Omega_2(t) \end{bmatrix} \begin{bmatrix} \dot{q}_1 \\ \dot{q}_2 \end{bmatrix} + \begin{bmatrix} \Omega_1^2(t) & 0 \\ 0 & \Omega_2^2(t) \end{bmatrix} \begin{bmatrix} q_1 \\ q_2 \end{bmatrix} = \begin{bmatrix} 0 \\ 0 \end{bmatrix} \quad (2.3)$$

where q_1 and q_2 are the modal coordinates, and $\Omega_j(t)$, $j = 1, 2$, are the natural frequencies of the system. For the three different cases, the natural frequencies are denoted as follows:

$$\begin{aligned} \text{Unconstrained} & : \Omega_j(t) = \omega_j \\ \text{Constrained} & : \Omega_j(t) = \bar{\omega}_j \\ \text{Switched} & : \Omega_j(t) = \begin{cases} \omega_j & \text{if } t \in [t_i, t_{i+1}) \\ \bar{\omega}_j & \text{if } t \in [t_{i+1}, t_{i+2}) \end{cases}, \quad i = 0, 2, 4, \dots \end{aligned} \quad (2.4)$$

where $\omega_j = \sqrt{k_j/m_j}$, $j = 1, 2$. The expressions for $\bar{\omega}_j$ are complicated and are not provided here.

Table 2.1 Parameters used in the 2-DOF simulations

m_1 (kg)	m_2 (kg)	k_1 (N/m)	k_2 (N/m)	k_r (N/m)	ζ
1.00	2.00	2.00	2.00	20000	0.001

Simulations were performed for the three cases discussed above, using parameters in Table 2.1 and the same set of initial conditions. The natural frequencies of the Unconstrained and Constrained systems were found to be

$$(\omega_1, \omega_2) = (1.4142, 1.0000), \quad (\bar{\omega}_1, \bar{\omega}_2) = (1.1547, 1.7321 \times 10^2) \quad (2.5)$$

where the units are rad/s. One of the frequencies for the Constrained system was high relative to the other natural frequencies. This frequency was associated with the relative motion of the two masses, when they were connected by the stiff spring k_r .

The simulation results are shown in Figs.2.2 and 2.3. The total energy and the displacements of the Unconstrained and Constrained systems are shown in Fig.2.2. For the Unconstrained system,

the total energy of the system decayed very slowly; only 10.5% was dissipated in 42.7 s. This is because of low internal damping associated with low natural frequencies of the system. For the Constrained system, the total energy decayed rapidly initially, but slowly thereafter; 35.9% was dissipated in 42.7 s. One natural frequency of the Constrained system was high and rapid decay of the energy associated with this mode contributed to the initial rapid decay of the total energy. The displacements of the two masses of the Constrained system appeared to be identical. This is because of small relative motion of the masses, a consequence of high stiffness of the spring connecting them.

For both the Unconstrained and the Constrained systems in Fig.2.2, a small fraction of the energy was dissipated. In contrast, the energy of the Switched system (see Fig.2.3) decayed significantly faster; 83.4% was dissipated in 42.7 s. For the Switched system, the two masses were initially unconstrained. They were connected (constrained) by the spring at $t_1 = 11.24$ s, released (unconstrained) at $t_2 = 21.25$ s, and again connected at $t_3 = 32.70$ s. As mentioned earlier, t_1 , t_2 and t_3 were chosen such that no energy was added to or subtracted from the system during the process of application or removal of the constraint (stiffness switching). At $t = t_1$ and $t = t_3$, appli-

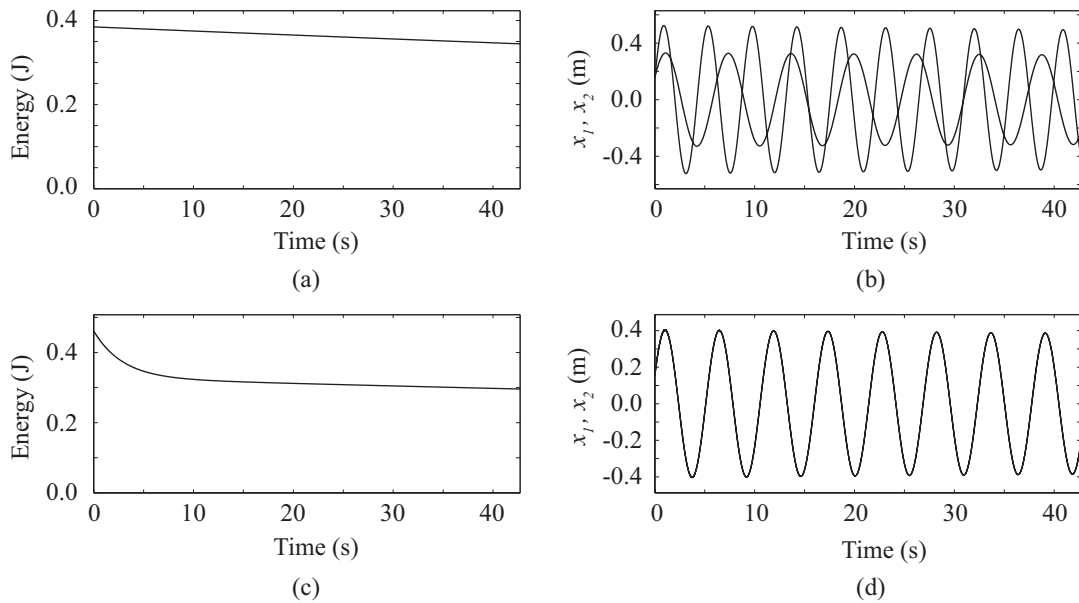


Figure 2.2 Total energy and displacements of the Unconstrained system - (a), (b); Total energy and displacements of the Constrained system - (c), (d)

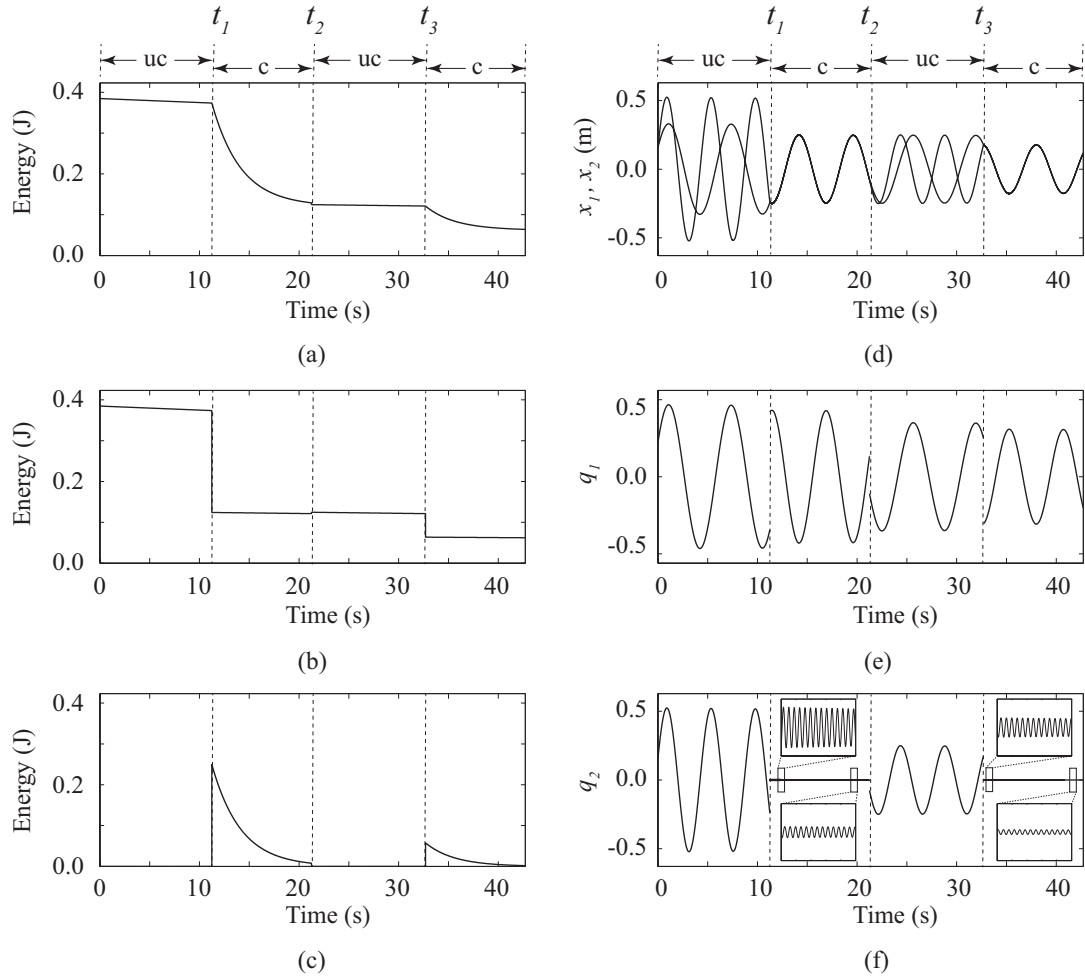


Figure 2.3 Switched system: (a) Total energy; (b) energy associated with the low-frequency mode(s); (c) energy associated with the high-frequency mode; (d) displacements of the masses; (e), (f) modal displacements. In all of these figures, “uc” and “c” denote the unconstrained and constrained states of the system. A magnified view of the modal displacement is shown in the constrained states.

cation of the constraint created a high-frequency mode and funneled energy into this mode, where it was dissipated quickly; this can be verified from the energy plots of the low- and high-frequency modes. As in the case of the Constrained system in Fig.2.2, the displacement plots of the two masses for the Switched system appear to be identical when they were constrained by the spring. The plots of the modal coordinates show discontinuities at the times of constraint application and removal. This is because the modal coordinates have different functional descriptions in the constrained and unconstrained states. In the constrained state, the high-frequency mode had a small

amplitude (q_2 in Fig.2.3), but its energy content was significant. This energy decayed rapidly each time after the system was switched from the unconstrained state to the constrained state. This can be seen from the magnified views of q_2 in the time interval $[t_1, t_2]$, and again in the interval $[t_3, 42.7]$. A comparison of the magnified views of q_2 in the intervals $[t_1, t_2]$ and $[t_3, 42.7]$ also confirms that switching resulted in funneling of energy into the high-frequency mode.

The example above illustrates that energy dissipation is faster in systems with switched stiffness than in systems with constant stiffness in the presence of modal damping. The faster rate of dissipation is not due to direct removal of energy by the action of switching, but due to funneling of energy into the high-frequency modes of the system. The ease with which energy can be funneled from the low-frequency modes to the high-frequency modes is discussed in the next section for a general multi-degree-of-freedom linear system.

2.2 Stiffness variation in multi-DOF systems

Consider the N -DOF linear system

$$\mathbb{M}\ddot{X} + \mathbb{K}(t)X = 0 \quad (2.6)$$

where $X = (x_1, x_2, \dots, x_N)^T$ denotes the vector of generalized coordinates, \mathbb{M} denotes the mass matrix, and $\mathbb{K}(t)$ denotes the stiffness matrix. The stiffness matrix $\mathbb{K}(t)$ consists of a constant stiffness matrix \mathbb{K}_0 and a time-varying stiffness matrix $\Delta\mathbb{K}(t)$ as follows:

$$\mathbb{K}(t) = \mathbb{K}_0 + \Delta\mathbb{K}(t), \quad \Delta\mathbb{K}(t) = \begin{cases} 0 & \text{if } t \in [t_i, t_{i+1}) \\ K_r & \text{if } t \in [t_{i+1}, t_{i+2}) \end{cases}, \quad i = 0, 2, 4, \dots \quad (2.7)$$

where K_r is the change in the stiffness matrix due to the addition of springs connecting pairs of generalized coordinates. In the simplest case where a single spring is used to connect a pair of generalized coordinates x_m and x_n , the entries of $K_r \in \mathbb{R}^{N \times N}$ can be obtained from the Hessian of

the additional strain energy $(1/2)k_r(x_m - x_n)^2$

$$K_r(i, j) = \begin{cases} k_r & \text{if } (i, j) = (m, m) \text{ or } (n, n) \\ -k_r & \text{if } (i, j) = (m, n) \text{ or } (n, m) \\ 0 & \text{otherwise} \end{cases} \quad m \neq n \quad (2.8)$$

where k_r is the stiffness of the spring, which is large compared to the magnitude of the entries of \mathbb{K}_0 .

In Eq.(2.7), $t_j, j = 0, 1, 2, \dots$, are chosen such that the change in stiffness does increase the total energy of the system. This is assured by choosing the time t_j when switching $\Delta\mathbb{K}(t_j)$ from 0 to K_r (stiffness increase) such that all the relevant relative displacements are zero. In the simplest case mentioned above, where a single spring is used, t_j is chosen to switch $\Delta\mathbb{K}(t_j)$ from 0 to K_r (stiffness increase) such that $x_m(t_j) - x_n(t_j) = 0$. When $\Delta\mathbb{K}(t_j)$ is switched from K_r to 0 (stiffness decrease), t_j can be arbitrary. In this process of stiffness decrease, there might be direct and instantaneous loss of energy due to the fact that relative displacement is usually nonzero given arbitrary t_j . This direct energy loss only favorably reduces the energy of the system.

Let ϕ_i and $\mu_i, i = 1, 2, \dots, N$, denote the linearly independent orthogonal mode shapes and the corresponding modal coordinates in the unconstrained state. Similarly, let ψ_i and $v_i, i = 1, 2, \dots, N$, denote the linearly independent orthogonal mode shapes and the corresponding modal coordinates in the constrained state. At the time of application of the constraint ($\Delta\mathbb{K}$ changes from 0 to K_r), the generalized coordinates and their velocities can be expressed as follows:

$$X(t_{i+1}) = \begin{cases} \sum_{i=1}^N \mu_i(t_{i+1}) \phi_i = \Phi \mu(t_{i+1}) \\ \sum_{i=1}^N v_i(t_{i+1}) \psi_i = \Psi v(t_{i+1}) \end{cases} \quad i = 0, 2, 4, \dots \quad (2.9)$$

$$\dot{X}(t_{i+1}) = \begin{cases} \sum_{i=1}^N \dot{\mu}_i(t_{i+1}) \phi_i = \Phi \dot{\mu}(t_{i+1}) \\ \sum_{i=1}^N \dot{v}_i(t_{i+1}) \psi_i = \Psi \dot{v}(t_{i+1}) \end{cases} \quad i = 0, 2, 4, \dots \quad (2.10)$$

where $\Phi = [\phi_1, \phi_2, \dots, \phi_N]$ and $\Psi = [\psi_1, \psi_2, \dots, \psi_N]$ are modal matrices in the unconstrained and constrained states respectively. Using Eqs.(2.9) and (2.10), the transition of the system from the

unconstrained state to the constrained state can be described by the relations

$$\mathbf{v}(t_{i+1}) = \Gamma \boldsymbol{\mu}(t_{i+1}), \quad \dot{\mathbf{v}}(t_{i+1}) = \Gamma \dot{\boldsymbol{\mu}}(t_{i+1}), \quad i = 0, 2, 4, \dots \quad (2.11)$$

where Γ is the modal disparity matrix (Diaz & Mukherjee, 2006a; Issa et al., 2008), and is given by the relation

$$\Gamma = \Psi^T \mathbb{M} \Phi \quad (2.12)$$

The transition of the system from the constrained state to the unconstrained state can be similarly described by the relations

$$\boldsymbol{\mu}(t_i) = \Gamma^T \mathbf{v}(t_i), \quad \dot{\boldsymbol{\mu}}(t_i) = \Gamma^T \dot{\mathbf{v}}(t_i), \quad i = 0, 2, 4, \dots \quad (2.13)$$

The transformation matrix Γ is the identity matrix when $K_r = 0$, *i.e.*, when no stiffness variation is introduced. When $K_r \neq 0$, $\Gamma(i, j) \neq 0$ for some values of i and j , $i \neq j$. This implies that energy will be transferred from the j -th mode of the unconstrained state to the i -th mode of the constrained state, and vice versa. If the frequency of the i -th mode of the constrained state is much higher than that of the j -th mode of the unconstrained state, the energy transferred from the low-frequency mode to the high-frequency mode will be quickly dissipated. This follows from the assumption

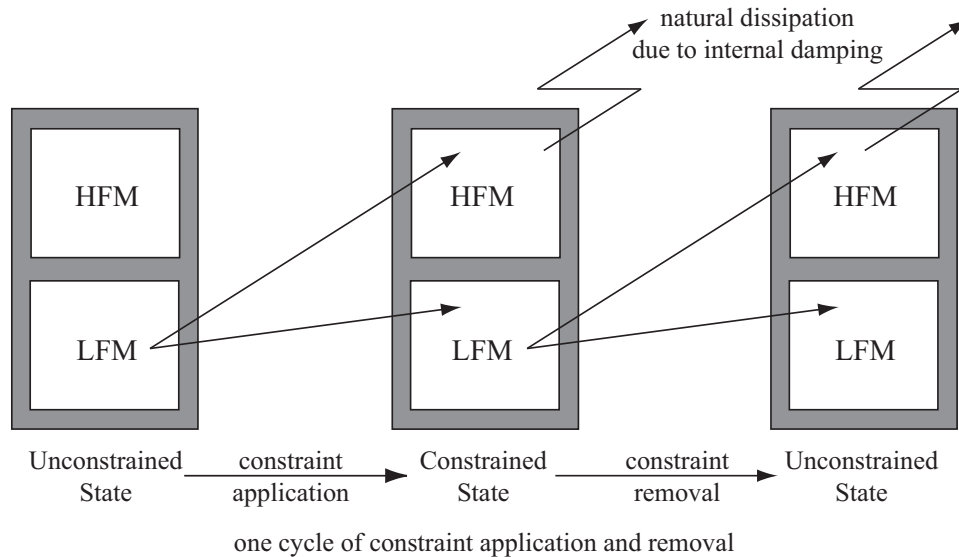


Figure 2.4 Vibration suppression through energy funneling from low-frequency modes (LFM) into high-frequency modes (HFM).

of the modal damping model with the uniform damping ratio. For the process to be repeated, the system has to be switched back from the constrained state to the unconstrained state. To avoid energy flow from the high-frequency modes in one state to the low-frequency modes in the other state, the system should be held in each state sufficiently long time such that energy in the high-frequency modes is dissipated. This strategy for vibration suppression is explained with the help of Fig.2.4.

The success of vibration suppression using stiffness switching will depend on modal disparity created by the change in stiffness. To quantify modal disparity, we define the metric

$$\lambda = \sum_{i=j+1}^N \sum_{j=1}^{N-1} (i-j) |\gamma_{ij}| \quad (2.14)$$

where $\gamma_{ij} = \Gamma(i, j)$ is the (i, j) -th entry of the modal disparity matrix Γ . This metric is a weighted sum of the projections of the low-frequency modes in the unconstrained state onto high-frequency modes in the constrained state and the weights are the difference of the indices of the modes in the two states. This metric will be used to determine better location of constraints in a simple tension-aligned structure, modeled and simulated in the following subsections.

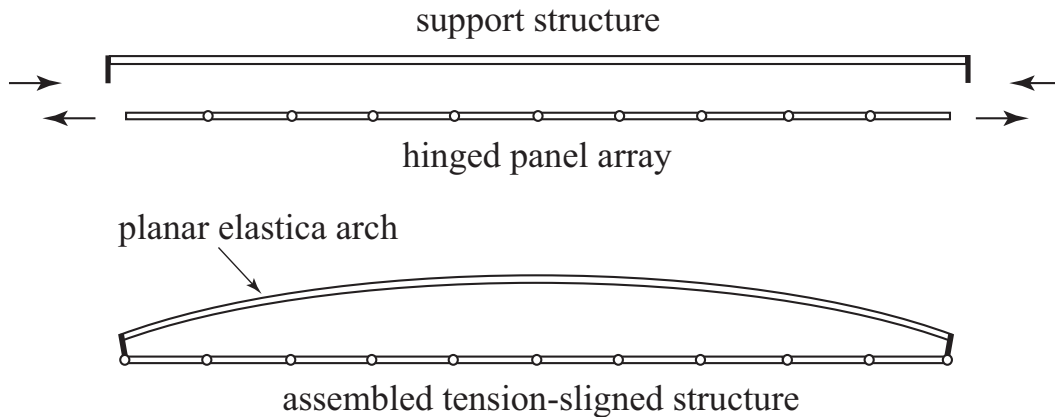


Figure 2.5 A tension-aligned structure formed by connecting a support structure (in compression) to an array of hinged panels (in tension).

2.3 Model of a two-dimensional simple tension-aligned structure

In this subsection we present a finite-element model of a two-dimensional tension-aligned structure. The tension-aligned structure, shown in Fig.2.5, consists of a planar elastica arch support structure in compression and a hinged panel array in tension. The planar elastica arch is initially a straight slender rod; it is bent into its curved shape by eccentric end loads that maintain equilibrium with the tension forces in the panels.

2.3.1 Nonlinear dynamic model of the support structure

The dynamic model of the elastica arch is reproduced from the work by Perkins (1990). The elastica arch, shown in Fig.2.6, is assumed to be a slender rod of length L , held in static equilibrium under the horizontal end-load f and moment fd , where d denotes the vertical eccentricity of the end-load f . In a disturbed state, a point on the rod has a displacement of $\vec{u}(s,t)$, where s denotes the arc length along the centerline of the static equilibrium shape, and t denotes time. $\vec{u}(s,t)$ can be decomposed into its tangential component and normal components as follows:

$$\vec{u}(s,t) = u_t(s,t) \hat{e}_t + u_n(s,t) \hat{e}_n$$

where \hat{e}_t and \hat{e}_n are unit vectors along the tangential and normal directions of the static equilibrium shape, shown in Fig.2.6.

We follow Kirchhoff's assumptions for rod deformation (Dill, 1992), which are (i) rod is linearly elastic, (ii) strains are small (although rotations may be large) and cross-sectional dimensions

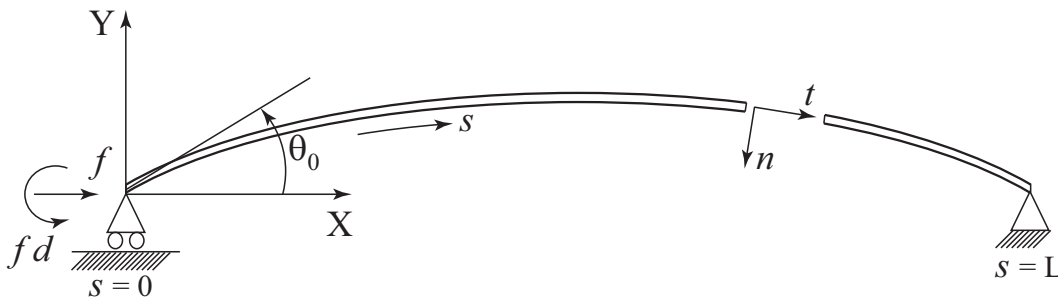


Figure 2.6 A planar elastica arch

of the rod are small compared to its length, (iii) cross-sections remain plane, undistorted and normal to the axis of the rod, and (iv) the transverse stress and rotary inertia can be neglected. Under these assumptions, the kinetic energy and the strain energy of the rod can be expressed as follows:

$$\Pi_T = \frac{1}{2} \int_0^L \rho \left[\left(\frac{\partial u_t}{\partial t} \right)^2 + \left(\frac{\partial u_n}{\partial t} \right)^2 \right] ds \quad (2.15)$$

$$\Pi_V = \frac{1}{2} \int_0^L (EI k^2 + EA e^2) ds \quad (2.16)$$

where ρ , E , A and I are constants and denote the mass per unit length, Young's modulus, cross-sectional area, and area moment of inertia of the rod, respectively. In Eq.(2.16) $k = k(s,t)$ and $e = e(s,t)$ are the curvature and the axial strain. The expression for $k(s,t)$ is obtained from Love (1944) and that of $e(s,t)$ is obtained from Perkins & Mote (1987)

$$k = k_s + \frac{\partial}{\partial s} \left(\frac{\partial u_n}{\partial s} + k_s u_t \right) \quad (2.17)$$

$$e = \frac{p}{EA} = \frac{p_s}{EA} + \frac{\partial u_t}{\partial s} - k_s u_n + \frac{1}{2} \left[\left(\frac{\partial u_t}{\partial s} - k_s u_n \right)^2 + \left(\frac{\partial u_n}{\partial s} + k_s u_t \right)^2 \right] \quad (2.18)$$

where $p = p(s,t)$ is the axial force, and p_s and k_s are the static values of p and k respectively, in the static equilibrium configuration.

The work done by external forces can be expressed as

$$W_{nc} = f (u_t \cos \theta_0 + u_n \sin \theta_0) |_{s=0} + f d \left(\frac{\partial u_n}{\partial s} + k_s u_t \right) \Big|_{s=0}^{s=L} \quad (2.19)$$

where θ_0 is the angle of inclination of the rod at $s = 0$, which will be determined later. Substituting Eqs.(2.17) and (2.18) into Eq.(2.16), neglecting terms that have degree three and higher of variables u_t and u_n , and their spatial derivatives, and using Hamilton's principle

$$\delta \int_{t_1}^{t_2} (\Pi_T - \Pi_V + W_{nc}) dt = 0 \quad (2.20)$$

we get the non-dimensional equations of motion in the normal and tangential directions Perkins (1990)

$$\begin{aligned} -\frac{\partial^3}{\partial S^3} \left(\frac{\partial U_n}{\partial S} + K U_t \right) + \frac{\partial}{\partial S} \left[P \left(\frac{\partial U_n}{\partial S} + K U_t \right) \right] \\ + K \left(P + \frac{1}{I} \right) \left(\frac{\partial U_t}{\partial S} - K U_n \right) - \frac{\partial^2 K}{\partial S^2} + P K = \frac{\partial^2 U_n}{\partial T^2} \end{aligned} \quad (2.21)$$

$$\begin{aligned}
& K \left[\frac{\partial^2}{\partial S^2} \left(\frac{\partial U_n}{\partial S} + K U_t \right) \right] + \frac{\partial}{\partial S} \left[\left(P + \frac{1}{\bar{I}} \right) \left(\frac{\partial U_t}{\partial S} - K U_n \right) \right] \\
& - K P \left(\frac{\partial U_n}{\partial S} + K U_t \right) + K \frac{\partial K}{\partial S} + \frac{\partial P}{\partial S} = \frac{\partial^2 U_t}{\partial T^2}
\end{aligned} \tag{2.22}$$

In the equations above, the non-dimensional variables are defined as follows:

$$\begin{aligned}
S &\triangleq \frac{s}{L}, \quad D \triangleq \frac{d}{L}, \quad U_t \triangleq \frac{u_t}{L}, \quad U_n \triangleq \frac{u_n}{L}, \quad K \triangleq k_s L \\
P &\triangleq \frac{p_s L^2}{EI}, \quad F \triangleq \frac{f L^2}{EI}, \quad \bar{I} \triangleq \frac{I}{A L^2}, \quad T \triangleq \frac{t}{(\rho L^4 / EI)^{1/2}}
\end{aligned} \tag{2.23}$$

Together with the equations of motion, the following boundary conditions are obtained from Hamilton's principle

$$\begin{aligned}
& \left\{ \left[\frac{\partial}{\partial S} \left(\frac{\partial U_n}{\partial S} + K U_t \right) + K - F D \right] \delta \left[\frac{\partial U_n}{\partial S} \right] \right\}_{S=0} \\
& + \left\{ \left[-\frac{\partial}{\partial S} \left[\frac{\partial}{\partial S} \left(\frac{\partial U_n}{\partial S} + K U_t \right) + K \right] + P \left(\frac{\partial U_n}{\partial S} + K U_t \right) + F \sin \theta_0 \right] \delta U_n \right\}_{S=0} \\
& + \left\{ \left[K \left[\frac{\partial}{\partial S} \left(\frac{\partial U_n}{\partial S} + K U_t \right) \right] + K^2 + \left(P + \frac{1}{\bar{I}} \right) \left(\frac{\partial U_t}{\partial S} - K U_n \right) + P - F D K + F \cos \theta_0 \right] \delta U_t \right\}_{S=0} \\
& + \left\{ \left[-\frac{\partial}{\partial S} \left(\frac{\partial U_n}{\partial S} + K U_t \right) - K + F D \right] \delta \left[\frac{\partial U_n}{\partial S} \right] \right\}_{S=1} \\
& + \left\{ \left[\frac{\partial}{\partial S} \left[\frac{\partial}{\partial S} \left(\frac{\partial U_n}{\partial S} + K U_t \right) + K \right] - P \left(\frac{\partial U_n}{\partial S} + K U_t \right) \right] \delta U_n \right\}_{S=1} \\
& + \left\{ \left[-K \left[\frac{\partial}{\partial S} \left(\frac{\partial U_n}{\partial S} + K U_t \right) \right] - K^2 - \left(P + \frac{1}{\bar{I}} \right) \left(\frac{\partial U_t}{\partial S} - K U_n \right) + P + F D K \right] \delta U_t \right\}_{S=1} = 0
\end{aligned} \tag{2.24}$$

2.3.2 Static equilibrium configuration of the support structure

The static equilibrium configuration of the elastica arch depends on the values of f and d , or alternatively, on the non-dimensional variables F and D . For a tension-aligned structure, F and D are design variables; the value of F will depend on the tension desired in the hinged panel array, and the value of D will depend on the stiffness of the slender rod (elastica arch) and the difference in lengths of the hinged panel array and the slender rod. Assuming that the values of F and D are

provided, we determine the static equilibrium configuration by first substituting $U_t = U_n = 0$ in Eqs.(2.21) and (2.22). This yields the following equations:

$$-K'' + KP = 0 \quad (2.25)$$

$$P' + KK' = 0 \quad (2.26)$$

where $(.)'$ denotes the derivative of $(.)$ with respect to S . Substituting $U_t = U_n = 0$ in Eq.(2.24), and using the geometric boundary conditions:

$$\delta U_n(S=1) = 0, \quad \delta U_t(S=1) = 0, \quad \delta U_n(S=0) = \tan \theta_0 \cdot \delta U_t(S=0)$$

we obtain the following natural boundary conditions

$$\begin{aligned} K &= FD & \text{at } S &= 0, 1 \\ F + P \cos \theta_0 - K' \sin \theta_0 &= 0 & \text{at } S &= 0 \end{aligned} \quad (2.27)$$

A closed-form solution to Eqs.(2.25), (2.26) and (2.27) involves elliptic integrals of the first kind and can be found in Perkins (1990). The solutions $K(S)$, $P(S)$, and θ_0 determine the equilibrium configuration and the pre-stress in this configuration.

2.3.3 Linear dynamic model of the support structure

We use the Raleigh-Ritz method Rao (2007) to obtain the linear dynamic model of the elastica arch about its static equilibrium configuration. To write the differential equations, we substitute the equilibrium values of $P = P(S)$ and $K = K(S)$ obtained from the solutions of Eqs.(2.25), (2.26) and (2.27) into Eqs.(2.17) and (2.18), which yields the non-dimensional linear vibration equations

We use the Raleigh-Ritz method Rao (2007) to obtain the linear dynamic model of the elastica arch about its static equilibrium configuration. To write the differential equations, we substitute the equilibrium values of $P = P(S)$ and $K = K(S)$ obtained from the solutions of Eqs.(2.25), (2.26) and (2.27) into Eqs.(2.17) and (2.18), which yields the non-dimensional linear vibration equations

$$-\frac{\partial^3}{\partial S^3} \left(\frac{\partial U_n}{\partial S} + KU_t \right) + \frac{\partial}{\partial S} \left[P \left(\frac{\partial U_n}{\partial S} + KU_t \right) \right] + K \left(P + \frac{1}{I} \right) \left(\frac{\partial U_t}{\partial S} - KU_n \right) = \frac{\partial^2 U_n}{\partial T^2} \quad (2.28)$$

$$K \left[\frac{\partial^2}{\partial S^2} \left(\frac{\partial U_n}{\partial S} + KU_t \right) \right] + \frac{\partial}{\partial S} \left[\left(P + \frac{1}{\bar{I}} \right) \left(\frac{\partial U_t}{\partial S} - KU_n \right) \right] - KP \left(\frac{\partial U_n}{\partial S} + KU_t \right) = \frac{\partial^2 U_t}{\partial T^2} \quad (2.29)$$

To solve Eqs.(2.28) and (2.29), we need to go back to the energy form. To this end, we substitute the equilibrium values of $P = P(S)$ and $K = K(S)$ into the non-dimensional version of Eqs.(2.17) and (2.18), and then substitute the results in the non-dimensional form of the kinetic and strain energies in Eqs.(2.15) and (2.16). Neglecting terms that have degree three and higher of variables U_n and U_t and their spatial derivatives, we have the following expressions for the non-dimensional kinetic and strain energies

$$\begin{aligned} \bar{\Pi}_V = \frac{1}{2} \int_0^1 & \left\{ \overbrace{K^2 + P^2 \bar{I}}^{\text{terms 1 and 2}} + \overbrace{2K \frac{\partial}{\partial S} \left(\frac{\partial U_n}{\partial S} + KU_t \right) + 2P \left(\frac{\partial U_t}{\partial S} - KU_n \right)}^{\text{terms 3 and 4}} \right. \\ & + \left[\frac{\partial}{\partial S} \left(\frac{\partial U_n}{\partial S} + KU_t \right) \right]^2 + \left(P + \frac{1}{\bar{I}} \right) \left(\frac{\partial U_t}{\partial S} - KU_n \right)^2 \\ & \left. + P \left(\frac{\partial U_n}{\partial S} + KU_t \right)^2 \right\} dS \end{aligned} \quad (2.30)$$

$$\bar{\Pi}_T = \frac{1}{2} \int_0^1 \left\{ \left(\frac{\partial^2 U_n}{\partial T^2} \right)^2 + \left(\frac{\partial^2 U_t}{\partial T^2} \right)^2 \right\} dS \quad (2.31)$$

Note that $\bar{\Pi}_V$ and $\bar{\Pi}_T$ are related to Π_V and Π_T , respectively, by the relations

$$\bar{\Pi}_V = \frac{L}{EI} \Pi_V, \quad \bar{\Pi}_T = \frac{L}{EI} \Pi_T$$

In Eq.(2.30), terms 1 and 2 of the integrand are functions of S alone, and not a function of time. The same is true for terms 3 and 4 since a variation of the integral of these terms can be shown to be zero. The first four terms of Eq.(2.30) therefore result in constant strain energy, which does not contribute to the vibration of the system.

We assume U_n and U_t to be of the form

$$U_n(S, T) = V_n(S) e^{i\omega T}, \quad U_t(S, T) = V_t(S) e^{i\omega T} \quad (2.32)$$

where $V_n(S)$ and $V_t(S)$ are the mode shapes. The mode shapes are discretized as follows:

$$V_n(S) = \sum_i W_{n,i}(S) Y_i = W_n(S) \cdot Y \quad (2.33)$$

$$V_t(S) = \sum_i W_{t,i}(S) Z_i = W_t(S) \cdot Z \quad (2.34)$$

where $W_n(S)$ and $W_t(S)$ are vectors of known shape functions. They are constructed using piecewise polynomials (cubic and linear respectively), standard in finite element discretizations, with discontinuities at nodes. Y and Z are vectors of nodal degrees of freedom (see Eq.(2.38) below) associated with V_n and V_t . Substituting Eqs.(2.32), (2.33) and (2.34) into Eqs.(2.30) and (2.31), we rewrite the non-dimensional kinetic and strain energies as follows:

$$\bar{\Pi}_V = \frac{e^{i2\omega T}}{2} \begin{bmatrix} Y^T & Z^T \end{bmatrix} \mathbb{K}_A \begin{bmatrix} Y \\ Z \end{bmatrix} + Const \quad (2.35)$$

$$\bar{\Pi}_T = \frac{e^{i2\omega T}}{2} (-\omega^2) \begin{bmatrix} Y^T & Z^T \end{bmatrix} \mathbb{M}_A \begin{bmatrix} Y \\ Z \end{bmatrix} \quad (2.36)$$

where

$$Const = \frac{1}{2} \int_0^1 \left\{ K^2 + P^2 \bar{I} + 2K \frac{\partial}{\partial S} \left(\frac{\partial U_n}{\partial S} + K U_t \right) + 2P \left(\frac{\partial U_t}{\partial S} - K U_n \right) \right\} dS \quad (2.37)$$

is the constant strain energy associated with the static equilibrium configuration, discussed before. The mass and stiffness matrices \mathbb{M}_A and \mathbb{K}_A of the elastica arch (support structure) are associated with the generalized coordinate X_A

$$\begin{aligned} X_A &= e^{i\omega T} \begin{bmatrix} Y^T & \vdots & Z^T \end{bmatrix}^T \\ &= \left[u_n^\ell, \theta_A^\ell, \dots, u_n^i, \theta_A^i, \dots, u_n^r, \theta_A^r \vdots u_t^\ell, \dots, u_t^i, \dots, u_t^r \right]^T \end{aligned} \quad (2.38)$$

where u_n and u_t are the translational degrees-of-freedom and θ_A is the rotational degree-of-freedom of each node, and ℓ , r and i denote the left end-node, right end-node and i -th node, respectively, of

the elastica arch. Note that elements of Y and Z need to be consistent with the geometric boundary conditions

$$V_n(S = 1) = 0, \quad V_t(S = 1) = 0, \quad V_n(S = 0) = \tan \theta_0 \cdot V_t(S = 0)$$

The above boundary conditions will be changed when the elastica arch is assembled with the hinged panel array.

2.3.4 Hinged panel array model

The array of hinged panels is shown in Fig.2.7. It was modeled using a standard finite element method. We used two-dimensional two-node frame elements with three degrees of freedom at each node: two translational and one rotational degrees of freedom. A geometric stiffness matrix was added to the standard frame stiffness matrix to model the effect of tension f . A hinge between two panels is treated as a node in the finite element model. The left and right elements of the hinge node have independent rotations but have common translations. The degrees-of-freedom of the hinged panel array are denoted by

$$X_P = \left[\begin{array}{c} x^\ell, y^\ell, \theta_P^\ell, \dots, \underbrace{x^k, y^k, \theta_P^k}_{\text{node } k \text{ on panel array}}, \underbrace{x^{k+1}, y^{k+1}, \theta_P^{k+1}}_{\text{node } (k+1) \text{ on panel array}}, \dots, x^r, y^r, \theta_P^r \end{array} \right]^T \quad (2.39)$$

where x and y are the translational degrees-of-freedom and θ_P is the rotational degree-of-freedom of each node, and ℓ , r and k denote the left end-node, right end-node and k -th node, respectively, of the hinged panel array. For the generalized coordinates X_P , the mass and stiffness matrices are assembled as \mathbb{M}_P and \mathbb{K}_P .

The hinged panel array is then assembled with the elastica arch by connecting their ends together using pin joints. In the modelling, that is to assemble \mathbb{M}_A with \mathbb{M}_P and assemble \mathbb{K}_A with \mathbb{K}_P . After assembly, the end nodes of the two substructures share translations in the plane but maintain independent rotational degrees of freedom.



Figure 2.7 The array of hinged panels

2.3.5 Methods of stiffness variation

Stiffness variation described by Eq.(2.7) is realized in the assembled tension-aligned structure by two methods. These two methods are depicted in Fig.2.8 and are described below:

- (A) The rotations of two adjacent panels at their common hinge, θ_P^k and θ_P^{k+1} , are connected by a rotational spring of time-varying stiffness.
- (B) Node i on the elastica arch and node j on the panel array are connected by a translational spring of time-varying stiffness.

Method (A) can be implemented by placing an electromagnetic brake at the hinge of the adjacent panels. Turning on the brake will prevent relative rotation between the adjacent panels and will be equivalent to constraining the degrees of freedom θ_P^k and θ_P^{k+1} by a rotational spring of very high stiffness. Turning off the brake will release the degrees of freedom and will be equivalent to setting the spring stiffness to zero. Method (B) can be implemented by connecting and disconnecting an elastic bar between a point on the arch and a point on the panel. These two points will be chosen to coincide with nodes of the finite element model for the purpose of simulation.

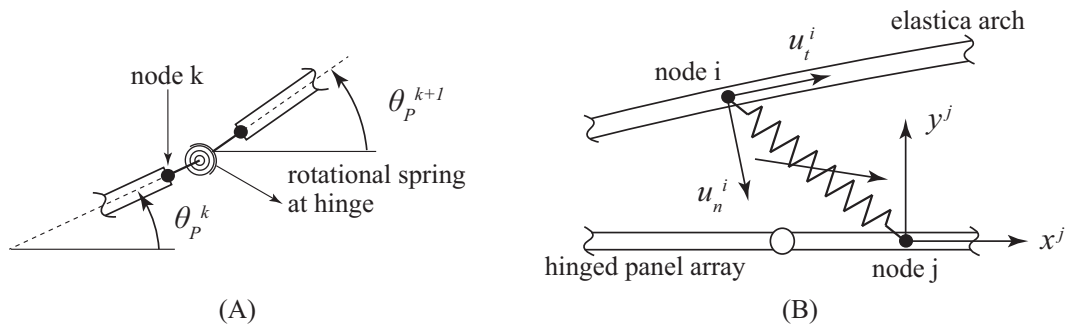


Figure 2.8 Stiffness variation in the tension-aligned structure is realized using two methods: (A) and (B); these are described in section 3.4.

The stiffness of the tension-aligned structure can be varied using multiple springs of the type described in method (A) and/or method (B). Since each of these springs can be in one of two states, the tension-aligned structure will have multiple stiffness states. In the next section, where we present simulation results, the stiffness of the structure will be switched cyclically between the lowest stiffness state and the highest stiffness state via intermediate stiffness states. The lowest and highest stiffness states are defined as the states with the lowest and the highest fundamental frequency.

2.3.6 Numerical simulation

The material and geometric properties of the tension-aligned structure are provided in Table 2.2. The structure is made of aluminum and the damping ratio of all modes is assumed to be $\zeta = 0.001$. The panel array is comprised of eight panels of dimensions $L_p \times b \times h$; these dimensions are shown in Fig.2.9. Each panel is modelled using 10 beam elements. The support structure (elastica arch) is initially a straight rod of radius 0.04 m and length ≈ 8.00 m. It is modelled using 80 elements. The eccentricity of the load applied to the support structure is 0.008 m. The tension in the hinged panel array was assumed to be 1000 N. This is less than 5% of the buckling load of the straight rod with free-free boundary conditions. In this subsection, we simulate the behavior of the structure without control and the structure controlled using two different methods of stiffness variation.

We take an initial condition where the second joint of the hinged panel array (see Fig.2.9) was displaced vertically by 0.01 m (1% of the length of the panel array) and released. The first 25

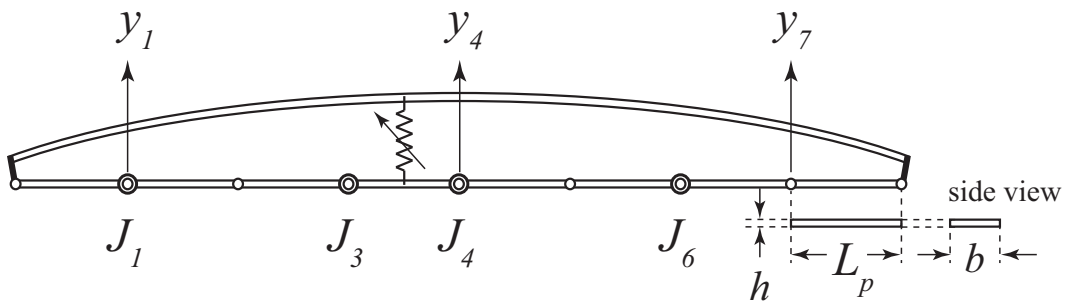


Figure 2.9 The eight-panel tension-aligned structure used in simulations.

Table 2.2 Properties of Simulated Tension-Aligned Structure

Material	Aluminum
Young's modulus E	69×10^9 Pa
Density $\bar{\rho}$	2700 kg/m^3
Damping ratio ζ	0.001
Panel number	8
Panel length L_p	1.000 m
Panel area $b \times h$	$0.500 \text{ m} \times 0.015 \text{ m}$
Radius of support rod r	0.040 m
Length of support rod L	8.000 m approx.
Eccentricity of connection d	0.008 m
Tension f	1000 N

modes of the structure were simulated; these do not include the rigid-body modes. The energy of the tension-aligned structure is shown in Fig.2.10 for three different cases, as described below:

1. Unconstrained structure (no control) undergoing free vibration,
2. Constrained structure (no control) with high-stiffness rotational spring in joints J_1, J_3, J_4 and J_6 - see Fig.2.9. Using method (A) of stiffness variation, the stiffness of the rotational springs is activated when the adjacent panels are aligned. The rotational springs are activated at the earliest possible opportunity in a sequential manner and are kept in their high stiffness state.
3. Controlled structure with switched stiffness using method (A). The high-stiffness rotational springs in joints J_1, J_3, J_4 and J_6 are activated sequentially when their adjacent panels are aligned and their stiffness are then set to zero simultaneously. The process is repeated 92 times in the simulation period of 180 sec.

It is clear from Fig.2.10 that the energies of the unconstrained structure and the constrained structure decay slowly compared to the structure with switched stiffness. After 180 sec, the unconstrained structure and the constrained structure have $\approx 22.5\%$ of their initial energy left; in contrast, the structure with switched stiffness has $\approx 0.4\%$ of its initial energy left. Although vibration en-

energy is dissipated through internal damping in all three cases, the structure with switched stiffness has a higher rate of energy dissipation since it effectively funnels energy from the low-frequency modes to the high-frequency modes.

For the structure with switched stiffness, the joints are released simultaneously, not sequentially, to reduce the time required for each cycle of constraint application and removal. In simulations, where high-stiffness springs are used to constrain the joints, simultaneous release of the joints causes residual energy stored in the springs to vanish. This discontinuous change in the energy is not the main mechanism of energy dissipation. An evaluation of this energy over all cycles indicates that it does not exceed 0.1% of the total energy at its initial level. This means the bulk of the energy is dissipated due to energy transfer from low-frequency modes to high-frequency modes. In practical implementation (Issa et al., 2008), where electromagnetic brakes may be used to constrain the joints, release of the brakes will not result in direct loss of energy (since brakes do not store energy) but facilitate energy transfer to the high-frequency modes where they will be dissipated quickly.

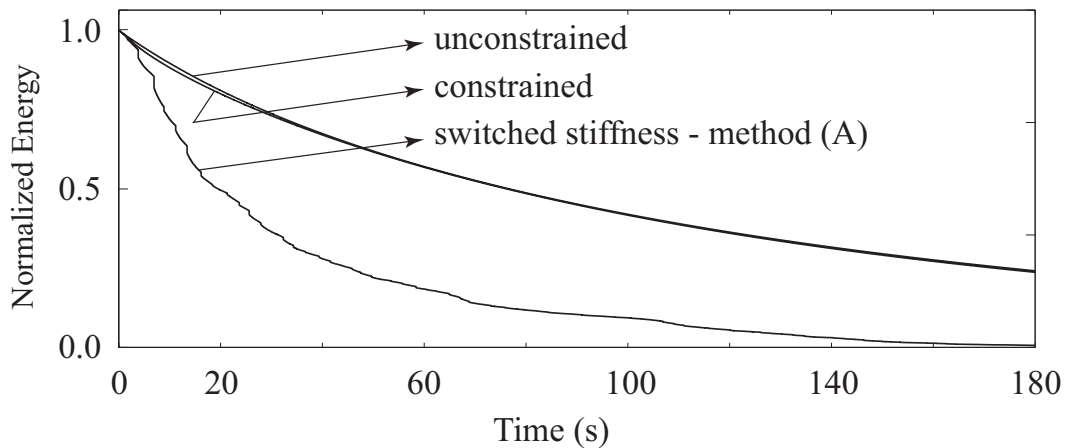


Figure 2.10 Plot of energy for the three cases discussed in Section 4.2.

The rates of energy decay of the unconstrained structure and the constrained structure are almost identical. Since the structure has many degrees-of-freedom and activating the springs in four joints only makes it marginally stiffer than the unconstrained structure. This can be verified from Table 2.3, which shows the first six natural frequencies of the unconstrained and constrained

structures.

Table 2.3 First six natural frequencies of the unconstrained and the constrained tension-aligned structure in rad/s.

Unconstrained	ω_1	ω_2	ω_3	ω_4	ω_5	ω_6
	3.820	6.999	9.129	13.144	15.859	20.213
Constrained	$\bar{\omega}_1$	$\bar{\omega}_2$	$\bar{\omega}_3$	$\bar{\omega}_4$	$\bar{\omega}_5$	$\bar{\omega}_6$
	3.996	7.502	11.096	28.042	37.875	71.666

The structure with switched stiffness, where stiffness is varied using method (A), has a faster rate of energy decay than the uncontrolled (unconstrained and constrained) structures.

In order to further improve the efficiency of the control using switched stiffness, we need to investigate different methods of stiffness variation. Applying methods (A) and (B), again using 25 modes, the behavior of the structure was simulated for the same initial condition that was used in the previous case. The energy of the tension-aligned structure is shown in Fig.2.11 for the following three cases:

1. Unconstrained structure undergoing free vibration
2. Structure with switched stiffness using method (A). The high-stiffness rotational springs in joints J_1 , J_3 , J_4 and J_6 are activated sequentially when their adjacent panels are aligned and their stiffness are then set to zero simultaneously. The process is repeated 92 times within the simulation period of 180 sec.
3. Structure with switched stiffness using methods (A) and (B). The high-stiffness rotational springs in joints J_1 , J_3 , and J_4 are activated sequentially when their adjacent panels are aligned. This is followed by connecting an elastic bar (high-stiffness translational spring) between a point on the elastica arch and a point on the panel array (see Fig.2.9) in a manner such that no energy is added to the structure. The stiffness of all four springs are then set to zero simultaneously. The process is repeated 105 times within the simulation period of 5180 sec.

It is clear from Fig.2.11 that the energy of the uncontrolled structure decays slowly compared to the structure with switched stiffness. After 180 sec, the uncontrolled structure has $\approx 22.5\%$ of its initial energy left; in contrast, the structure with switched stiffness using method (A) has $\approx 0.4\%$ of its initial energy left. For vibration suppression to $\approx 0.4\%$ energy level, methods (A) and (B) combined requires 76 sec as compared to 180 sec required by method (A). Accordingly, for the case of methods (A) and (B) combined, the transverse displacements of three points on the hinged panel array Fig.2.12, which clearly shows the suppression of vibration.

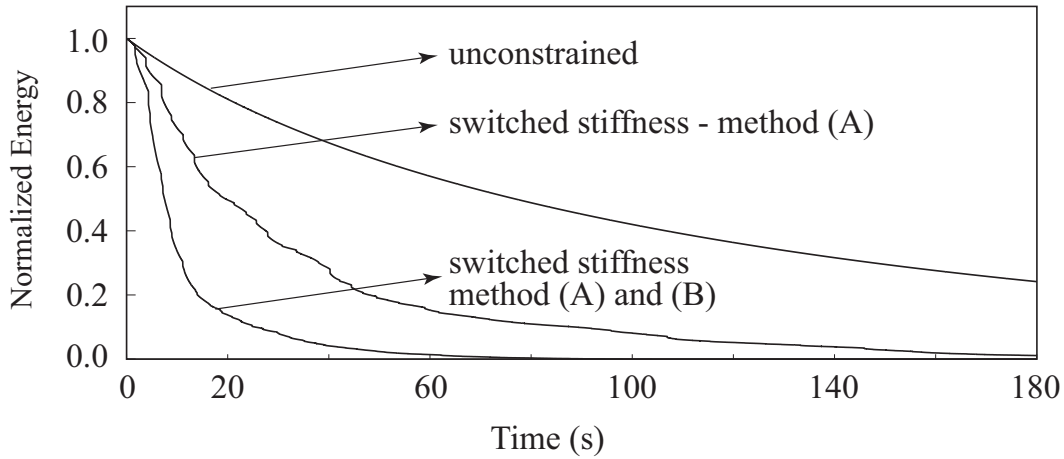


Figure 2.11 Plot of energy for the three cases simulated.

The efficiency of vibration suppression using stiffness variation can be much improved by combining methods (A) and (B). This improvement in effectiveness can be understood by examining the modal disparity matrices for the two cases and comparing their modal disparity indices. The modal disparity indices for these two cases were computed as

$$\lambda_A = 22.15, \quad \lambda_{AB} = 40.48 \quad (2.40)$$

Since λ_{AB} is greater than λ_A , stiffness variation combining methods (A) and (B) is more effective than method (A) in transferring energy from the low-frequency modes to the high-frequency modes. Modal disparity proves to be an effective measure to evaluate the magnitude of stiffness variation for the purpose of vibration suppression.

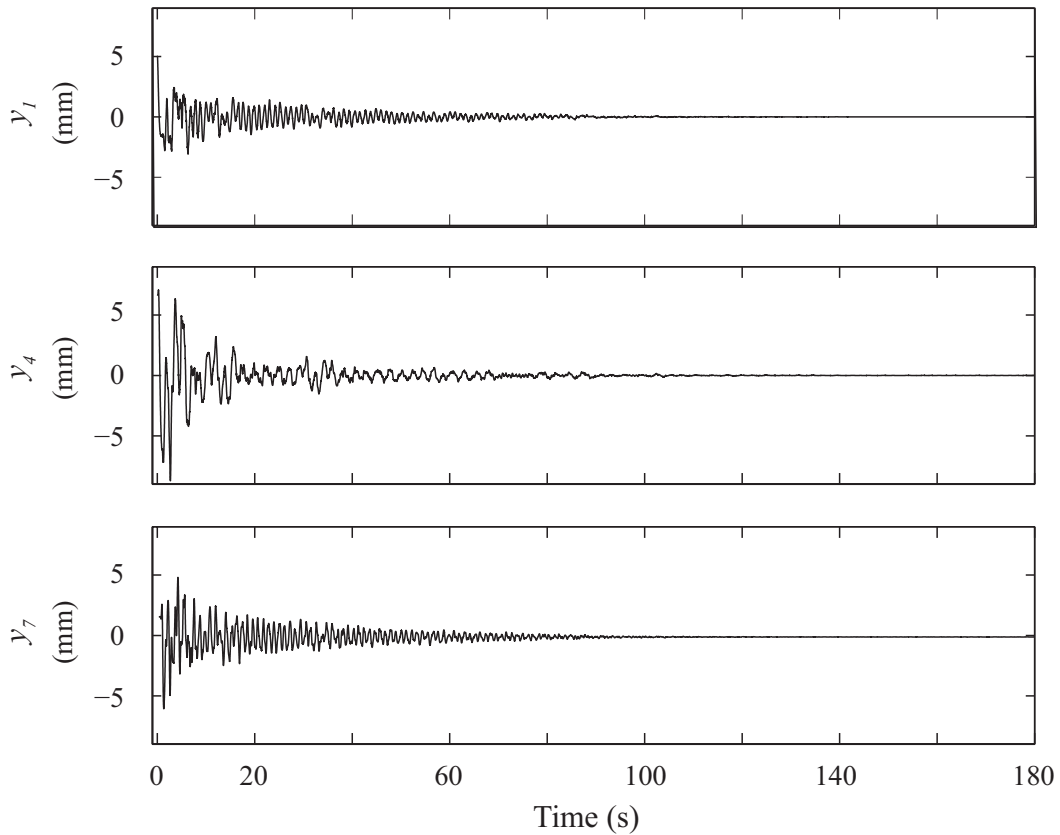


Figure 2.12 Plots of the transverse displacements of three points on the hinged panel array (see Fig.2.9), in the case of methods (A) and (B) combined.

2.4 Model of a three-dimensional tension-aligned structure

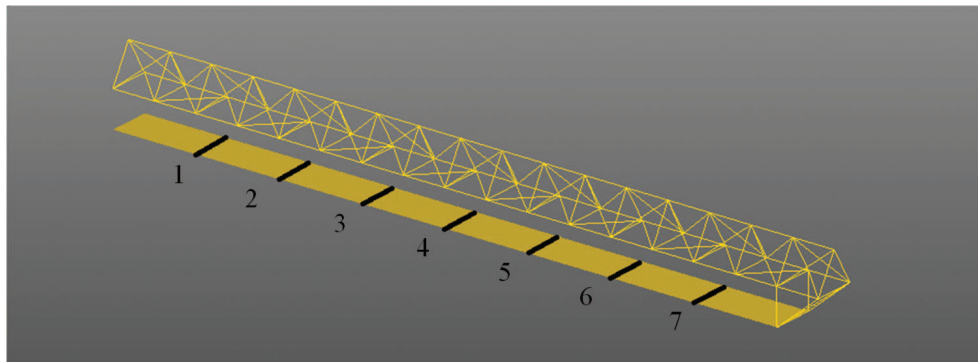


Figure 2.13 Overview of the tension-aligned three-dimensional structure. 8 panels are connected using 7 hinges and supported by a truss structure.

A three-dimensional model was built to verify the effectiveness of the stiffness variation method in a more realistic structure. This model takes the design data of the truss structure from

the ISAT project and we set all material as aluminum. 17 truss cells were built. Each cell has the dimension of 0.5 m and the truss structure has the total length of 8.5 m. The truss functions as a support structure and provides tension for the hinged panel array where the antenna is mounted. There are 8 panels hinged to form an array and each panel has the dimension of 1.00 m \times 0.50 m \times 0.01 m. The overview of structure is shown in Fig.2.13. The combined structure is clamped at one end and free at another. The tension level is set to be 200 N. The geometry of the structure is depicted in Fig.2.14.

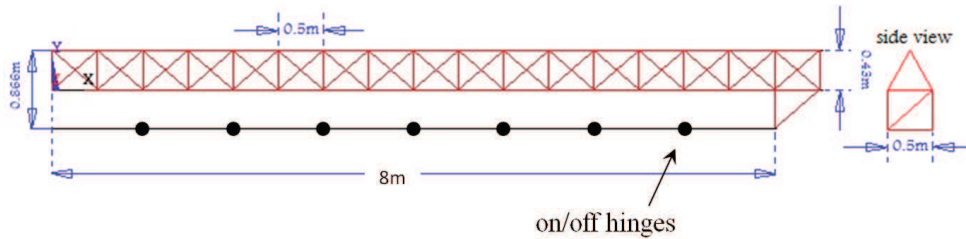


Figure 2.14 Geometry of the three-dimensional structure.

ANSYS was used for the finite element modelling. The truss structure was modelled using link elements that have two nodes and three degrees of freedom at each node. The plates were modelled using shell elements that have four nodes and six degrees of freedom at each node. The total number of DOF is 648, and 25 modes were used in the dynamic simulation.

Only method (A) was used in this model for the application of stiffness variation. The control logic was similar to the two-dimensional model. Results of vibration suppression were very consistent, as shown in Fig.2.15. When four hinges were used, the energy plot resembles the results of the two-dimensional model. As the number of controlled hinges increased, vibration suppression became more efficient. This is because the magnitude of the modal disparity increases as the number of controlled hinges increases. In all cases of controlled hinges used, stiffness variations as a control method has shown its efficacy in vibration suppression in the three-dimensional tension-aligned structure model.

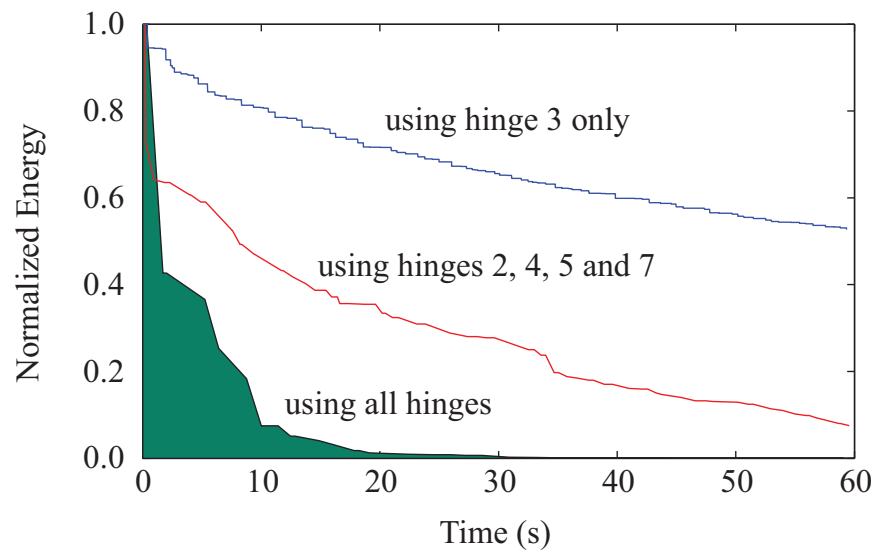


Figure 2.15 Plot of energy for cases of controlling different number of joints.

CHAPTER 3

VIBRATION SUPPRESSION USING A SLIDING MECHANISM

3.1 Sliding mechanism description

Sliding mechanism in the form of constraints in flexible structures has been investigated by many researchers, especially in areas such as contact mechanics (Popov, 2010; Fischer-Cripps, 2007) and flexible multibody dynamics (Bauchau, 2010; Wittbrodt, 2006). A good example that has been studied frequently is the quick return mechanism (Barhorst, 2004) where an inverted slider crank is connected with a flexible follower. Usually Hamilton's principle is used together with Lagrange multipliers to formulate the equations of motion of the system. Constraint forces can be found by solving for the Lagrange multipliers. Finite element methods are very powerful tools for numerical simulations of these systems, where Arbitrary Lagrange-Euler (ALE) descriptions are usually needed to allow finite element nodes to move in the material coordinate system (Hong & Ren, 2011).

The dynamics of constrained systems, such as the sliding constraint discussed above, are usually described by Differential Algebraic Equations (DAE) in order to obtain the constraint forces and to solve for the system states. The idea of controlling the motion of a sliding constraint in a flexible structure for the purpose of vibration suppression is new and has not been explored in the literature. This study considers a simple structure of a nonlinear beam with pinned-pinned boundary conditions and a sliding constraint which is frictionless. Assuming that the constraint force could be measured, a straightforward control strategy is developed to do negative work on the system and suppress the vibration energy of the beam. A mathematical model of a nonlinear beam will be presented in the following section. A simple feedback control scheme for the purpose of vibration suppression will be presented as well. Then a modified control design that reduces the bandwidth requirement of the actuator will also be introduced.

3.2 Equations of motion for a nonlinear beam with a fixed slider

Similar to Section 2.3, we derive the planar vibration model of the nonlinear beam following the work by Perkins (1990) on the elastica arch. Consider a slender beam shown in Fig.3.1, held in equilibrium under horizontal end load f , where f can be either tensile or compressive yet less than the buckling load. The beam is initially straight and keeps being straight with f applied. It is measured to have length L under f . Both ends of the beam are subsequently pinned to the ground; this creates pre-stress in the beam. A frictionless slider is assumed to constrain the motion of the beam; its location is fixed in space that initially coincides with the midpoint of the beam. The slider restricts the position of the material point on the beam in contact with it, but does not restrict the slope of the beam. Since the slider is fixed and does not move with the beam, material can flow through it. A point Q on the beam instantaneously in contact with the constraint can be described using material coordinate $s = s_q$, where coordinate s is measured in the initial equilibrium configuration using Lagrangian description (material coordinate). Due to a disturbance, the beam starts to deform. A given point on the beam has displacement of $\vec{u}(s,t)$, where t denotes time. $\vec{u}(s,t)$ can be decomposed into an axial component $\vec{u}_t(s,t)$ which is always in the X-direction and a transverse component $\vec{u}_n(s,t)$, which is always in the Y-direction. Note that two sets of coordinates are used here, namely the material coordinate system s and the X - Y frame.

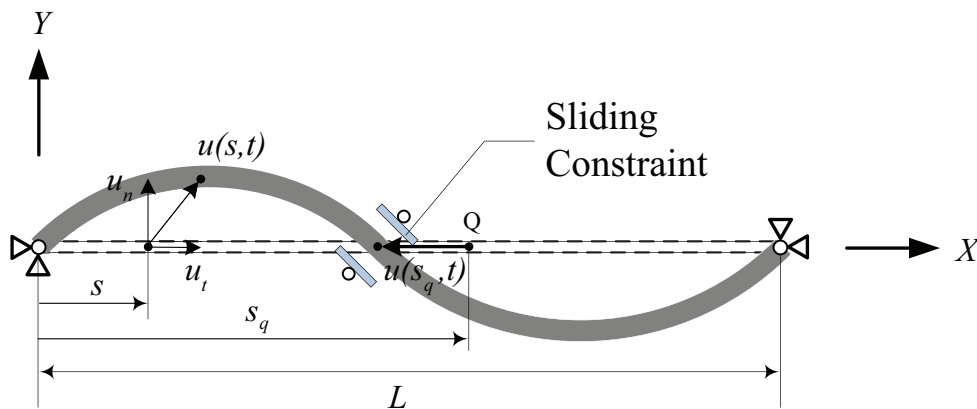


Figure 3.1 A pinned-pinned beam with a sliding constraint.

The sliding constraints can be described as

$$C_x = u_t(s = s_q, t) + s_q(t) - L/2 = 0 \quad (3.1)$$

$$C_y = u_n(s = s_q, t) = 0 \quad (3.2)$$

where Eq (3.1) states that the material point Q in contact with the slider is initially measured as s_q in the initial equilibrium configuration, and that point Q has an axial displacement of u_t in order to keep in contact with the slider; Eq.(3.2) states that any material point in contact with the constraint should never have transverse motion.

We use Kirchhoff's assumptions for beam deformation (Dill, 1992). (i) The beam is linearly elastic. (ii) Strains are small (although accumulated rotations may be large), and the cross-sectional dimensions of the beam are small compared to its length. (iii) Cross-sections remain planar, undistorted and normal to the axis of the beam. (iv) The transverse stress and rotary inertia are negligible. In light of these assumptions, with the consideration that the beam remains straight in its equilibrium configuration, the nonlinear axial strain can be written as Perkins & Mote (1987)

$$e = -f/EA + \frac{\partial u_t}{\partial s} + \frac{1}{2} \left[\left(\frac{\partial u_t}{\partial s} \right)^2 + \left(\frac{\partial u_n}{\partial s} \right)^2 \right] \quad (3.3)$$

The curvature k can be expressed as in Love (1944)

$$k = \frac{\partial^2 u_n}{\partial s^2} \quad (3.4)$$

where A , E , and I denote the cross-sectional area, Young's modulus, and area moment of inertia of the beam respectively. The virtual work done by internal elastic forces due to any virtual deformation can be written as

$$\int_{\Omega} \sigma \delta[\varepsilon] d\Omega = \int_0^L EAe\delta[e] ds + \int_0^L EI k \delta[k] ds \quad (3.5)$$

where σ and ε represent general stress and strain respectively. Ω is the domain of interest, which includes all material points on the beam.

We use the principle of virtual displacement and D'Alembert's principle, together with Lagrange multipliers to describe the dynamics of the beam in the following form:

$$\int_{\Omega} \sigma \delta[\varepsilon] + (-\mathbf{P} + \rho \ddot{\mathbf{u}}) \cdot \delta[\mathbf{u}] d\Omega = \delta[\boldsymbol{\lambda} \cdot \mathbf{C}] \quad (3.6)$$

where vector \mathbf{P} is the external force, \mathbf{u} is the displacement field, $(\dot{\quad})$ is the derivative with respect to time t , $\boldsymbol{\lambda}$ is a vector of Lagrange multipliers, and \mathbf{C} is the vector of constraint expressions. The term on the right hand side of Eq.(3.6) can be expanded as

$$\boldsymbol{\lambda} \cdot \mathbf{C} = \lambda_x C_x + \lambda_y C_y \quad (3.7)$$

where the expressions for C_x and C_y are given in Eqs.(3.1) and (3.2). Since Lagrange multipliers have the physical interpretations of constraint forces, λ_x and λ_y represent the constraint forces in axial and transverse directions, or X- and Y-directions respectively.

Equation (3.6) states that the beam is in dynamic equilibrium if the external virtual work done by the applied forces, including the constraint forces, is equal to the internal virtual work done by the forces due to any virtual deformation that satisfies the kinematic boundary conditions. Here, the internal virtual work is extended with an inertial term using D'Alembert's principle. The kinematic boundary conditions for constraints are included on the right hand side of the equation. These constraint conditions described by Eqs.(3.1) and (3.2) could be recovered if collecting the variations of Lagrange multipliers.

In our problem, \mathbf{P} will only be used in setting up the static problem to create the initial condition. As far as the dynamic problem is in concern, we simply set external forces to be zero

$$\mathbf{P} = 0 \quad (3.8)$$

Substituting Eqs.(3.3) and (3.4) into Eq.(3.5), then substituting the resulting equation together with Eqs.(3.1), (3.2), (3.7) and (3.8) into Eq.(3.6), and using the following non-dimensional quantities:

$$\begin{aligned} S &\triangleq \frac{s}{L}, & S_Q &\triangleq \frac{sq}{L}, & U_t &\triangleq \frac{u_t}{L}, & U_n &\triangleq \frac{u_n}{L}, & K &\triangleq kL \\ F &\triangleq \frac{fL^2}{EI}, & \bar{I} &\triangleq \frac{I}{AL^2}, & T &\triangleq \frac{t}{(\rho L^4/EI)^{1/2}}, & \Lambda &\triangleq \frac{\lambda L^2}{EI} \end{aligned} \quad (3.9)$$

we get the energy form of the equations of motion

$$\begin{aligned}
& \int_0^1 \ddot{U}_n \delta[U_n] dS + \int_0^1 \ddot{U}_t \delta[U_t] dS + \int_0^1 \frac{\partial^2 U_n}{\partial S^2} \delta \left[\frac{\partial^2 U_n}{\partial S^2} \right] dS \\
& + \int_0^1 \left(-F + \frac{1}{\bar{I}} \frac{\partial U_t}{\partial S} + \frac{1}{2\bar{I}} \left(\frac{\partial U_t}{\partial S} \right)^2 + \frac{1}{2\bar{I}} \left(\frac{\partial U_n}{\partial S} \right)^2 \right) \frac{\partial U_n}{\partial S} \delta \left[\frac{\partial U_n}{\partial S} \right] dS \\
& + \int_0^1 \left(-F + \frac{1}{\bar{I}} \frac{\partial U_t}{\partial S} + \frac{1}{2\bar{I}} \left(\frac{\partial U_t}{\partial S} \right)^2 + \frac{1}{2\bar{I}} \left(\frac{\partial U_n}{\partial S} \right)^2 \right) \left(1 + \frac{\partial U_t}{\partial S} \right) \delta \left[\frac{\partial U_t}{\partial S} \right] dS \\
& = \left\{ \Lambda_y \frac{\partial U_n(S=S_Q)}{\partial S} + \Lambda_x \left(\frac{\partial U_t(S=S_Q)}{\partial S} + 1 \right) \right\} \delta[S_Q] \\
& + U_n(S=S_Q) \delta[\Lambda_y] + \{ U_t(S=S_Q) + S_Q - 1/2 \} \delta[\Lambda_x] \\
& + \Lambda_y \delta [U_n(S=S_Q)] + \Lambda_x \delta [U_t(S=S_Q)]
\end{aligned} \tag{3.10}$$

Integrating Eq.(3.10) by parts and collecting like terms of independent variations yield the differential form of equations of motion and boundary conditions. The PDEs are written as the following:
from collecting terms involving $\delta[U_n]$

$$\begin{aligned}
& -\frac{\partial^4 U_n}{\partial S^4} - F \frac{\partial^2 U_n}{\partial S^2} + \frac{3}{2\bar{I}} \left(\frac{\partial U_n}{\partial S} \right)^2 \frac{\partial^2 U_n}{\partial S^2} + \frac{1}{2\bar{I}} \frac{\partial^2 U_n}{\partial S^2} \left(\frac{\partial U_t}{\partial S} \right)^2 + \frac{1}{\bar{I}} \frac{\partial U_n}{\partial S} \frac{\partial U_t}{\partial S} \frac{\partial^2 U_t}{\partial S^2} \\
& + \frac{1}{\bar{I}} \frac{\partial^2 U_n}{\partial S^2} \frac{\partial U_t}{\partial S} + \frac{1}{\bar{I}} \frac{\partial U_n}{\partial S} \frac{\partial^2 U_t}{\partial S^2} + \Lambda_y \mathcal{D}(S_Q - S) = \frac{\partial^2 U_n}{\partial T^2}
\end{aligned} \tag{3.11}$$

from collecting terms involving $\delta[U_t]$

$$\begin{aligned}
& \left(-F + \frac{1}{\bar{I}} \right) \frac{\partial^2 U_t}{\partial S^2} + \frac{3}{2\bar{I}} \left(\frac{\partial U_t}{\partial S} \right)^2 \frac{\partial^2 U_t}{\partial S^2} + \frac{1}{\bar{I}} \frac{\partial U_n}{\partial S} \frac{\partial U_t}{\partial S} \frac{\partial^2 U_n}{\partial S^2} + \frac{1}{2\bar{I}} \left(\frac{\partial U_n}{\partial S} \right)^2 \frac{\partial^2 U_t}{\partial S^2} \\
& + \frac{3}{\bar{I}} \frac{\partial U_t}{\partial S} \frac{\partial^2 U_t}{\partial S^2} + \frac{1}{\bar{I}} \frac{\partial U_n}{\partial S} \frac{\partial^2 U_n}{\partial S^2} + \Lambda_x \mathcal{D}(S_Q - S) = \frac{\partial^2 U_t}{\partial T^2}
\end{aligned} \tag{3.12}$$

from collecting terms involving $\delta[S_Q]$

$$\Lambda_y \frac{\partial U_n(S=S_Q, T)}{\partial S} + \Lambda_x \frac{\partial U_t(S=S_Q, T)}{\partial S} + \Lambda_x = 0 \tag{3.13}$$

together with the recovered constraint equations in non-dimensional form from collecting terms involving $\delta\Lambda_x$ and $\delta\Lambda_y$

$$U_n(S = S_Q, T) = 0 \quad (3.14)$$

$$U_t(S = S_Q, T) + S_Q - 1/2 = 0 \quad (3.15)$$

where in Eqs.(3.11) and (3.12) $\mathcal{D}(\cdot)$ is the Dirac delta function.

Eqs.(3.11) - (3.15) are a full set of equations of motion describing the dynamics of a nonlinear beam with a fixed slider. If damping is to be added to the system, Eq.(3.6) needs to be rewritten to include the viscous damping terms, such as

$$\int_{\Omega} \sigma \delta[\varepsilon] + \eta \dot{\sigma} \delta[\varepsilon] + (-\mathbf{P} + \rho \ddot{\mathbf{u}}) \cdot \delta[\mathbf{u}] d\Omega = \delta[\lambda \cdot \mathbf{C}] \quad (3.16)$$

where the added term $\eta \dot{\sigma} \delta[\varepsilon]$ expresses that the internal damping forces contributing to the virtual work due to any virtual deformation of the structure. It also states that the damping force is proportional to the damping coefficient η and the stress rate $\dot{\sigma}$.

Starting from Eq.(3.16), and repeating the process of nondimensionalization and variation described above, one can get another set of equations of motion with damping present. The process is repetitive and is omitted here.

3.3 Numeric simulation of the sliding mechanism of a nonlinear beam

3.3.1 Finite element discretization using adaptive mesh

The finite element model of our system is established in the framework of the Arbitrary Lagrange-Euler (ALE), following the work of Hong & Ren (2011). To discretize Eq.(3.10) using a finite element method, we choose to put a sliding node on the beam in the same position coinciding with the constraint that takes into account the sliding nature of the constraint. The sliding node does not move in absolute space as long as the constraint is fixed. This special sliding node, therefore, is described using Eulerian description. As for other nodes, where the Lagrangian description is used,

nodes are attached to certain material points chosen at the beginning, and material coordinates of those nodes will remain the same as time progresses (Spencer, 1980).

Because of the existence of the special sliding node, two neighboring elements that share this node become variable-length elements, while other elements are still regular. In this sense, the meshing scheme of the structure is adaptive as the structure deforms and changes its contact point. It is necessary to derive expressions for velocity and acceleration of any material point in a variable-length element, which, compared to regular elements, are more complicated.

Consider a standard 2-node, 6-DOF planar frame element described by material coordinates of the two nodes (S_1^e, S_2^e) and 6 nodal displacements $(U_{n1}^e, U_{n1}^{\prime e}, U_{t1}^e, U_{n2}^e, U_{n2}^{\prime e}, U_{t2}^e)$, where the superscript e indicates element-wise or local numbering is used. In the framework of ALE description, both (S_1^e, S_2^e) and $(U_{n1}^e, U_{n1}^{\prime e}, U_{t1}^e, U_{n2}^e, U_{n2}^{\prime e}, U_{t2}^e)$ can vary with time. Using Hermite polynomials for shape functions of displacement in the normal or transverse direction $U_n^e(S, T)$, we get

$$U_n^e(S, T) = \mathbf{N}_e^T (S, S_1^e(T), S_2^e(T)) \mathbf{q}_n^e(T) \quad (3.17)$$

where

$$\mathbf{N}_e = \begin{pmatrix} 2\xi^3 - 3\xi^2 + 1 \\ \xi^3 - 2\xi^2 + \xi \\ -2\xi^3 + \xi^2 \\ \xi^3 - \xi^2 \end{pmatrix}, \quad \mathbf{q}_n^e = \begin{pmatrix} U_{n1}^e \\ U_{n1}^{\prime e} \\ U_{n2}^e \\ U_{n2}^{\prime e} \end{pmatrix} \triangleq \begin{pmatrix} a_1^e \\ b_1^e \\ a_2^e \\ b_2^e \end{pmatrix} \quad (3.18)$$

and $\xi = (S - S_1^e)/(S_2^e - S_1^e)$. The shape functions \mathbf{N}_e are functions of both material coordinate S and node locations (S_1^e, S_2^e) , which means \mathbf{N}_e are functions of S and T . The nodal displacements \mathbf{q}_n^e are functions of time T only.

Similarly, choosing Lagrange polynomials, the tangential or axial displacement $U_t^e(S, T)$ can be written as

$$U_t^e(S, T) = \mathbf{R}_e^T (S, S_1^e(T), S_2^e(T)) \mathbf{q}_t^e(T) \quad (3.19)$$

where

$$\mathbf{R}_e = \begin{pmatrix} (S_2^e - S)/(S_2^e - S_1^e) \\ S - S_1^e/(S_2^e - S_1^e) \end{pmatrix}, \quad \mathbf{q}_t^e = \begin{pmatrix} U_{t1}^e \\ U_{t2}^e \end{pmatrix} \triangleq \begin{pmatrix} c_1^e \\ c_2^e \end{pmatrix} \quad (3.20)$$

The shape functions \mathbf{R}_e^T are functions of S and T . The nodal displacements \mathbf{q}_t^e are functions of time T .

Differentiating Eqs.(3.17) and (3.19) twice with respect to time, the accelerations can be derived as

$$\begin{aligned} \ddot{U}_n^e = & \mathbf{N}_e^T \ddot{\mathbf{q}}_n^e + \frac{\partial \mathbf{N}_e^T}{\partial S_1^e} \mathbf{q}_n^e \ddot{S}_1^e + \frac{\partial \mathbf{N}_e^T}{\partial S_2^e} \mathbf{q}_n^e \ddot{S}_2^e + 2 \frac{\partial \mathbf{N}_e^T}{\partial S_1^e} \dot{\mathbf{q}}_n^e \dot{S}_1^e + 2 \frac{\partial \mathbf{N}_e^T}{\partial S_2^e} \dot{\mathbf{q}}_n^e \dot{S}_2^e \\ & + \frac{\partial^2 \mathbf{N}_e^T}{\partial S_1^{e2}} \mathbf{q}_n^e \dot{S}_1^{e2} + 2 \frac{\partial^2 \mathbf{N}_e^T}{\partial S_1^e \partial S_2^e} \mathbf{q}_n^e \dot{S}_1^e \dot{S}_2^e + \frac{\partial^2 \mathbf{N}_e^T}{\partial S_2^{e2}} \mathbf{q}_n^e \dot{S}_2^{e2} \end{aligned} \quad (3.21)$$

$$\begin{aligned} \ddot{U}_t^e = & \mathbf{R}_e^T \ddot{\mathbf{q}}_t^e + \frac{\partial \mathbf{R}_e^T}{\partial S_1^e} \mathbf{q}_t^e \ddot{S}_1^e + \frac{\partial \mathbf{R}_e^T}{\partial S_2^e} \mathbf{q}_t^e \ddot{S}_2^e + 2 \frac{\partial \mathbf{R}_e^T}{\partial S_1^e} \dot{\mathbf{q}}_t^e \dot{S}_1^e + 2 \frac{\partial \mathbf{R}_e^T}{\partial S_2^e} \dot{\mathbf{q}}_t^e \dot{S}_2^e \\ & + \frac{\partial^2 \mathbf{R}_e^T}{\partial S_1^{e2}} \mathbf{q}_t^e \dot{S}_1^{e2} + 2 \frac{\partial^2 \mathbf{R}_e^T}{\partial S_1^e \partial S_2^e} \mathbf{q}_t^e \dot{S}_1^e \dot{S}_2^e + \frac{\partial^2 \mathbf{R}_e^T}{\partial S_2^{e2}} \mathbf{q}_t^e \dot{S}_2^{e2} \end{aligned} \quad (3.22)$$

Substituting Eqs.(3.17)-(3.22) into Eq.(3.10) gives us the finite element version of the dynamic system. If the beam is meshed with $2m$ elements, there are m elements to the left and m elements to the right of the constraint. Thus node $m + 1$ counted from the left end is the sliding node on the beam and is fixed in space. This special node has the material coordinate S_Q that varies with time, while other nodes have fixed material coordinates. Now we can use generalized variables \mathbf{q} , a vector with $6m + 4$ entries written as

$$\mathbf{q} = (a_1, a_2, \dots, a_{2m+1}, b_1, b_2, \dots, b_{2m+1}, c_1, c_2, \dots, c_{2m+1}, S_Q, \Lambda_x, \Lambda_y)^T \quad (3.23)$$

$$\begin{aligned}
& \int_0^1 \ddot{U}_n \frac{U_n}{\mathbf{q}} \delta[\mathbf{q}] dS + \int_0^1 \ddot{U}_t \frac{U_t}{\mathbf{q}} \delta[\mathbf{q}] dS + \int_0^1 \frac{\partial^2 U_n}{\partial S^2} \frac{\partial \left(\frac{\partial^2 U_n}{\partial S^2} \right)}{\partial \mathbf{q}} \delta[\mathbf{q}] dS \\
& + \int_0^1 \left(-F + \frac{1}{\bar{I}} \frac{\partial U_t}{\partial S} + \frac{1}{2\bar{I}} \left(\frac{\partial U_t}{\partial S} \right)^2 + \frac{1}{2\bar{I}} \left(\frac{\partial U_n}{\partial S} \right)^2 \right) \frac{\partial U_n}{\partial S} \frac{\partial \left(\frac{\partial U_n}{\partial S} \right)}{\partial \mathbf{q}} \delta[\mathbf{q}] dS \\
& + \int_0^1 \left(-F + \frac{1}{\bar{I}} \frac{\partial U_t}{\partial S} + \frac{1}{2\bar{I}} \left(\frac{\partial U_t}{\partial S} \right)^2 + \frac{1}{2\bar{I}} \left(\frac{\partial U_n}{\partial S} \right)^2 \right) \left(1 + \frac{\partial U_t}{\partial S} \right) \frac{\partial \left(\frac{\partial U_t}{\partial S} \right)}{\partial \mathbf{q}} \delta[\mathbf{q}] dS \quad (3.24) \\
& = \left\{ \Lambda_y \frac{\partial U_n(S=S_Q)}{\partial S} + \Lambda_x \left(\frac{\partial U_t(S=S_Q)}{\partial S} + 1 \right) \right\} \delta[S_Q] \\
& + U_n(S=S_Q) \delta[\Lambda_y] + \{ U_t(S=S_Q) + S_Q - 1/2 \} \delta[\Lambda_x] \\
& + \Lambda_y \delta [U_n(S=S_Q)] + \Lambda_x \delta [U_t(S=S_Q)]
\end{aligned}$$

First, variation of the terms in Eq.(3.10) is carried out by taking derivatives with respect to \mathbf{q} . Then the finite element version of the dynamic system is given as Eq.(3.24). With the help of Lagrange multipliers, we can treat all variables in \mathbf{q} independent with each other, then by collecting coefficients of arbitrary $\delta[\mathbf{q}]$, Eq.(3.24) gives rise to $(6m+6)$ nonlinear equations. Among them, by collecting coefficients of $\delta[\Lambda_x]$ and $\delta[\Lambda_y]$, two constraint equations are recovered as

$$\begin{aligned}
C_x &= c_{m+1} + S_{m+1} - 1/2 = 0 \\
C_y &= a_{m+1} = 0
\end{aligned} \quad (3.25)$$

Geometric boundary conditions, pinned-pinned two ends, give

$$U_n(S=0) = U_t(S=0) = U_n(S=1) = U_t(S=1) = 0$$

or

$$a_1 = c_1 = a_{2m+1} = c_{2m+1} = 0 \quad (3.26)$$

They cancel four equations out from $(6m+6)$. In total, $(6m+2)$ equations are obtained regarding \mathbf{q} . They can be written as

$$\mathbf{M}(\mathbf{q}, T) \ddot{\mathbf{q}} = \mathbf{F}(\mathbf{q}, \dot{\mathbf{q}}, T) \quad (3.27)$$

where \mathbf{M} is the generalized mass matrix and \mathbf{F} is the generalized force vector. If damping is present, one can follow the whole process starting from Eq.(3.16), then obtain a discretized dynamic system with the form very similar to Eq.(3.27). The process is not repeated here. It is worth mentioning that since the two constraint equations expressed are included, Eq.(3.27) is essentially a Differential Algebraic Equation (DAE) system, featured by the generalized mass \mathbf{M} being singular. This requires special numeric solvers to be described later. Up to this point, it has been shown that the system is successfully discretized using variable-length finite elements (adaptive meshing).

Table 3.1 Properties and geometry of the simulated beam with a sliding constraint.

Material	Aluminum
Young's modulus E	69×10^9 Pa
Density $\bar{\rho}$	2700 kg/m^3
Damping coefficient η	10^{-5} sec
Beam length L	3.66 m
Beam cross section area	$38.1 \text{ mm} \times 1.57 \text{ mm}$
Pre-load f	0 N

A numeric simulation of free vibration is given to demonstrate the effectiveness of our mathematical model. Geometry and material properties used in the simulation are listed in Table 3.1. In the numeric model, the beam was meshed using 20 frame elements. A sliding joint, node number 11 counted from the left end, was placed on the beam at the same position where the sliding constraint was located, with the material coordinate S_Q as a variable to be solved. There were 10 elements to the left and 10 elements to the right of the sliding node. Elements number 10 and 11 were variable-length elements, while other elements were regular elements which had nodes with fixed coordinates allocated at the beginning. Initial conditions were created by applying a 5 N transverse force positive in Y-direction on the beam at $S = 0.75$ or $s = 2.743$ m. Eq (3.27) were formulated and numerically integrated by time to solve for $\mathbf{q}(T)$, $\dot{\mathbf{q}}(T)$ as time progressed. This process was done using MATLAB solver `ode15s`. `ode15s` is a variable order solver based on the numerical differentiation formulas (NDFs). Optionally, it uses the backward differentiation formulas

(BDFs, also known as Gear's method) that are usually less efficient. ode15s was chosen as the numeric solver because it is suitable for solving a differential algebraic problem, i.e., mass matrix being singular. For more details, refer to Shampine & Reichelt (1997) and Shampine et al. (1999). The results of the free vibration simulation are shown in Fig.3.2 with dimensions.

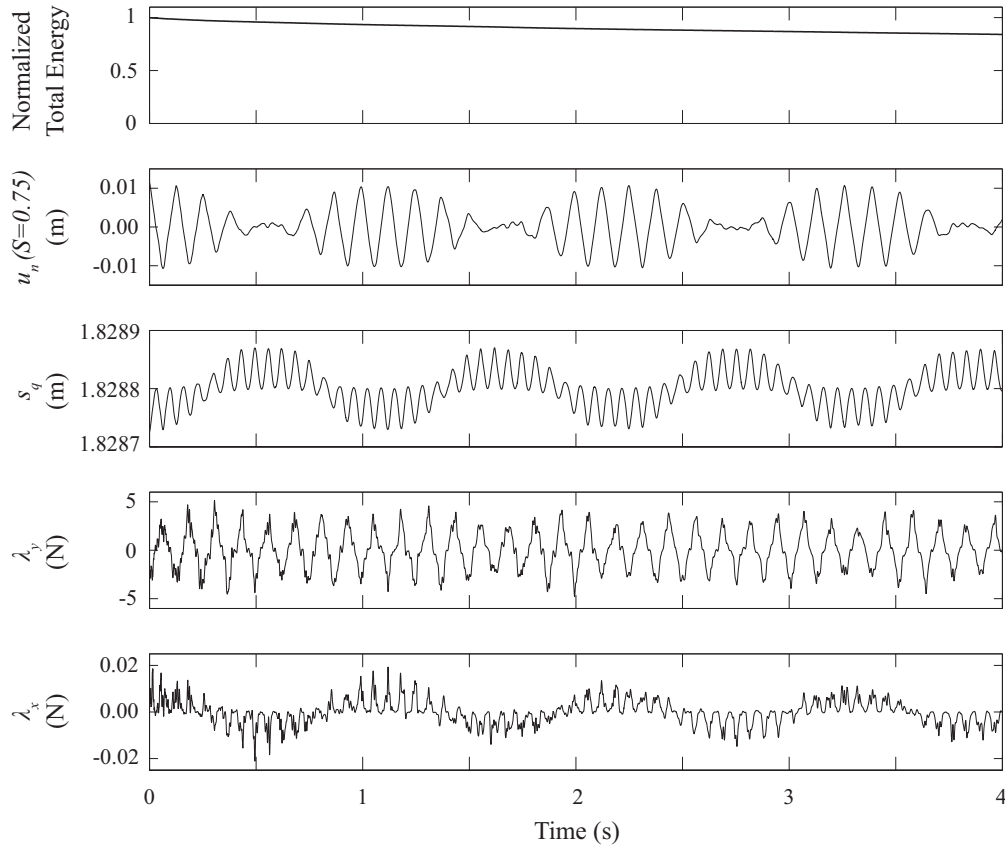


Figure 3.2 Plots of the system in free vibration: normalized energy; transverse displacement sampled at $S = 0.75$ or $s = 2.743$ m; material coordinate of the point Q in contact with the slider; constraint force in transverse direction; constraint force in axial direction.

The oscillatory behavior of the nonlinear beam can be clearly observed from Fig.3.2. The frequency of the transverse displacement u_n sampled at $S = 0.75$ or $s = 2.743$ m is approximately half of the frequency of the material coordinate s_q which corresponds to the point Q in contact with the slider. The frequency of the constraint force λ_y in transverse direction is strongly associated with the transverse vibration $u_n(S = 0.75)$, while the frequency of the constraint force λ_x in axial direction is strongly associated with s_q . Constraint forces also carry high frequency content. This

is due to the fact that constraint force is related to higher degrees of derivatives of u_n and u_t with respect to s . The total energy of the system was obtained by combining kinetic and strain energies and then normalized by the initial energy level. Energy decays slowly due to the presence of light material damping.

3.3.2 Numeric issue of computing the constraint force: Lagrange multiplier vs. penalty method

It has been shown in the previous subsection that the sliding dynamics can be solved using the numeric scheme that employs the Lagrange multiplier that gives rise to an algebraic problem. This leads to a system of extremely stiff equations (singular mass matrix) and makes the solution process very costly and time consuming. A special implicit solver that employs backward differentiation formulas had to be used but showed its inefficiency. The numeric example shown in the previous subsection took over 24 hours to complete with occasional manual intervention. Considering that the size of the example problem is actually small (64 unknowns in total), this time consumption is too high.

The author also explored the numeric scheme using the penalty method instead of Lagrange multipliers to solve for the constraint forces. In this structural problem, the penalty method essentially was applied by handling the constraint with large springs. In principle, any two degrees of freedom that are supposed to obey the kinematic constraint of being tied together rigidly are instead connected using a large spring. Then the constraint force can be derived from the internal elastic force of the spring given the stiffness of the spring and the relevant two degrees of freedom solved. Stiffness of the spring should be chosen by considering the trade-off between the constraint accuracy and the numeric expense. That is to say, if the spring stiffness is chosen to be very large, then the constraint and the constraint force could be simulated accurately, but numerically the problem may be too stiff and difficult to solve. On the other hand, if the spring stiffness is not set large enough, the numeric problem could be solved more easily, but the constraint modeling loses its accuracy.

The benefits of using the penalty method usually come from the fact that instead of using a special implicit numeric solver for DAEs, a general explicit solver can be used with a fixed time step. This makes the problem solving process more predictable in terms of time consumption, given a chosen time step that guarantees the numeric stability. However, after experimenting with the penalty method on this problem, the author found no apparent advantage of it in terms of numeric expense. Therefore the numeric simulations presented in the following all used Lagrange multipliers and DAE formulations.

3.4 Feedback control design of the slider motion

3.4.1 Preliminary design of the slider motion control

The control strategy using sliding mechanism is based on the idea of negative work. This idea simply explores that energy loss of the beam be facilitated by negative work done by the constraint force applied by the slider. When the slider is fixed in space, no actual work could be done by the constraint force and the total energy of the system is only dissipated through material damping, as shown in simulation results in the free vibration case. Since one can measure (in practice) or compute (in simulation) the axial constraint force Λ_x , it can be used as feedback in the control scheme. Instead of using a fixed constraint, the scheme prescribes the slider's X-direction motion X_C to be opposite to the direction of Λ_x to do negative work. This strategy can be realized by replacing the static constraint in Eq.(3.1) with a moving one as follows:

$$V_C = \dot{X}_C = \frac{\partial (U_t(S = S_Q, T) + S_Q(T))}{\partial T} \quad (3.28)$$

The constraint in Eq.(3.2) remains the same.

This control scheme is shown in Fig.3.3. Based on previous work done by Nudehi et al. (1992) and Issa et al. (2010), we choose the Lyapunov candidate as

$$V_1 = E_{total}(\mathbf{q}, \dot{\mathbf{q}}, T) \quad (3.29)$$

The origin of V_1 corresponds to the static equilibrium state of the beam. It is obvious that when the beam stays in static equilibrium, i.e., $\mathbf{q} = \mathbf{q}_0$ and $\dot{\mathbf{q}} = 0$, there is $V_1 = 0$. In the static state \mathbf{q}_0 has all entries zero but S_Q depending on the slider position. The change of total energy can only be caused by damping and the work done by the axial constraint force Λ_x if the X-direction displacement X_C of the slider is prescribed by the control scheme while the Y-direction displacement is always kept as zero, namely

$$\dot{E}_{total} = \dot{E}_{damping} + \dot{X}_C \Lambda_x \quad (3.30)$$

where $\dot{E}_{damping} \leq 0$. To implement this control scheme, the material boundary needs to be set since in practice the slider can only operate within a certain range of the beam. In order to realize $S_{lower} \leq S_Q \leq S_{upper}$, the slider position is further prescribed as

$$-\dot{X}_C = u = \begin{cases} h(y_1 = \Lambda_x) & \text{if } S_{lower} < S_Q < S_{upper} \\ 0 & \text{otherwise} \end{cases} \quad (3.31)$$

Substituting Eqs.(3.30) and (3.31) into Eq.(3.29) yields

$$\dot{V}_1 = \begin{cases} \dot{E}_{damping} - u y_1 = \dot{E}_{damping} - y_1 h(y_1) \leq 0 & \text{if } S_{lower} < y_2 = S_Q < S_{upper} \\ \dot{E}_{damping} \leq 0 & \text{otherwise} \end{cases} \quad (3.32)$$

For the choice of control input u in Eq.(3.31), it has been shown in Eq.(3.32) that it leads to $\dot{V}_1 \leq 0$. Using LaSalle's Theorem (Khalil, 2002), one can claim that the origin is asymptotically stable.

We now investigate the efficacy of the control design in Eq.(3.31) by simulation. The beam is again meshed using 20 elements, with the same properties and geometry shown in Table 3.1. Set material boundaries $s_{lower} = 1.33$ m and $s_{upper} = 2.33$ m for our simulation. In implementation, the material range $[s_{lower}, s_{upper}]$ for control is determined by the stroke length of the sliding device. The speed limit of the slider is set to be 1 m/sec. With the same initial conditions applied as in the free vibration case, results are shown in Fig.3.4 with dimensions.

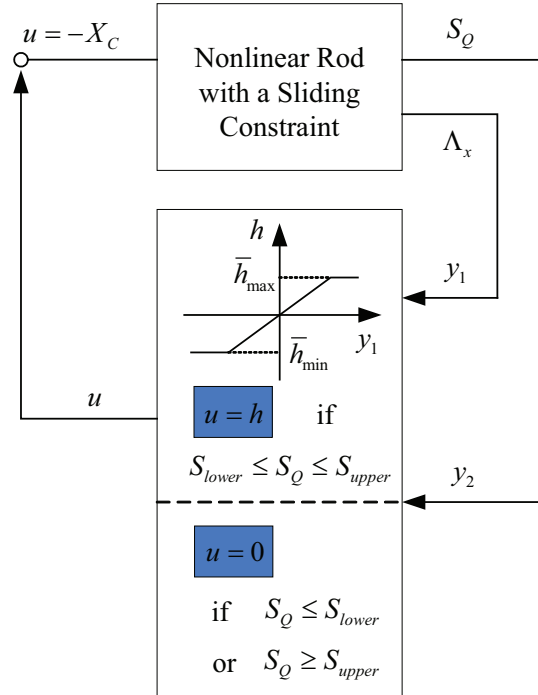


Figure 3.3 Preliminary feedback control design.

As shown in Fig.3.4, at the end of 12 sec, the total energy of the system was effectively dissipated to 1.0% of its starting level, while the transverse displacement at $S = 0.75$ was reduced to 17%. Most high frequency vibration was suppressed, as the history of $u_n(S = 0.75)$ shows, leaving the beam with slowly-varying residual transverse oscillations that should be fairly easy to cope with in application. The range of motion for the slider turned out to be within 0.2 m, which suggests that a relatively small travel distance suffices for the purpose of vibration suppression in this design. As the vibration energy was dissipated and the displacement of the beam was reduced, constraint force λ_x in X-direction decreased rapidly. This is because the geometric nonlinearity which gives rise to λ_x becomes less significant as the reduced amplitude of u_n decouples the interaction between u_n and u_t in the axial strain. One potential problem of this control design is that because of the high frequency components in λ_x , the position of the slider oscillates too fast in order to follow the change of λ_x , as one can see from the plot of \dot{x}_C . This may exceed the bandwidth of the actual actuator. The potential issue in implementation leads to our modified feedback control design, which is to be introduced next.

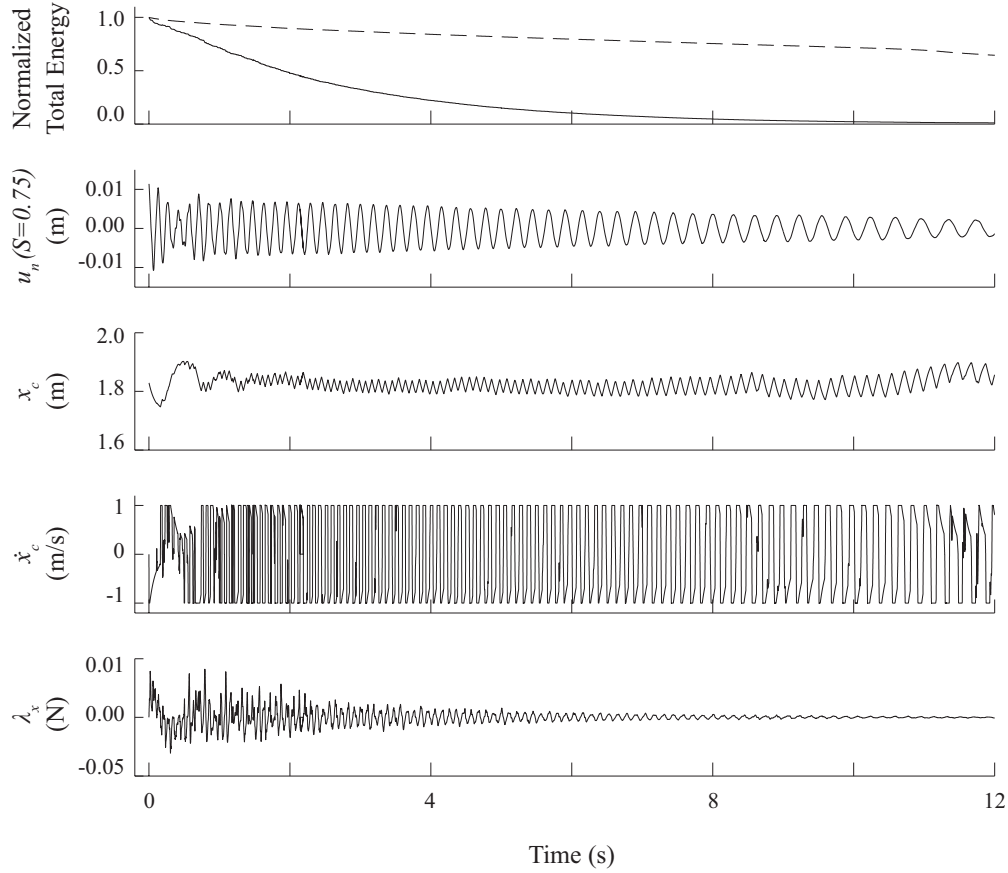


Figure 3.4 Plots of the system applied with direct control: normalized energy of the direct control results in solid line, normalized energy of free vibration in dashed line as reference; transverse displacement sampled at $S = 0.75$ or $s = 2.743$ m; slider position; slider velocity; constraint force in horizontal direction.

3.4.2 Modified control design

As stated in last subsection, when the slider is trying to follow the change of axial constraint force Λ_x , it may oscillate too fast that the hardware requirement exceeds the bandwidth of the actuator. To tackle this problem, we introduce a Low-Pass Filter (LPF) into the feedback loop, which measures Λ_x as its input and gives a signal z as the output. This LPF is chosen to be first order with the time constant τ . Instead of using Λ_x directly in the control law, we use the filtered signal z in the modified feedback control design. Choosing a new Lyapunov candidate, we can prove that the stability of the modified system can be retained.

The modified control scheme is shown in Fig. 3.5. Choose a new Lyapunov candidate as

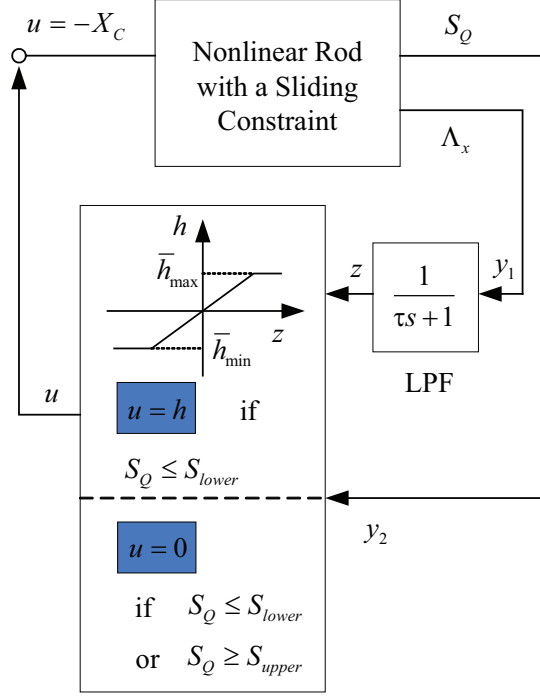


Figure 3.5 Modified control design with filter.

$$V_2 = E_{total} + \tau \int_0^z h(\xi) d\xi \quad (3.33)$$

The origin of V_2 corresponds to the static equilibrium state of the beam, i.e., $\mathbf{q} = \mathbf{q}_0$ and $\dot{\mathbf{q}} = 0$, where \mathbf{q}_0 has all entries zero but S_Q depending on the slider position. Use Eq.(3.30) we can obtain that when $S_{lower} < y_2 < S_{upper}$, the following holds:

$$\begin{aligned} \dot{V}_2 &= \dot{E}_{total} + \tau h(z) \dot{z} \\ &= \dot{E}_{damping} - y_1 u + h(y_1 - z) \\ &= \dot{E}_{damping} - z h \leq 0 \end{aligned} \quad (3.34)$$

And when $y_2 = S_Q \leq S_{lower}$ or $y_2 = S_Q \geq S_{upper}$, there is $\dot{V}_2 = \dot{E}_{damping} \leq 0$. Therefore using LaSalle's Theorem, again we can claim that the origin is asymptotically stable for the modified control system.

Following is the investigation of the efficacy of the modified control design by simulation. Meshing, material properties, geometric and control parameters, plus initial conditions were cho-

sen to be the same as in the preliminary control design. For the first-order low-pass filter, time constant τ was simulated as 40 ms. Results of simulation are shown in Fig.3.6 with dimensions.

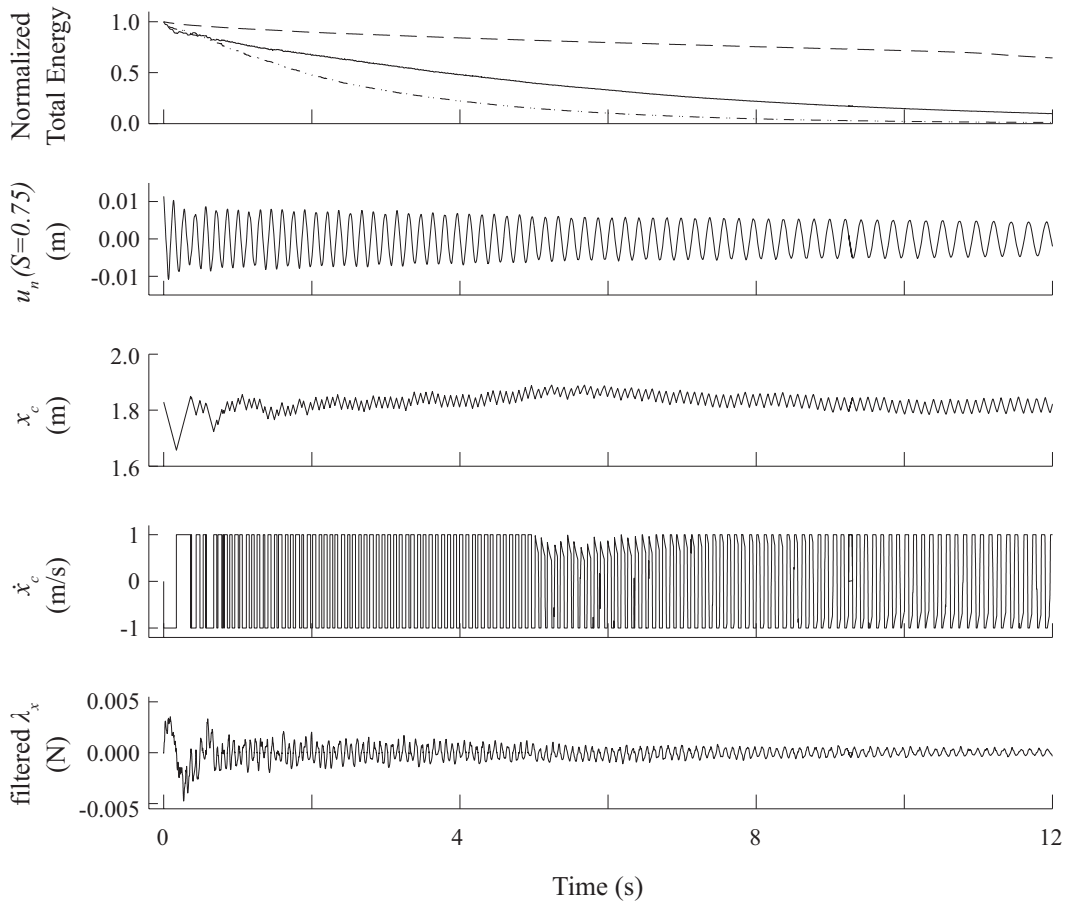


Figure 3.6 Plots of the system applied with direct control: normalized energy of the modified control results in solid line, normalized energy of free vibration in dashed line as reference, normalized energy of the direct control results in dotted-solid line as reference; transverse displacement sampled at $S = 0.75$ or $s = 2.743$ m; slider position; slider velocity; constraint force in horizontal direction after the low-pass filter.

Adding the low-pass filter is a trade-off between control efficiency and actuator bandwidth. As shown in Fig.3.6, the slider velocity \dot{x}_c driven by the actuator, switched less frequently compared with the preliminary design results, especially at the early stage (before 2 sec). This eases the requirement for the actuator bandwidth. The cost for this is that the vibration suppression process becomes less efficient. At the end of 12 sec, 9.7% of the total energy of the system remained. To achieve the same level of 1.0% suppression, compared to the control without a filter, the modified

design obviously requires longer time of the slider application.

In summary, up to this point, using the principle of virtual displacement and D'Alembert's principle, we have modeled a two-dimensional nonlinear beam with pinned-pinned boundary conditions and a frictionless sliding constraint. A variable-length finite element method (adaptive meshing) in the framework of ALE description was employed to discretize the dynamic system and to solve the equations of motion numerically. With the axial constraint force solved at any moment, the slider motion was prescribed to do negative work on the structure so that vibration can be suppressed. Numerical simulation results were presented to demonstrate the effectiveness of this control strategy. To meet the bandwidth requirement of the actuator, a nonlinear filter was placed in the feedback loop and asymptotic stability of the equilibrium configuration was established using Lyapunov stability theory. This method employing a sliding mechanism for vibration suppression in the flexible structure has been shown its great potential.

3.5 Combining slider motion with stiffness variation

With two vibration control strategies developed, this section looks into the combination of the two. In a general sense, as the slider moves and changes the contact point with the beam, the stiffness of the system varies. But this variation occurs continuously. In this context the stiffness variation is referred to specifically as the mechanism that varies the stiffness of the structure in a discontinuous way. Stiffness variation in the following is performed on the slider by treating the rotation of the slider as an on/off joint. When this joint is activated, the rotation of the slider is fixed, as well as the rotation of the contacted point of the beam. Numerically it is implemented by formulating a constraint on the rotational degree of freedom at the sliding node on the beam model. For such stiffness variation to be effective, the beam structure needs to have moderate damping present, which is very different from the system with light damping. In the latter case, as shown in previous sections, energy dissipation can not utilize the damping mechanism. It has to rely on the direct energy reduction means through sliding motion. With moderate damping present, as shown in

Table 3.2 Properties, geometry and other parameters of the beam system used in the validation simulation.

Material	Aluminum
Young's modulus E	69×10^9 Pa
Density $\bar{\rho}$	2700 kg/m^3
Damping coefficient η	10^{-3} sec
Beam length L	3.66 m
Beam cross section area	$38.1 \text{ mm} \times 1.57 \text{ mm}$
Pre-load (tensile) f	10 N
Added mass 1	0.66 kg
Added mass 2	0.66 kg

Chapter 2, energy redistribution in the frequency domain due to stiffness variation allows the high frequency energy to be dissipated rapidly.

If the sliding motion designed so far is referred to as "forward sliding" in terms of the direction of the motion prescribed, one can easily imagine that with light damping, the sliding should not be applied in the reverse way, for the reason that there would be energy continuously added by the sliding motion. Such energy will accumulate with no easy outlet through material damping, even if the energy exists in high frequency form. If reverse sliding is applied, the system will most likely go unstable or fail structurally in reality. However, if moderate damping is present, the combination of the reverse sliding and stiffness variation becomes possible, for damping may be significant enough to dissipate the energy added by the slider. Therefore, a combination involving reverse sliding will also be investigated.

3.5.1 Simulation of the system undergoing free vibration

Table 3.2 lists the properties, geometry and parameters used in the following simulation. The geometry of the beam was set to be identical as in the experiments to be presented in Chapter 4. So was the material properties such as Young's modulus and density. There were lumped masses added to the beam to decrease the natural frequencies of the structure. Mass 1 was located

at $s = 0.95$ m (1/4 of the beam length). Mass 2 was located at $s = 2.74$ m (3/4 of the beam length). The damping coefficient $\eta = 10^{-3}$ sec was the result of trials to approximate the decay rate obtained from the experiment results of a beam structure subjected to moderate damping (Chapter 4). The damping coefficient used now is significantly higher than the value $\eta = 10^{-5}$ sec used in earlier simulations.

Results of the free vibration case are shown in Fig. 3.7. The initial conditions of the free vibration and of all simulation cases were created by displacing mass 1 (located at $s = 0.91$ m) by 11.2 mm. After being released from its initial displacement, the beam underwent free vibration. During this process there was no sliding motion, but the slider was allowed to rotate freely.

Five quantities are shown in Fig. 4.7. They are: 1) axial force evaluated on slider, applied by the beam. 2) slope of the slider, indicating the rotational displacement at the contact point. 3) position of the slider, measured from left end of the beam, indicating the linear displacement of the slider. 4) transverse displacement of mass 1. 5) transverse displacement of mass 2.

Results of the axial constraint force and slider slope were basically obtained as the same order of magnitude compared to experiment results (to be presented in Chapter 4). Slider slope and displacements of the masses all show dominant frequency content in 2 ~ 3 Hz range. A low frequency envelope or beating behavior, was captured. The beating will be analyzed later in detail in Chapter 4. Dominant frequency component of the axial constraint force was twice of the dominant frequency component in transverse vibration, consistent with simulation results earlier. Low frequency component superimposed in the axial constraint force can be estimated as 0.2 Hz. This can be verified by a Fast Fourier Transform (FFT) analysis shown in Fig. 3.8.

Mass 1, directly displaced in the initial condition, had the displacement that started at the level of 0.011 m. At 10 sec, mass 1 displacement magnitude decreased to ≈ 0.006 m, 55% of the initial level. Mass 2, not directly excited by the disturbance, had the initial displacement of 0. As the vibration propagated from mass 1 and reached mass 2, its displacement started to increase and vary. At 10 sec, mass 2 also had the displacement of ≈ 0.006 m, estimated by observing the neighboring beating peaks. Vibration was evenly distributed on the two sides of the slider on the beam.

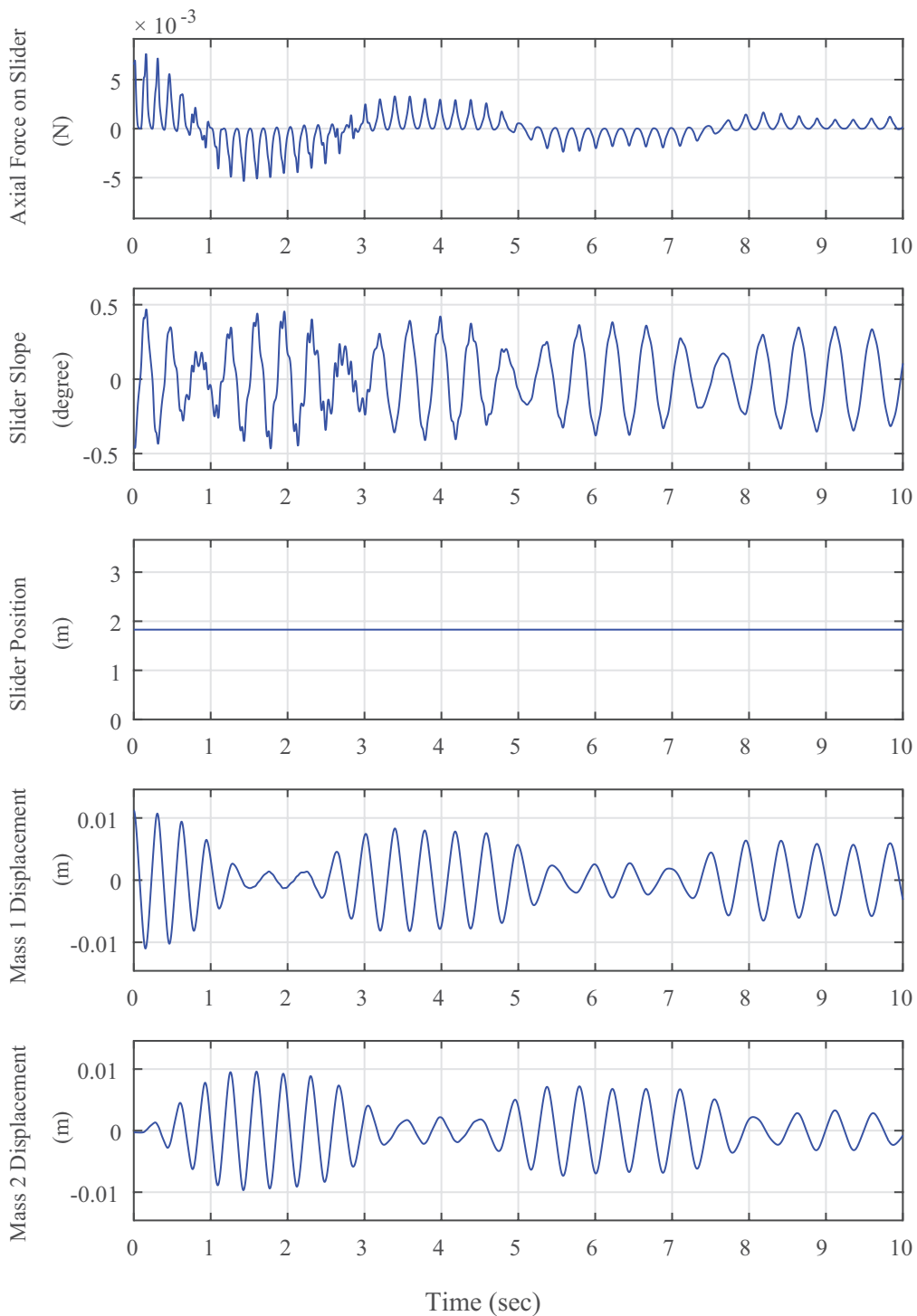


Figure 3.7 Simulation of the system under free vibration (time domain). Plots from top to bottom: axial force evaluated on the slider, applied by the beam; slider slope, or rotational displacement; slider position, measured from left end of the beam; displacement of mass 1; displacement of mass 2.

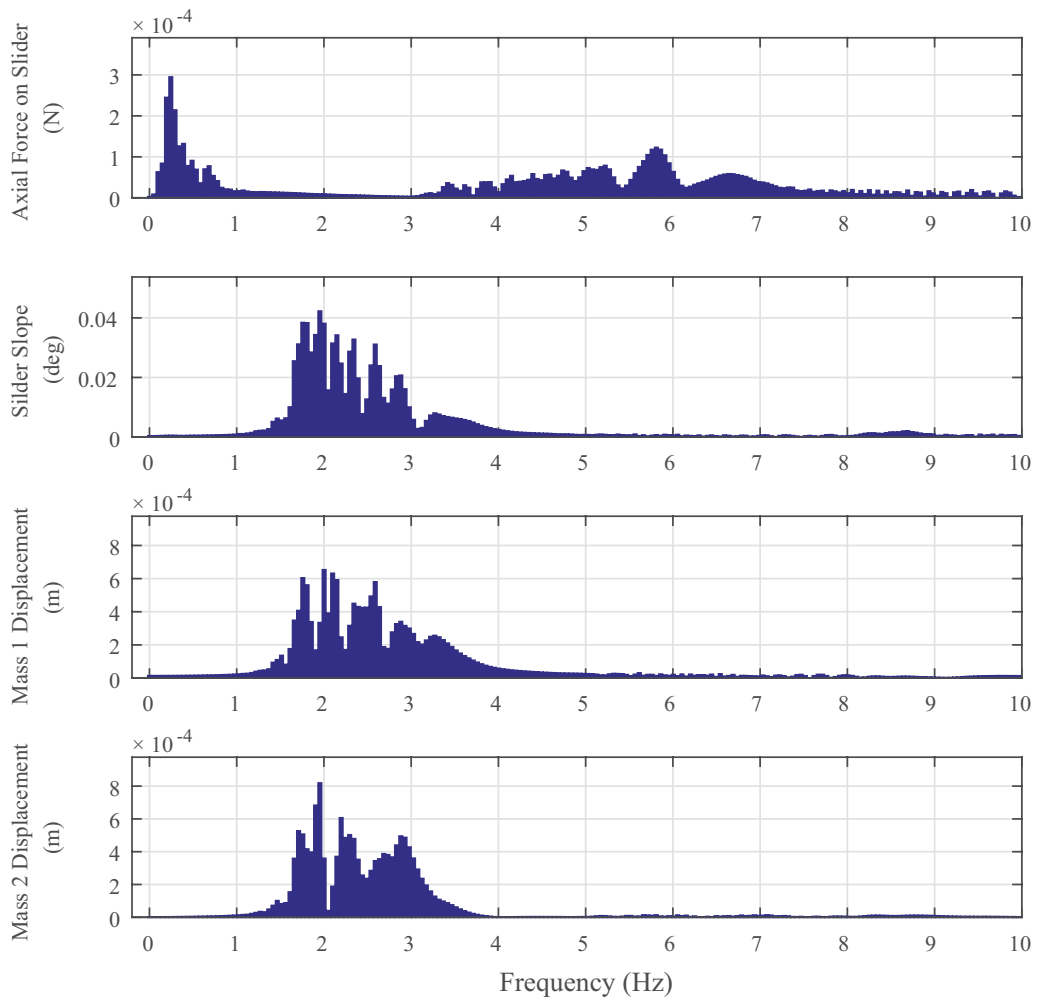


Figure 3.8 Simulation of the system under free vibration (frequency domain). Plots from top to bottom: axial force evaluated on the slider, applied by the beam; slider slope, or rotational displacement; displacement of mass 1; displacement of mass 2.

Also evaluated are the accelerations of two masses, as plotted in Fig. 3.9. Mass 1 had the acceleration that started at the level of 7.4 m/s^2 . At 10 sec, mass 1 acceleration decreased to $\approx 1.2 \text{ m/s}^2$, 16% of the initial level. Mass 2 had the initial acceleration of 0. At 10 sec, mass 2 also had the acceleration of $\approx 1.2 \text{ m/s}^2$, the plot was extended to 12 sec in order to better reveal the acceleration level as it may be covered in beats.

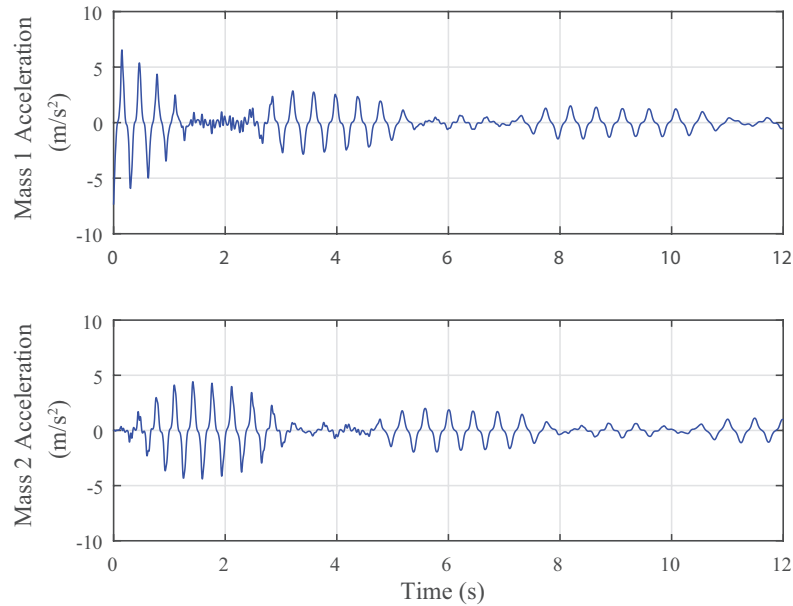


Figure 3.9 Simulation of the mass accelerations under free vibration.

A system energy history was evaluated and is plotted in Fig. 3.10. The system energy was computed by summing the potential energy and kinetic energy of the beam with added masses. The plot shows that the total energy started at 15.3 mJ and decreased to 2.1 mJ at 10 sec, with 14% remaining. This means 86% of the energy was dissipated through material damping. The system has moderate damping level that is comparable to what was observed in experiments (see Chapter 4).

With a reasonably model established above through free vibration evaluation, the combination of control methods were investigated in the following.

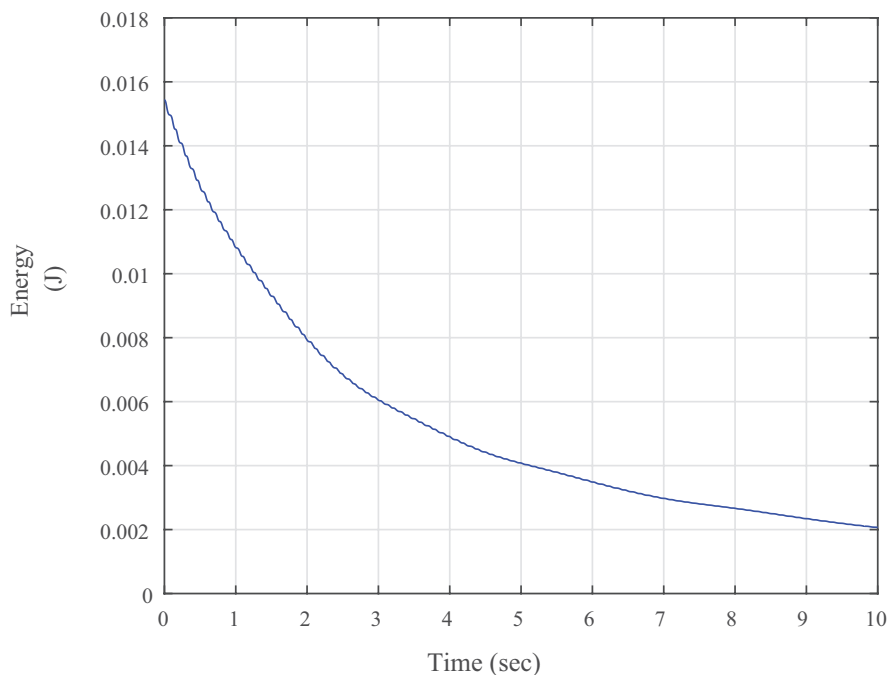


Figure 3.10 Simulation of the system energy under free vibration.

3.5.2 Simulation of the system employing sliding control only

First is the case employing sliding mechanism only. Results of simulation were produced using the same initial condition as in the free vibration case shown in Fig. 3.11. The slider moved at the maximum velocity of 1 m/s. A stroke length of 1.76 m was assumed. This length set the material boundary right before the slider reaches the two masses. The slider velocity was set to be zero as it hit the material boundary and continued with the direction of attempting to go over the boundary. Same algorithm was applied, as shown in Fig. 3.3. One can clearly see the upper material boundary being reached in Fig. 3.11. For most of the time in the 10 sec interval, the axial force on the slider was in positive X-direction, or towards the right end of the beam.

Displacement of mass 1 started at the level of 0.011 m. At 10 sec, mass 1 displacement decreased to ≈ 0.007 m, 64% of the initial level, higher compared to the free vibration case in which the value became ≈ 0.006 m. This defeats the purpose of vibration reduction. Or it can be understood as the direct energy removal by the slider could not compete with the moderate damping

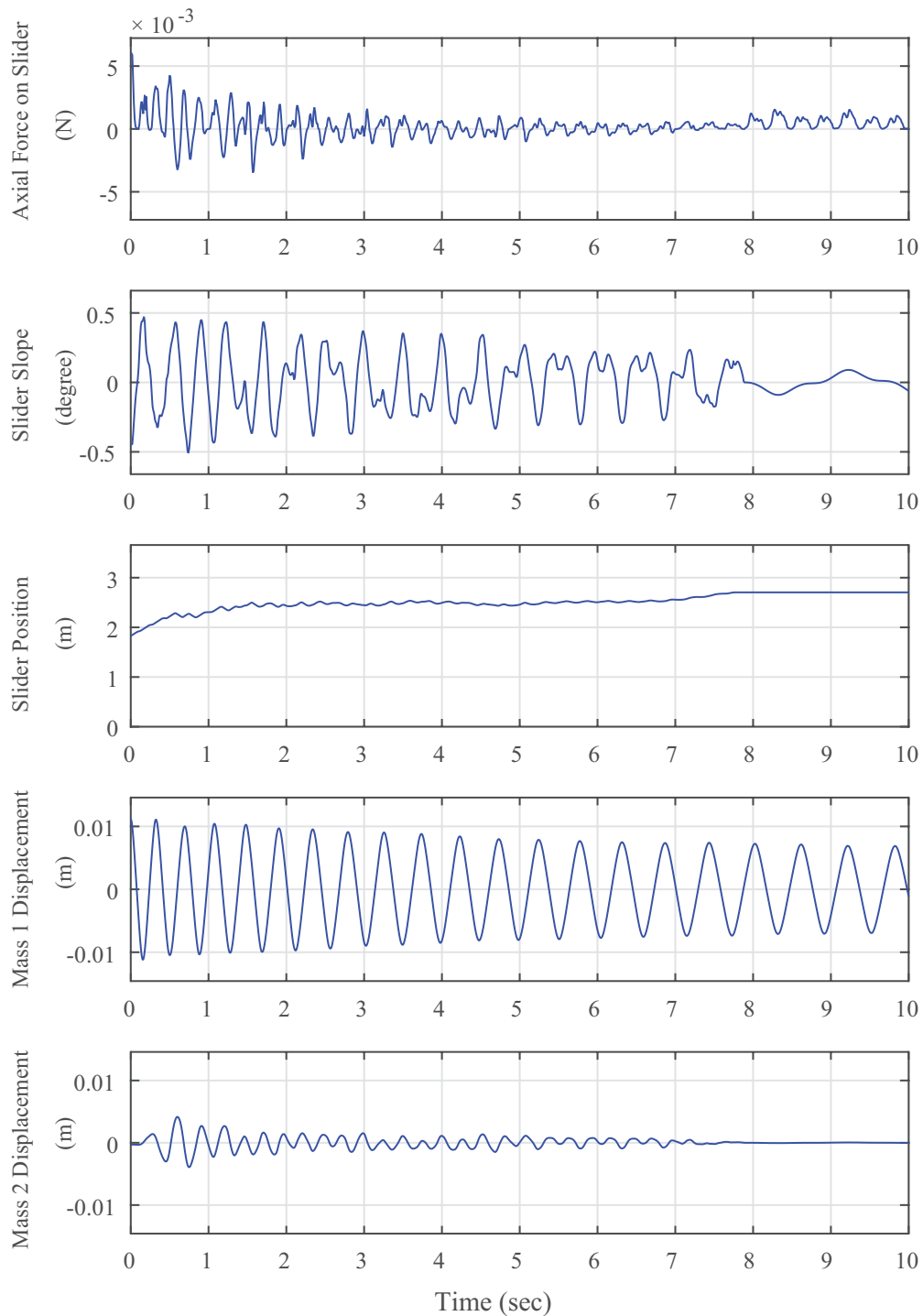


Figure 3.11 Simulation of the system under sliding control only. Plots from top to bottom: axial force measured on the slider, applied by the beam; slider slope, or rotational displacement; slider position, measured from left end of the beam; displacement of mass 1; displacement of mass 2.

rate. Mass 2, not directly excited by the initial disturbance, had the initial displacement of 0. After some oscillation, mass 2 displacement decreased back to 0, which showed the effect of vibration suppression. Similarly, accelerations results were extracted. Results are listed together in Table 3.3 for comparison.

The vibration was not effectively suppressed by the sliding mechanism alone. A conjecture was then made that the direct energy removal rate by the slider may not be fast enough to create a meaningful difference compared to the free vibration case. Based on this conjecture, the following evaluation was performed.

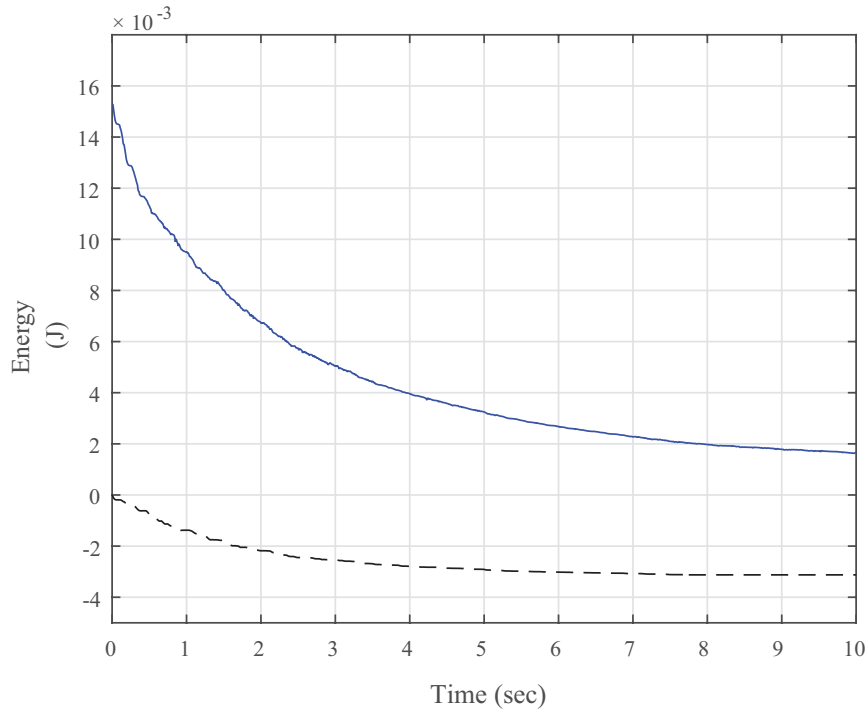


Figure 3.12 Simulation of the system energy under sliding control only. Solid line shows the total energy of the beam system. Dashed line represents the energy change directly due to the sliding motion.

The energy of the system are plotted in Fig. 3.12. The solid line shows the total energy of the system. The dashed line represents the energy change directly due to the sliding motion. The total energy of the system started from 15.3 mJ and decreased to 1.7 mJ at 10 sec. The total energy was reduced by 89%, slightly better than the free vibration case (86% reduction through material

damping only, no control). What is interesting is that evaluation of the energy change directly due to sliding motion shows that the slider kept reducing the energy of the system (thereby negative value for energy change). At 10 sec, the sliding motion reduced the system energy only by 3.1 mJ, which accounted for 20% of the total energy at 0 sec. This shows that the main portion of the energy decay was due to material damping (69%), not due to the direct energy removal by sliding. Direct energy removal by sliding was not efficient compared to material damping.

3.5.3 Simulation of the system employing sliding control combined with stiffness variation

Using the consistent parameters and initial conditions, the simulation continued with the case using the control method combining stiffness variation and forward sliding mechanism. It is referred to as "forward sliding" for the direction of the sliding motion is the same as the algorithm originally designed in Section 3.4, as opposed to "reverse sliding", which will also be investigated.

In the following simulation, the sliding motion was independent from the activating/deactivating operation for stiffness variation, meaning that the slider could still move regardless of the rotational on/off joint status. Stiffness variation was activated and deactivated cyclically. In simulation, the activation occurred exactly at the instances when the slider slope passed 0. It was kept activated for 0.1 sec, then was deactivated and released the slope for another 0.1 sec. After that the rotational on/off joint waited for the next instance of activation and the cycle went on.

Results of this case are shown in Fig. 3.13. The axial force on the slider had a positive value for most of the time. It is consistent with the fact that the overall slider moved in a positive direction towards the right end of the beam. After 5 sec, the sliding motion stopped due to the material boundary. Stiffness variation was activated and deactivated cyclically throughout the whole process, as reflected in the slider slope plot. The displacement of mass 1 started at the level of 0.011 m. At 10 sec, mass 1 displacement decreased to ≈ 0.006 m, 55% of the initial level, not more effective compared to the free vibration case. Mass 2, not directly excited by the initial disturbance, had the initial displacement of 0. After some oscillation, mass 2 displacement decreased back to 0, which showed the vibration suppression effect. Similarly, accelerations results

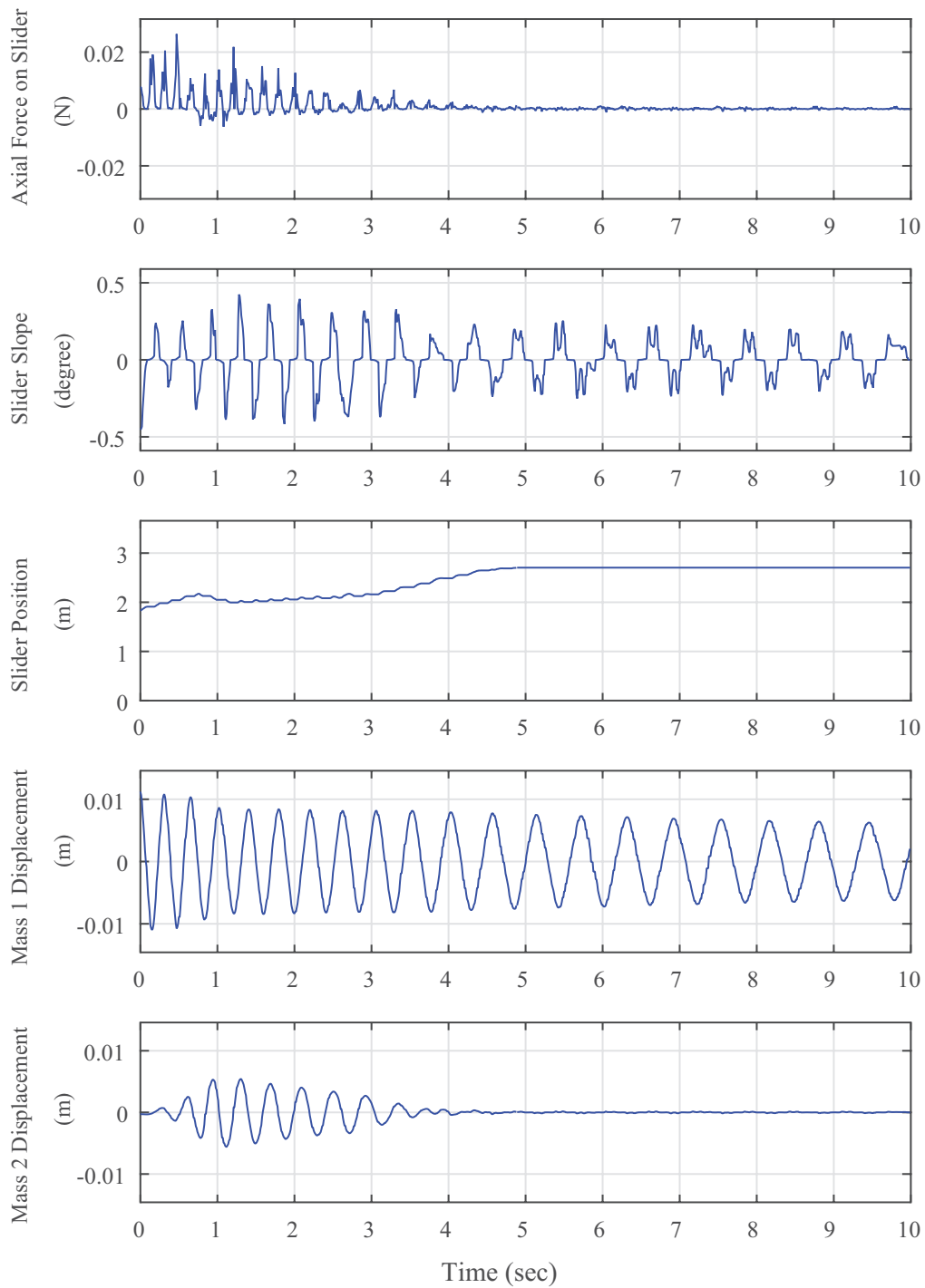


Figure 3.13 Simulation of the system under combined control of stiffness variation and forward sliding mechanism. Plots from top to bottom: axial force measured on the slider, applied by the beam; slider slope, or rotational displacement; slider position, measured from left end of the beam; displacement of mass 1; displacement of mass 2.

were extracted. Results are listed together in Table 3.3 for comparison.

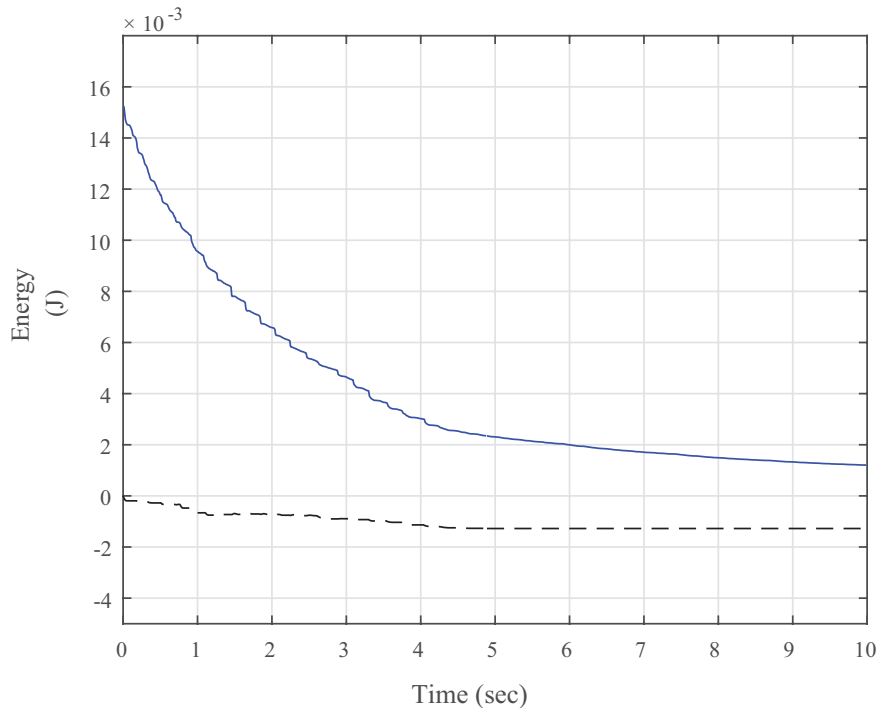


Figure 3.14 Simulation of the system energy under combined control of stiffness variation and forward sliding mechanism. Solid line shows the total energy of the beam system. Dashed line represents the energy change directly due to the sliding motion.

More insight can be gained from the energy plot. As shown in Fig. 3.14, the total energy of the system started from 15.3 mJ and decreased to 1.2 mJ at 10 sec. The total energy was reduced by 92%, a little better than the free vibration case in which there was 86% reduction through material damping only, no control. Evaluation of energy change directly due to the sliding motion shows that the slider kept reducing the energy of the system (thereby negative value for energy change). At the 10 sec, the sliding motion had reduced the system energy only by 1.3 mJ, which accounted for 9% of the total energy at 0 sec. This again shows that the main portion of the energy decay was due to material damping (83%), facilitated by material damping, and can not be attributed to the direct energy removal by sliding.

In an effort to improve the performance using the current configuration, a completely new combination was then explored. This combination also involves stiffness variation and sliding

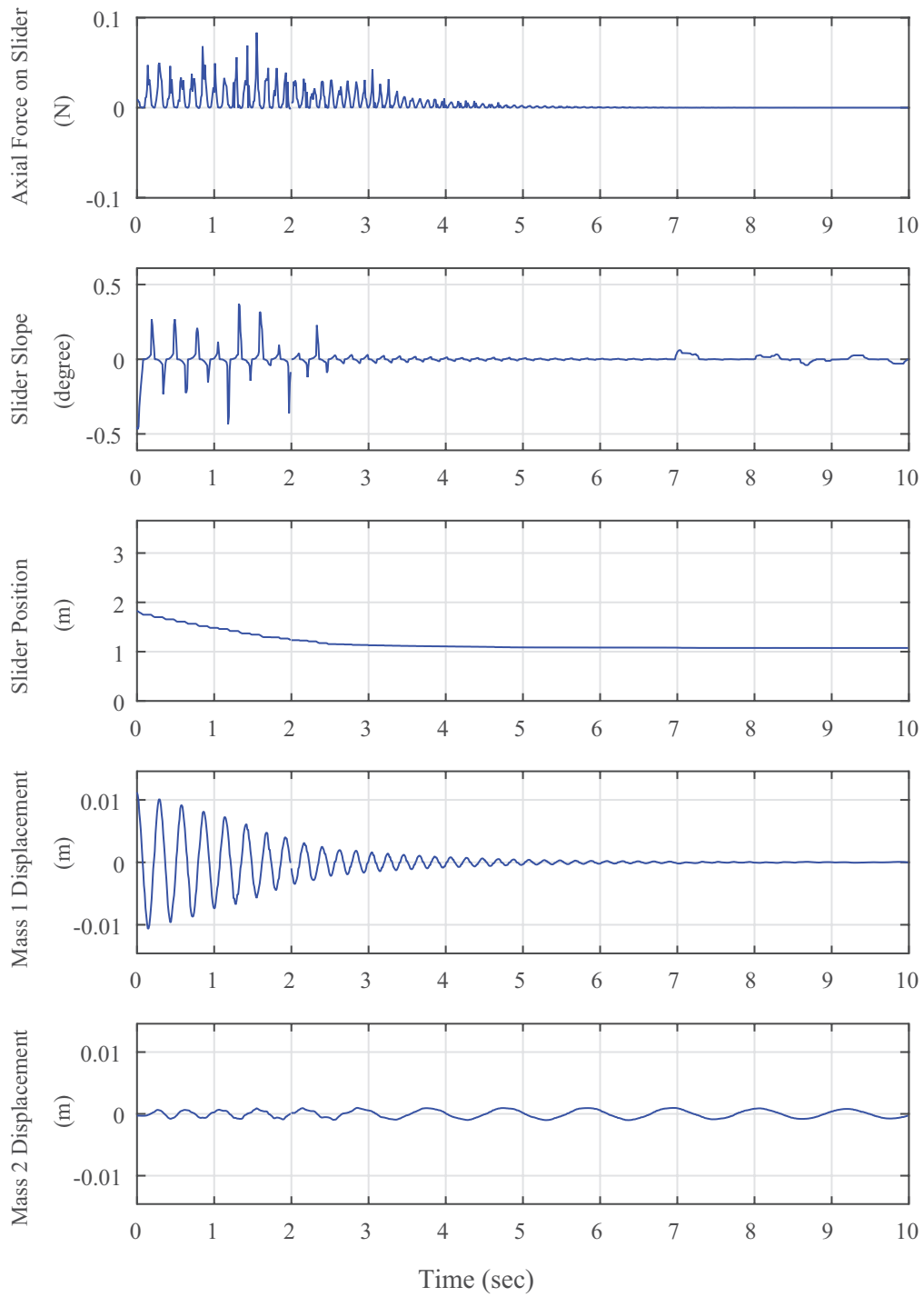


Figure 3.15 Simulation of the system under combined control of stiffness variation and reverse sliding mechanism.

mechanism. But instead of sliding according to the algorithm presented before, the sliding motion was carried out in the reverse direction.

Theoretically, if sliding in the reverse direction, always opposite to what the original algorithm suggests in any moment, slider continuously adds energy into the system. This seems to be hurting the purpose of vibration suppression. But there are potential benefits of doing so. It has been observed and the conjecture has been validated that through sliding approach, the direct energy removal rate only may not be fast enough to create a meaningful difference compared to the free vibration case. The main portion of energy decay was still due to the contribution internal material damping. The hope of applying reverse sliding is that if the slider keeps moving towards the side with higher axial force, it may dramatically reshape the energy spectrum in the frequency domain. The sliding motion will directly add some energy. But if it creates a much higher material damping rate, the results of the tradeoff may yield faster energy decay overall.

Therefore, the case of combining reverse sliding and stiffness variation was simulated. Simulation results are shown in Fig. 3.15. Axial force on the slider almost always had a positive value. The slider moved almost monotonically in negative direction towards the left end of the beam, for it was controlled in the reversed way. It can be understood as that the slider was always "moving against the wave", towards one part of the beam that exerting more axial force. After 3 sec, sliding motion was barely observed due to the material boundary. Stiffness variation was activated and deactivated alternatively throughout the whole process, as reflected in the slider slope plot. Displacement of mass 1 started at the level of 0.011 m. At 10 sec, mass 1 displacement decreased to less than 0.0001 m, which is less than 1% of the initial level, showing significant vibration reduction. Mass 2, not directly excited by the initial disturbance, had the initial displacement of 0. After some oscillation, mass 2 displacement decreased to 0.0007 m, 7% compared to the initial level of mass 1. Similarly, accelerations results were extracted. Results are listed together in Table 3.3 for comparison.

The mechanism of the energy change is more revealing from the energy plot. As shown in Fig. 3.16, the total energy of the system started from 15.3 mJ and decreased to 0.05 mJ at 10 sec. The

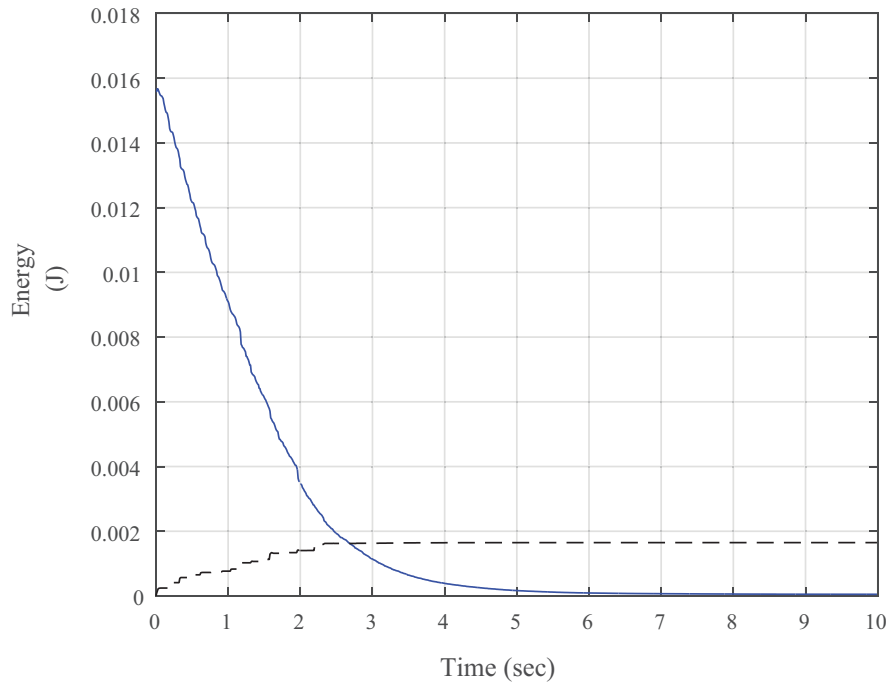


Figure 3.16 Simulation of the system energy under combined control of stiffness variation and reverse sliding mechanism. Solid line shows the total energy of the beam system. Dashed line represents the energy change directly due to the sliding motion.

total energy was reduced by 99.7%, showing successful vibration reduction compared to the free vibration case. Evaluation of energy change directly due to the sliding motion shows that the slider kept adding energy to the system (thereby positive value for energy change). At 10 sec, the sliding motion had added 1.6 mJ, which accounts for 10% of the total energy at 0 sec. This means that material damping practically dissipated 110% of the initial level of the system energy.

Apparently, by applying reverse sliding control the slider keeps moving towards the side with higher axial force. This indeed dramatically reshapes the energy spectrum in frequency domain. The sliding motion could add some energy (10%). But it creates a much more material damping, which is facilitated by stiffness variation. The net effect is much faster energy decay overall. In this way vibration seems to be significantly suppressed.

Combinations of the two control strategies provide the insight of how a real structure with the similar configuration and dimension may behave under control, as the structure in experiments

Table 3.3 Comparison of performance of different control strategies. All relative displacements and accelerations are computed using the mass 1 initial status as reference.

Control Condition	Mass 1 Relative Accel at 10 sec	Mass 2 Relative Accel at 10 sec	Mass 1 Relative Displacemt at 10 sec	Mass 2 Relative Displacemt at 10 sec	System Energy Remained at 10 sec
Free Vibration	55%	55%	16%	16%	14%
Sliding Only	64%	0%	14%	0%	11%
Forward Sliding and Stiffness Variation	55%	0%	16%	1%	8%
Reverse Sliding and Stiffness Variation	1%	6%	0%	7%	< 1%

usually have moderate damping present. The next chapter presents the experimental study of a system with two control strategies implemented and applied.

CHAPTER 4

EXPERIMENTAL STUDY OF VIBRATION SUPPRESSION THROUGH STIFFNESS VARIATION AND SLIDING MECHANISM

4.1 Experiment design

An experimental setup is presented in this chapter. The content to be shown starts from conceptualization and design in Section 4.1, followed by implementation and operation in Section 4.2. Section 4.3 shows the results of this experimental platform that validate the vibration suppression strategies proposed.

4.1.1 Tension-aligned structure

The basic structure under study follows the design depicted in Fig.3.1. The system should consist of two parts: 1) A flexible tension-aligned beam structure. 2) A relatively rigid support structure. Furthermore, there are the following considerations when designing the system on the structural level:

1. The beam under tension should be flexible and light-weight. These features make the beam exposed to noticeable vibration problem due to external disturbances, meanwhile sensitive to control force from the actuators. Since low-frequency vibration is the main target in this study, there is a trade-off between flexibility and light-weight. To manufacture a structure with low natural frequencies, the stiffness needs to be as low as structural stability allows (flexibility), while the structure needs to carry a reasonable amount of mass. On the other hand, the amount of mass of the beam should be kept small (light-weight) to allow actuators with reasonable driving power to be able to change the dynamics of the beam.
2. At the two ends of the beam, there needs to be a stable and easy-to-realize tension device that imparts enough tension to the beam. After the pre-tension is applied, there ought to be a

locking mechanism on this tension device that maintains a constant boundary condition for the beam (pinned-pinned). This is to guarantee that while the beam is undergoing vibration, the tension device does not add unexpected dynamics to the system.

3. Because one control strategy involves a sliding mechanism, the surface of the beam should be hard and smooth on which the slider operates. Also although the sliding motion is designed to be along the axial direction of the beam, deviation from the axis is almost unavoidable. Therefore, the beam needs to have enough width to tolerate the motion error. But the width can not be too large to produce any torsional displacement that is not accounted for.
4. The support structure should be rigid enough so that the vibration of the tension-aligned beam does not interact with the support structure. Ideally, one wants the beam to be directly grounded through the tension device to eliminate any unwanted dynamics and concentrate the study only on the beam itself. But in reality, the system including a complex sliding actuator needs to be mounted on a platform-like support structure. One then has to design a structure that has the comparable size of the beam and be much more rigid so that the influence from the vibrating parts (beam, actuators) on the support structure are minimized.

4.1.2 Stiffness variation mechanism

Stiffness variation as our first proposed vibration control strategy was implemented in two ways in simulations. One way was to use a rotational on/off joint that can be fairly easily realized on a continuous beam. This is to use a clamping device that has an on/off locking mechanism. The other way is to connect the beam to the support structure through a translational spring of time-varying stiffness. This is rather expensive to construct and difficult to engineer.

The experiment design chooses the rotational on/off joint as the means for stiffness variation. In addition, as described in Section. 4.1.3, the location of the joint, i.e., the contact point with the beam, can be varied or moved on the surface of the beam, along the beam's axial direction. This

further varies the stiffness of the beam. This differs from the situation in Section 2.3 or in Section 2.4, where the on/off joints are fixed at the locations of the discrete hinges between panels.

4.1.3 Sliding mechanism

The design of the sliding mechanism considers the following factors:

1. The slider needs to have enough stroke span to cover a significant portion of the beam's total length. It also needs to have significant frequency bandwidth and speed to cope with the beam dynamics. This is due to fact that the control algorithm dictates that the sliding motion closely follows the change in the constraint force. As the numeric simulation reveals, this requires the bandwidth of the slider to be twice compared to the beam's transverse frequency that is to be suppressed after excited by external disturbances.
2. The slider needs to be always in contact with the beam surface as it moves. Note that the beam surface or the sliding motion will not be perfectly smooth or straight. It is necessary to create a slider contact interface that is not absolutely rigid but has some compliance to tolerate these imperfections. Otherwise it is possible for the slider to damage the surface of the beam or even worse to destabilize the beam by the sliding itself.

4.2 Experiment implementation

4.2.1 A nonlinear beam

In order to explore nonlinearity in the beam vibration, which is essential to validate the vibration suppression strategy through sliding mechanism, the beam ought to be both flexible and slender. Flexibility requires low Young's modulus of the material to be used. That allows the beam to undergo relatively large vibration displacement caused by moderate disturbance. Slenderness is needed because geometric nonlinearity stems from large transverse displacement compared to the beam's thickness. In other words, the beam needs to be thin enough. Considering the beam

surface will be constantly exposed to the slider contact, it is preferable to use metal material to resist the wear for durability consideration. The beam was therefore chosen to have the properties and geometry as shown in Table 4.1. The beam was estimated to have a 20 mm displacement as the initial condition, this is over 10 times its thickness, which provides significant geometric nonlinearity.

Table 4.1 Properties and geometry of the beam used in experiment.

Material	Aluminum
Young's modulus E	69×10^9 Pa
Density $\bar{\rho}$	2700 kg/m ³
Beam length L	3.66 m
Beam cross section area	38.1 mm \times 1.57 mm

The beam was connected to the support structure through the tension device using a pinned-pinned boundary condition. This boundary condition, compared to other boundary conditions, has the flexibility that keeps the natural frequency of the beam low.

4.2.2 Added mass

Lumped masses were added on the beam to lower the natural frequency. Two masses were attached on the beam. Mass 1, with the weight of 0.33 kg, was located at $s = 0.95$ m (1/4 of the beam length). Mass 2, with the weight of 0.32 kg, was located at $s = 2.74$ m (3/4 of the beam length).

4.2.3 Tension device

The tension device or the tensioner employed a crank mechanism to stretch the beam at its one end. The crank rotation was converted to linear displacement through a shaft track which was axially aligned with the beam and a pair of bushings mounted on it. A force sensor was connected between the crank and the beam to make sure a desired tension level was achieved. After the pre-tension was applied, the tension device provided a locking mechanism through fastening screws to the track

which no longer allowed any axial movement of the beam. This maintained a constant boundary condition for the beam (pinned-pinned). The beam inevitably slacked after initial mounting due to gravity. The tension device turned out to be extremely important in the experiment setup in maintaining the straightness of such a long beam.

4.2.4 Sliding motion control

Sliding motion was provided by the Thomson Tollo M50 belt drive actuator, depicted in Fig. 4.1. This actuator was powered by a Kollmorgen AKM23E brushless servo motor through a 5:1 gear reducer. The motion control was implemented by a Kollmorgen AKD-P00306 programmable amplifier.

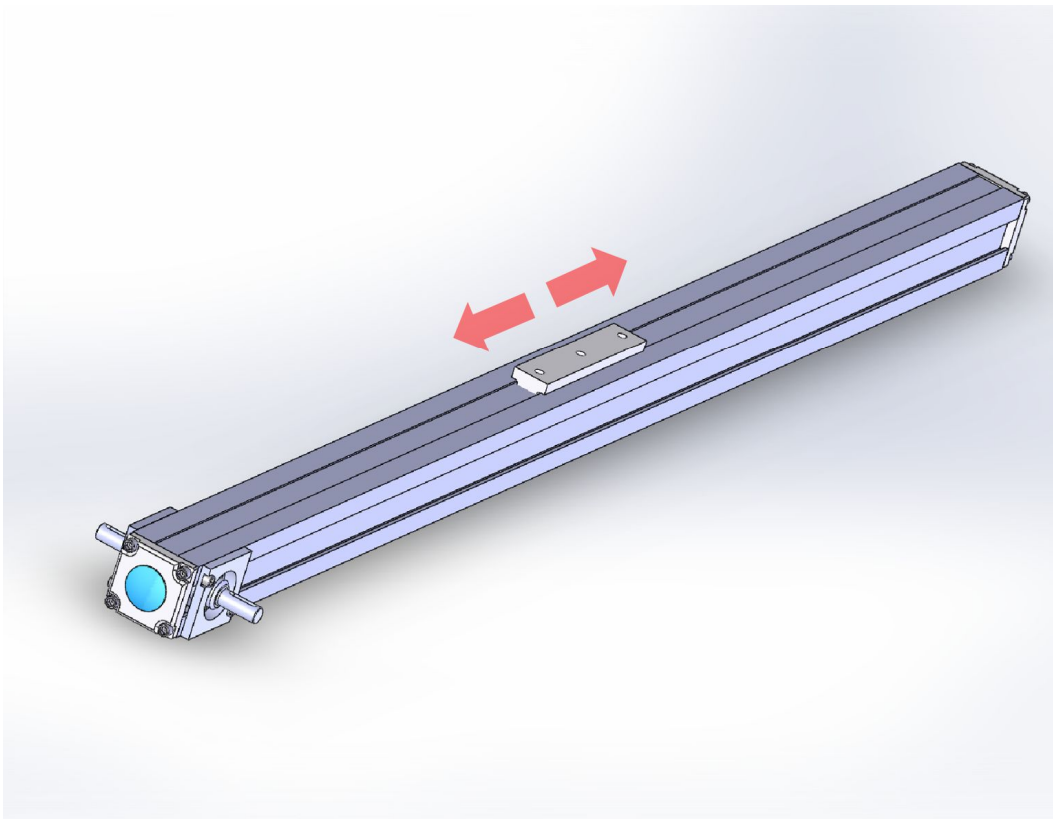


Figure 4.1 Belt drive actuator to provide sliding motion.

4.2.5 Rotational on/off mechanism

The slider was a moving joint in contact with the beam surface. It extended from the contact point downwards with a shaft and sat on a carriage driven by the sliding actuator. The carriage had a rotational on/off mechanism on the slider shaft. This controllable on/off mechanism was realized by an electromagnetic brake that was flange mounted to the carriage. Also installed in the carriage was an encoder which the slider shaft goes through, as shown Fig. 4.2. The encoder measured the rotation of the slider shaft as part of the feedback information.

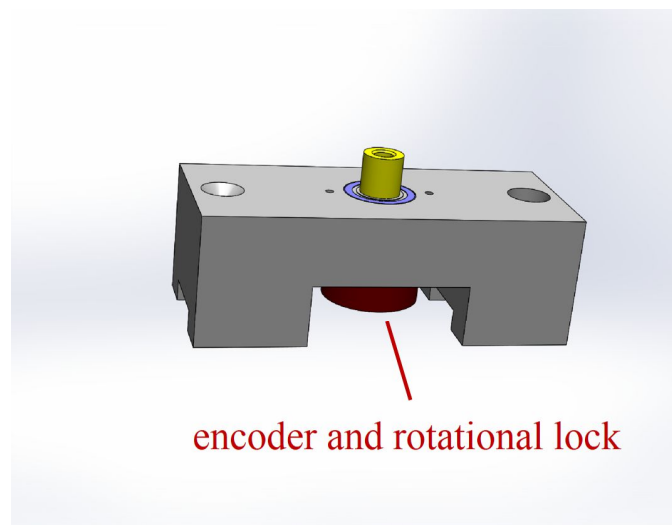


Figure 4.2 The slider carriage that consists of rotational on/off mechanism and encoder to measure the rotation. A slider shaft is to be assembled on to the carriage.

4.2.6 Slider contact interface

The contact interface between the slider and the beam used ball plunger to provide some compliance. Ball plungers are cylindrical parts with rotational spheres at the tip which minimize the friction on the beam surface. The spheres are loaded with springs inside the cylindrical body which allows limited linear displacement. One pair of ball plungers provided two contact points on each side of the beam. In total four ball plungers were used and created four contact points. On each side the two contact points were separated by 76 mm so that this portion of the beam had controllable slope to implement stiffness variation for the purpose of vibration suppression.

The ball plungers were mounted on a fork-like structure through two plates. The two arms of the fork structure were equipped with force sensors made of strain gauges as shown in Fig. 4.3. The force in the normal direction of the beam surface at the contact points was also part of the feedback information.

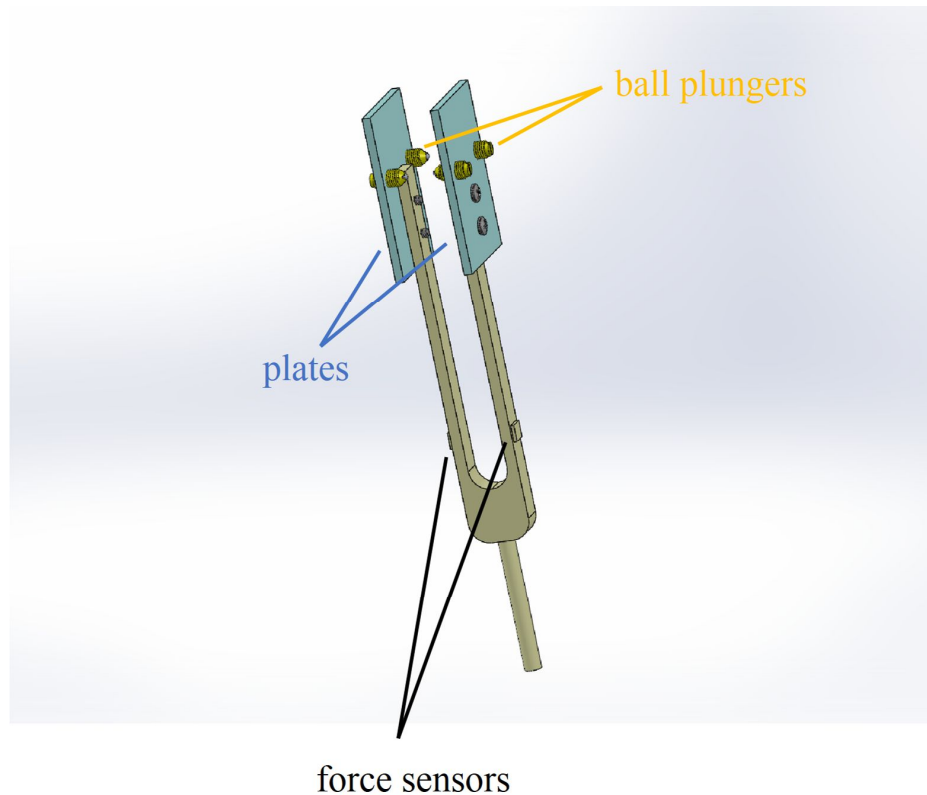


Figure 4.3 Slider contact interface with force sensors.

The assembled beam with the sliding interface that sits on the carriage of the sliding track is depicted in Fig. 4.4.

4.2.7 Measurement for feedback information and the system status

The complete set of feedback information was measured through the following sensor systems: 1) encoder on the slider shaft measuring slider slope or rotation angle; 2) strain gauges measuring the force on the slider, applied by the beam with the direction normal to the beam surface; 3) belt-driven actuation system monitoring slider position. Among these, 1) and 2) were further combined

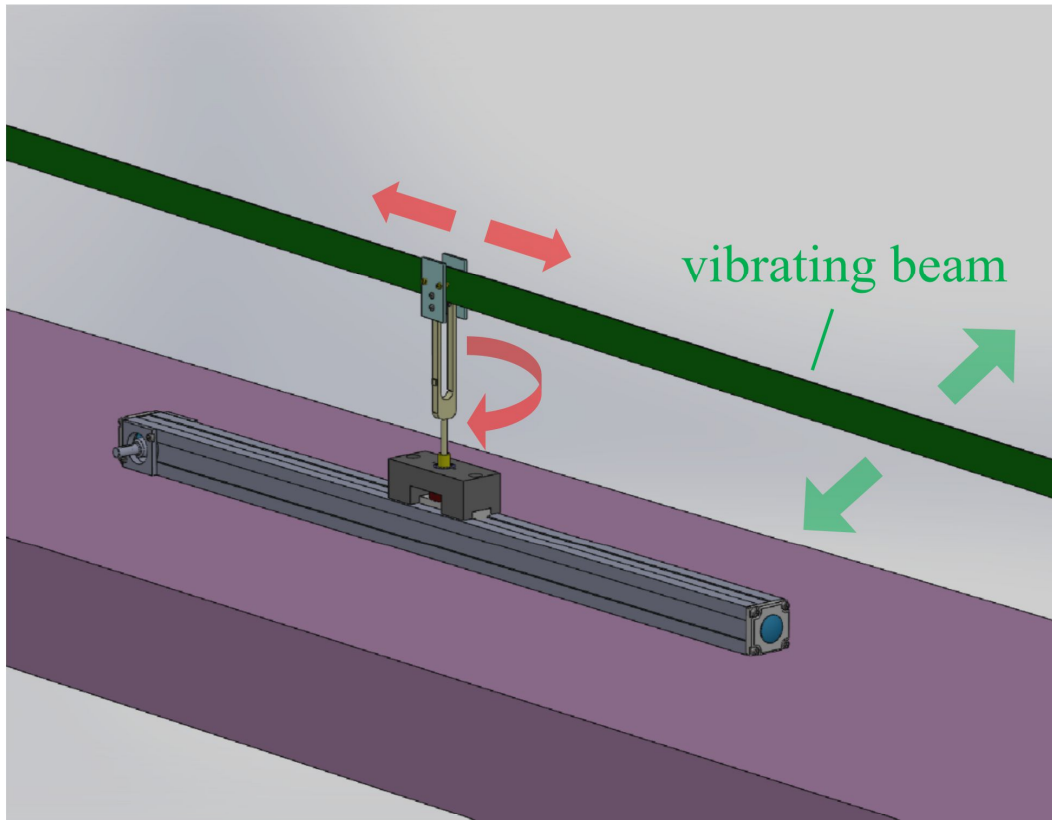


Figure 4.4 Assembled parts of sliding and rotational mechanism fixed on the support table in contact with the vibrating beam.

and processed to derive the axial force applied by the beam to the slider. This force is equal in magnitude to the constraint force in X-direction, i.e., Λ_x .

Besides feedback measurement, two accelerometer were mounted on the two added masses respectively to monitor and record the system status.

4.2.8 Data acquisition

Measurements obtained from sensors were acquired using a dSPACE DS1104 controller board. The controller board provided A/D and D/A converters, as well as digital I/O interface. It is programmable from Simulink block diagram environment. The DS1104 board was connected with a PC through PCI bus.

4.2.9 Real-time control and data processing algorithm

Real-time data acquired and transmitted from the controller board at the sampling rate of 1 kHz and was processed in the PC by a control software written in a Simulink environment. The signal flow of the algorithm followed the design shown in Fig. 3.5. There was also a graphic user interface for control operation. The interface, as shown in Fig. 4.5, was configured in the ControlDesk software tool provided along with the dSPACE controller hardware.

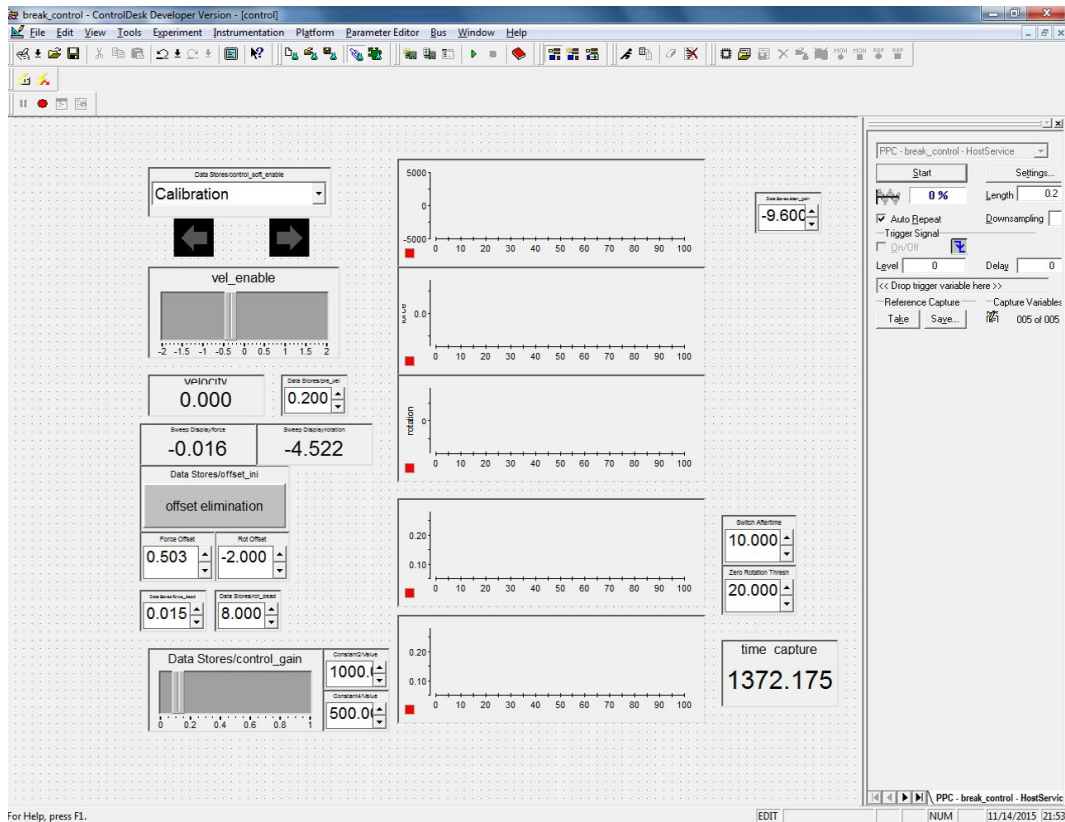


Figure 4.5 Interface of the real-time control and data processing software.

4.2.10 Initial displacement holder

To create consistent initial conditions for each experiment for control strategy validation, a simple initial displacement holder was devised to create a static displacement initial condition. It functions in a way such that the material point $s = 0.95$ m (adjacent to mass 1) was displaced by 20 mm and

held by the device. When the experiment started, the device was manually released and triggered the system to operate. The beam started to vibrate and the control mechanism started to take action.

4.2.11 Complete system

The overall system built after design implementation is shown in Fig. 4.6.

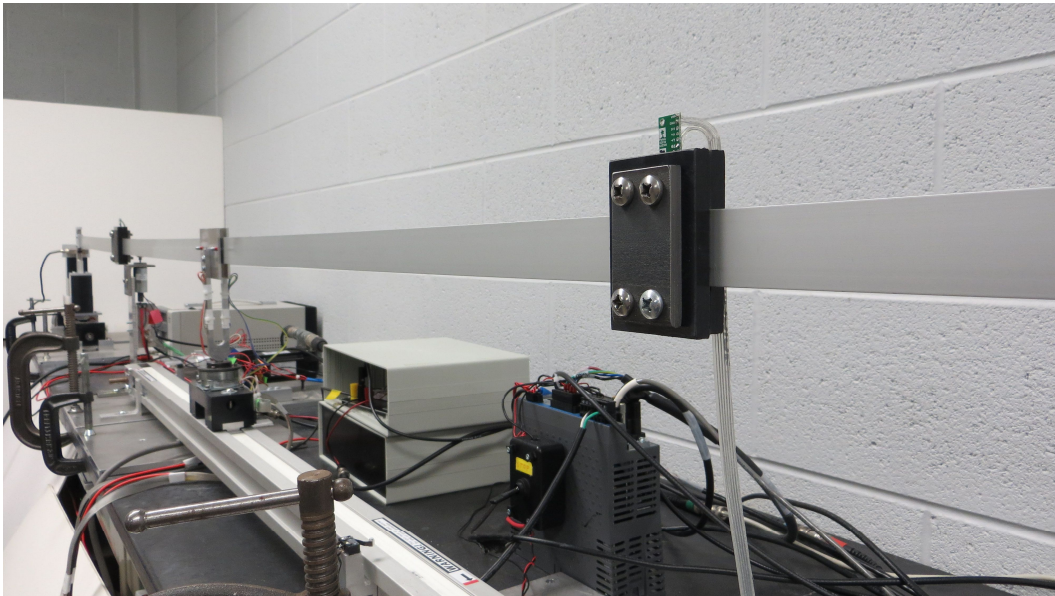


Figure 4.6 Complete experiment system built after design implementation.

4.3 Experiment results

4.3.1 Free vibration

The experiment investigation starts from the free vibration case. The beam was given the initial condition that the material point $s = 0.95$ m (adjacent to mass 1) was displaced by 20 mm. After

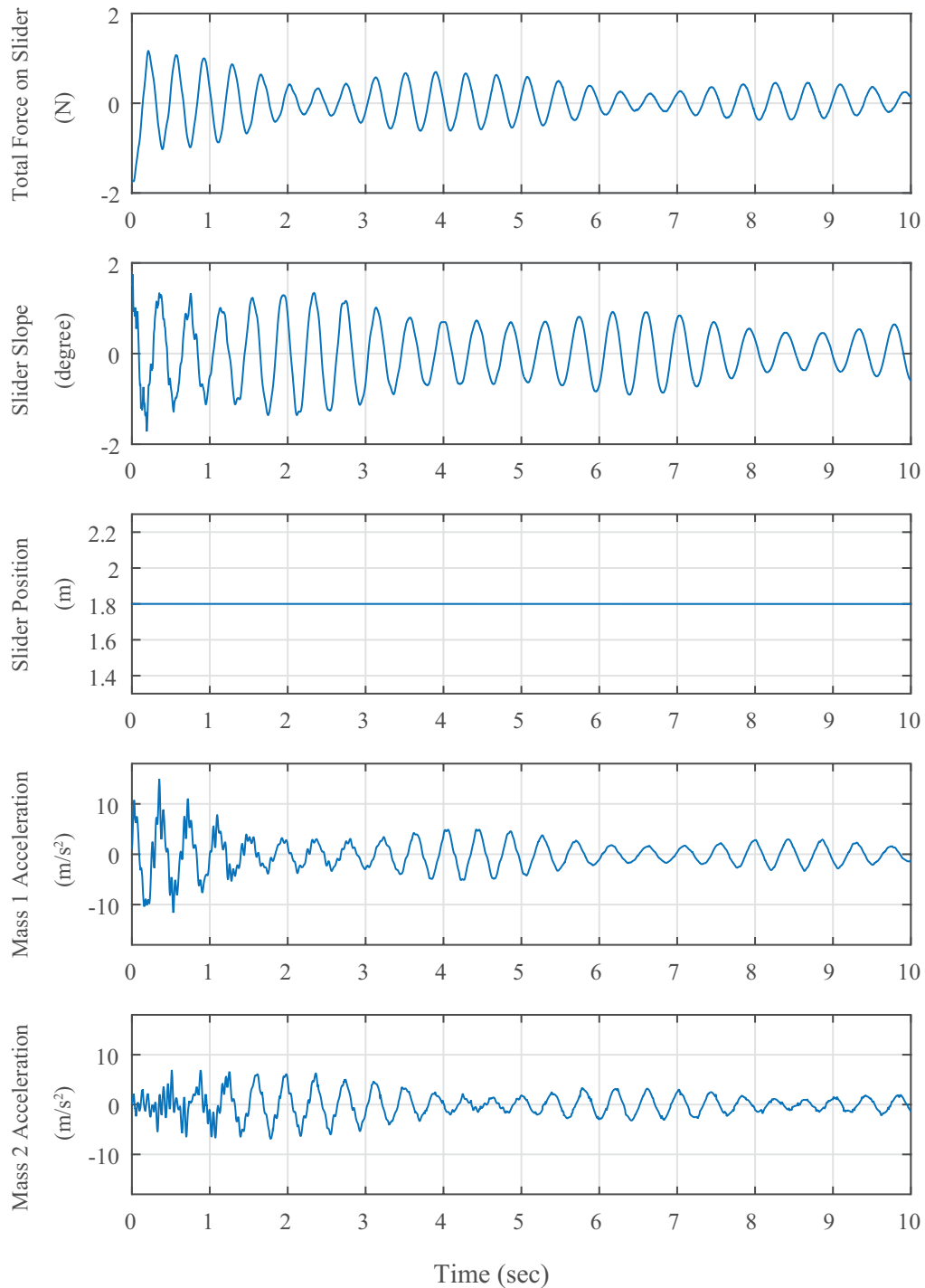


Figure 4.7 Experiment results of the system in free vibration (time domain). Plots from top to bottom: total force measured on the slider, applied by the beam; slider slope, or rotational displacement; slider position, measured from left end of the beam; acceleration of mass 1; acceleration of mass 2.

being released from its initial displacement, the beam underwent free vibration. During this process there was no sliding motion, but the slider was allowed to rotate freely.

Five quantities were directly measured and recorded, as shown in Fig. 4.7. They are 1) total force sensed on slider, applied by the beam with the direction normal to the beam surface; 2) slope of the slider, indicating the rotational displacement at the contact point; 3) position of the slider, measured from left end of the beam, indicating the linear displacement of the slider; 4) acceleration of mass 1; 5) acceleration of mass 2.

The following observation can be made. The slider position stayed constant since no sliding motion was allowed. Quantities such as total force on slider, slider slope and accelerations of the masses all exhibited a dominant frequency component around 2.5 Hz. A low frequency envelope, typically referred to as beats, was formulated on the amplitude of the dominant 2.5 Hz vibration. The envelope can be counted as 4 ~ 5 sec for its half period. High frequency components appeared at the beginning of the dynamic history, which can be clearly seen in the first 1 sec of the slider slope plot, and the first 2 sec of the mass acceleration plots. The high frequency dynamics were then dissipated, leaving a smoother dynamic curve as time progressed.

As the most relevant quantities to transverse vibration of the beam, the mass accelerations can be evaluated as follows. Mass 1, located less than 30 mm to the disturbance source point, started at the level of 10 m/s^2 . It rose to 15 m/s^2 around 0.3 sec. At 10 sec, mass 1 acceleration decreased to $\approx 2 \text{ m/s}^2$, 20% of the initial level. Mass 2, not directly excited by the disturbance, had the initial acceleration of 0. As the vibration propagated from mass 1 and reached mass 2, acceleration of mass 2 increased to its maximum value of 8 m/s^2 around 0.5 sec. At 10 sec, mass 2 also had the acceleration of $\approx 2 \text{ m/s}^2$, a sign indicating that the vibration energy is evenly distributed on two sides of the beam.

To better understand the free vibration dynamics of the system, a Fast Fourier Transform (FFT) analysis was performed to inspect the frequency domain. The analysis was performed on four quantities out of the recorded five quantities in Fig. 4.7. The constant slider position was not analyzed since the result would be trivial. Shown in Fig. 4.8, vibration information recorded by the

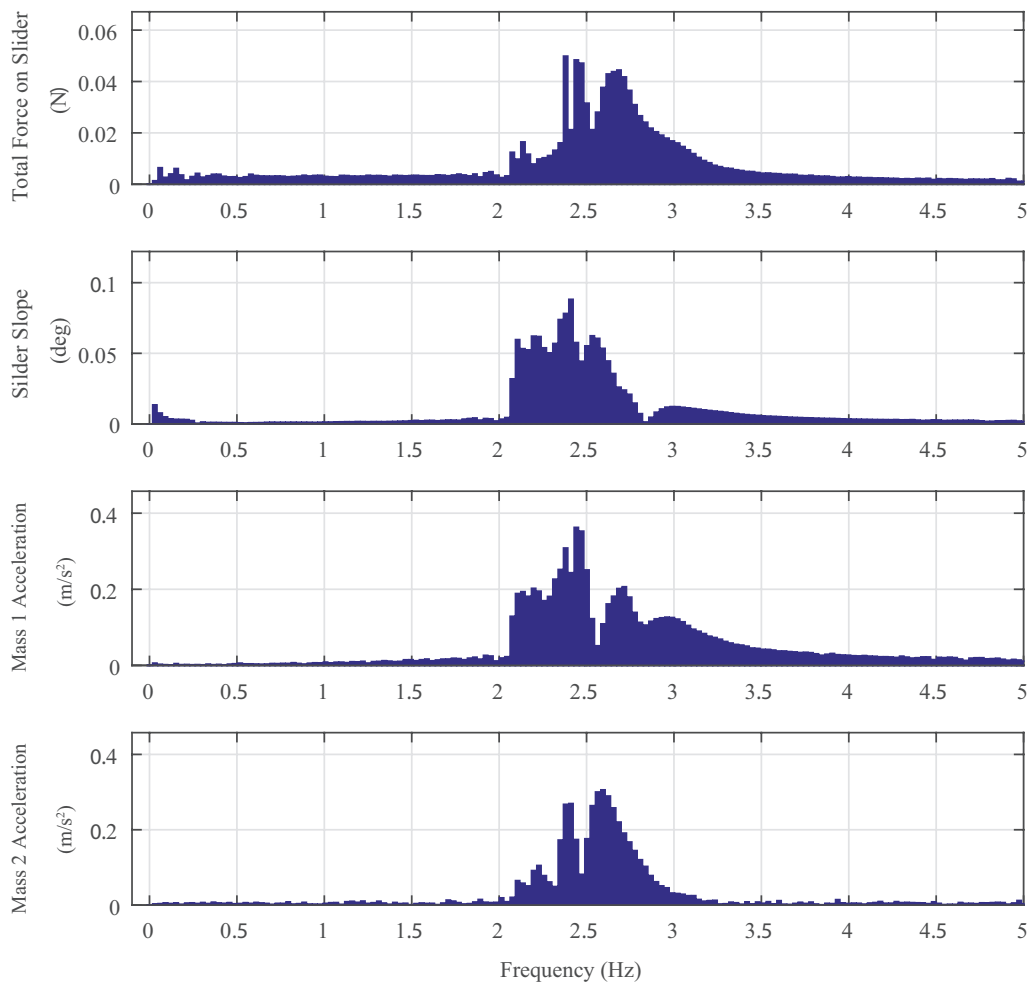


Figure 4.8 Experiment results of the system in free vibration (frequency domain). Plots from top to bottom: total force measured on the slider, applied by the beam; slider slope, or rotational displacement; acceleration of mass 1; acceleration of mass 2.

sensors has been converted in frequency domain. For all four quantities, one can tell from the plots that the energy mainly exists in the frequency range between 2 Hz and 3.5 Hz. Interestingly, all four plots show two neighboring frequency peaks centered around 2.5 Hz. The difference between the two peaks is 0.2 ~ 0.3 Hz. This explains the beats apparent in the time domain, shown in Fig. 4.7, for the beats are indeed caused by superimposing two frequencies that are close to each other. And the half period of the beats, measured before as 4 ~ 5 sec, agrees with the difference between the frequency peaks ($1/0.25 \text{ Hz} = 4 \text{ sec}$).¹

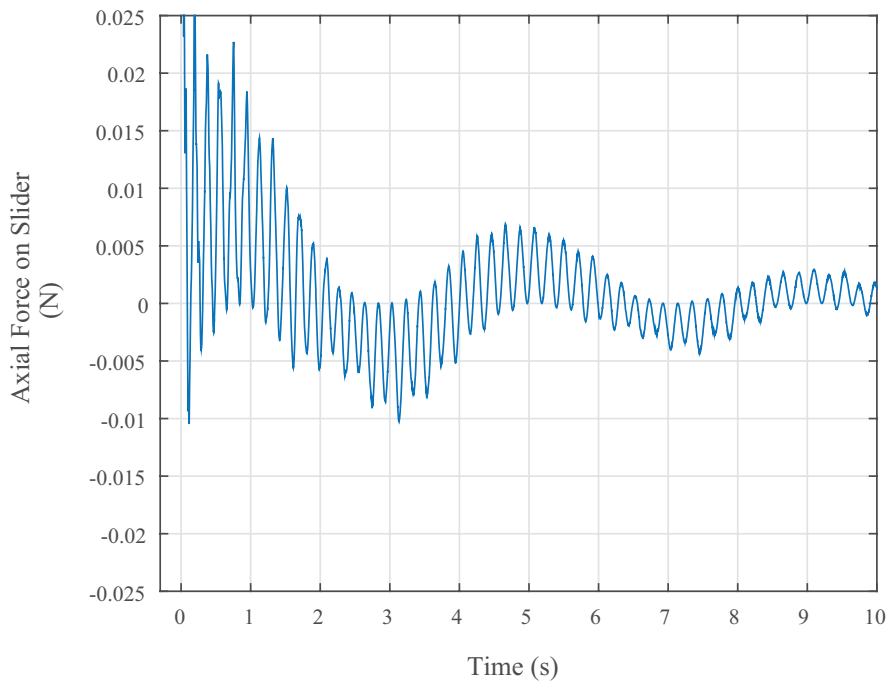


Figure 4.9 Axial force on slider, post-processed from experiment results of the system in free vibration (time domain).

The key information needed for the purpose of vibration control is the axial force. This quantity was derived from measurements by multiplying the total force on the beam and the slider slope. Fig. 4.9 shows a plot of the axial force through post-processing the measurement data of the free

¹Given two sine waves of unit amplitude and close frequencies of f_1 and f_2 , when added together, the combined wave is $\cos(2\pi f_1 t) + \cos(2\pi f_2 t) = 2 \cos(2\pi \frac{f_1 - f_2}{2} t) \cos(2\pi \frac{f_1 + f_2}{2} t)$, where the beating frequency is $|\frac{f_1 - f_2}{2}|$.

vibration case.

The processed axial force clearly exhibits two frequency contents, one around 0.2 Hz and the other around 5 Hz. This can be verified by the FFT analysis shown in Fig. 4.10. Different from quantities in Fig. 4.7, the low frequency vibration (0.2 Hz) of the axial force existed independently, and did not result from beating. Instead, this frequency was superimposed on the higher frequency component of 5 Hz. This is very important for the control scheme to be apply, as the low frequency is easy for the mechanical part of the control system to react and to follow.

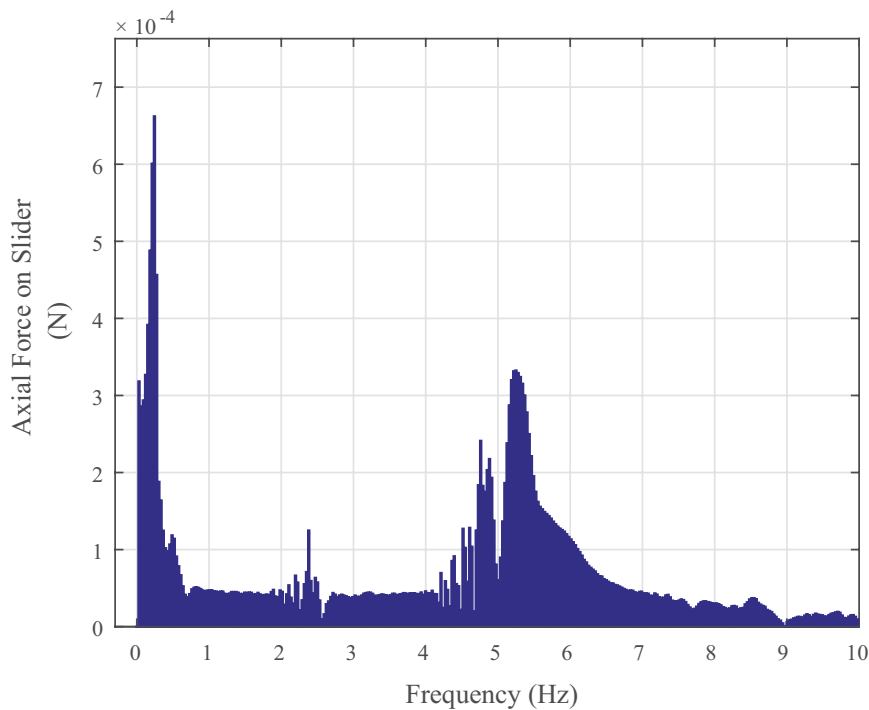


Figure 4.10 Axial force on slider, post-processed from experiment results of the system in free vibration (frequency domain).

The higher frequency around 5 Hz, is twice of the frequency of the quantities in Fig. 4.7. This again verifies that when the axial and transverse vibrations are nonlinearly coupled, the axial vibration doubles the frequency of the transverse vibration.

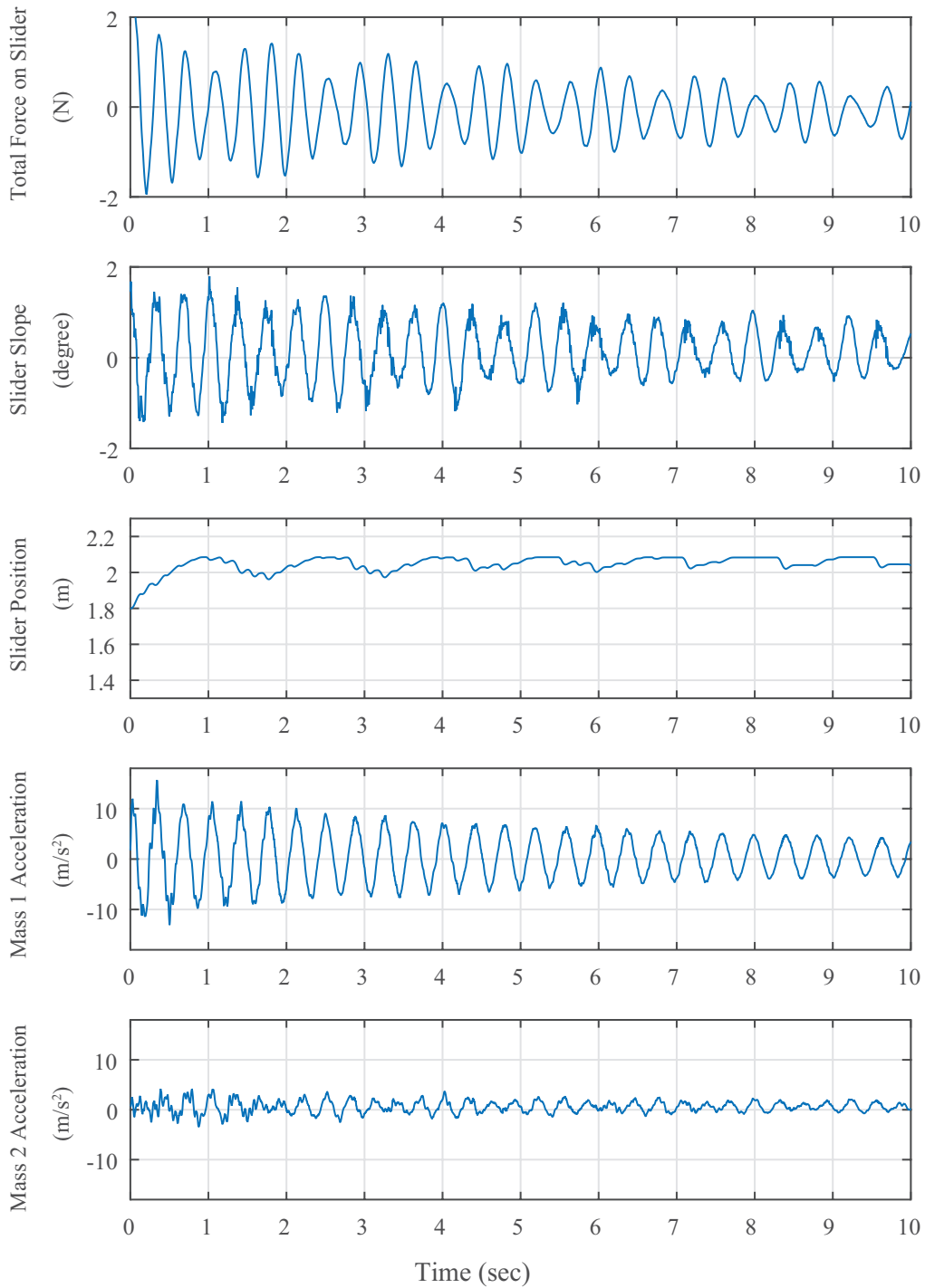


Figure 4.11 Experiment results of the system under sliding control only. Plots from top to bottom: total force measured on the slider, applied by the beam; slider slope, or rotational displacement; slider position, measured from left end of the beam; acceleration of mass 1; acceleration of mass 2.

4.3.2 Performance of control employing sliding mechanism only

The first vibration control method applied was the control scheme using sliding mechanism only. Again, five quantities were directly measured and recorded in the experiment, as shown in Fig. 4.11. They are presented in the same form as in Fig. 4.7.

Vibration of the beam and controlled motion of the slider started after release from the initial displacement configuration, i.e., material point $s = 0.95$ m (adjacent to mass 1) displaced by 20 mm. Variation of the total force on slide exhibited moderate beating but not as obvious as in Fig. 4.7. The half period of the beating amplitude envelope can be counted as ≈ 1.5 sec. This pattern also vaguely appeared in the slider slope plot. Likewise, vibration of period ≈ 1.5 sec can be observed in the slider position plot, corresponding to a motion frequency of 0.6 Hz. However, this beating behavior can hardly be detected in the acceleration plots of the two masses, where the single dominant frequency is between 2 Hz and 3 Hz. It can be observed that the frequency of mass 1 acceleration decreased slightly from ≈ 3 Hz in the first 1 sec to ≈ 2.3 Hz towards the end of 10 sec. This decrease in frequency can be explained by the fact that the effective beam length connected to mass 1 increased as the slider motion overall was moving towards mass 2. High frequency components appeared in the first 1 sec of the mass 1 acceleration, and the first 2 sec of the mass 2 acceleration. The high frequency dynamics were then dissipated, leaving a smoother dynamic curve in the acceleration plots as time progressed.

Acceleration of mass 1 started at the level of 10 m/s^2 . It rose to 16 m/s^2 around 0.3 sec. At 10 sec, mass 1 acceleration decreased to $\approx 4 \text{ m/s}^2$, 40% of the initial level. Compared to the free vibration case in which the value became 2 m/s^2 , here the acceleration level is larger, defeating the purpose of vibration reduction. Mass 2, not directly excited by the initial disturbance, had the initial acceleration of 0. As the vibration propagated from mass 1 and reached mass 2, acceleration of mass 2 increased to its maximum value of 4 m/s^2 around 0.4 sec. At 10 sec, mass 2 had the acceleration of $\approx 1.5 \text{ m/s}^2$, slightly decreased compared to the free vibration case (2 m/s^2 at 10 sec).

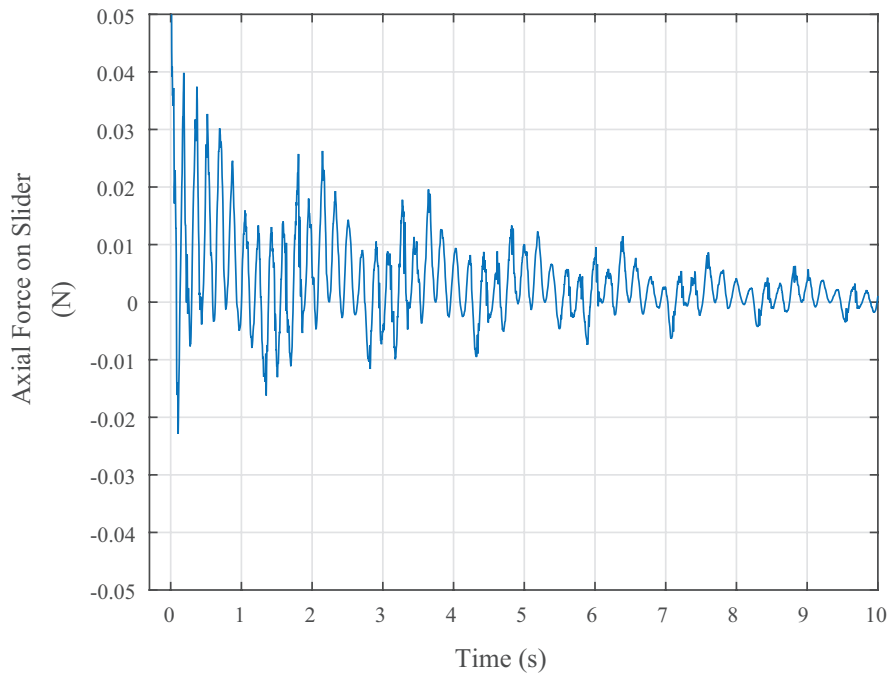


Figure 4.12 Axial force on slider in time domain, processed from measurements of total force on slider and slider slope .

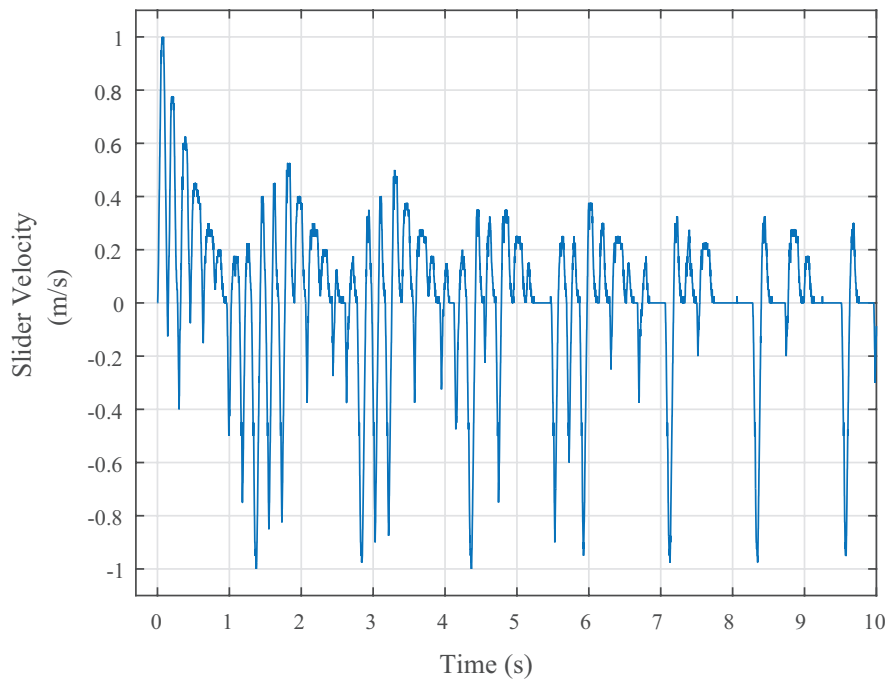


Figure 4.13 Slider velocity in time domain, processed from the measurement of slider position.

The slider moved at the maximum velocity of 1 m/s. A span length of 0.55 m was used, which set the material boundary on the beam for the sliding motion. The slider velocity was set to be zero if it hit the material boundary and continued with the direction of attempting to go over the boundary, as the algorithm depicted in Fig. 3.5. One can clearly see the upper material boundary being reached in Fig. 4.11. The axial force on the slider, which directly determined the slider motion in the algorithm, was extracted and presented in Fig. 4.12. For most of the time in the 10 sec interval, the axial force on the slider was in the positive X-direction, or towards the right end of the beam. This can be understood as the vibration was propagating out from the initial disturbance; the wave had the tendency of pushing the slider away from the source of disturbance, as the design intent of the algorithm. Slider velocity is plotted in Fig. 4.13. As the slider velocity was controlled to move in the same direction as the axial force on the slider, it reduced the energy that flowed through the slider to the other side of the beam where mass 2 is located. This explains why the acceleration on mass 2 was much smaller than the acceleration of mass 1, and in general smaller than the same quantity in the free vibration case. This also gave the slider less chance to move back in negative direction to the mass 1 side, because the energy was mostly kept on the mass 1 side, leaving the mass 2 side not enough energy to compete.

As proposed in Section 3.4, this scheme employs a low pass filter in the feedback loop, to ease the bandwidth requirement of the mechanical hardware. Knowing from the free vibration analysis that most of the vibration energy of the system stays below 10 Hz (Fig. 4.8 and Fig. 4.10), the low-pass filter used the time constant of $\tau = 0.01$ sec, corresponding to the bandwidth of $\frac{1}{2\pi\tau} = 16$ Hz. Post FFT analysis of axial force on slider was performed and presented in Fig. 4.14, and the analysis on slider velocity in Fig. 4.15. In both FFT results the DC values were omitted. The energy of axial force was lumped in two frequency ranges, one below 1 Hz, the other in the range of 5 ~ 7 Hz. Since the bandwidth of the slider velocity was reasonably set to be 16 Hz, the slider had no problem effectively reacting to the feedback information.

Although the control scheme was carried out as designed, the vibration does not seem to be effectively suppressed by the sliding mechanism. This could be explained as that the direct energy

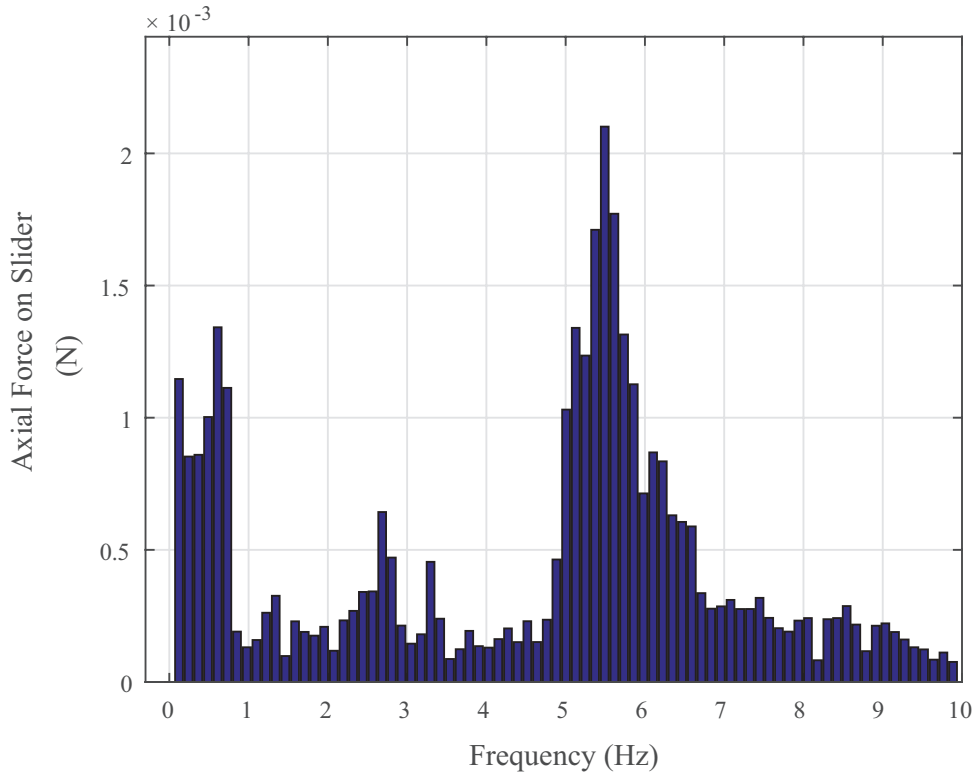


Figure 4.14 Axial force on slider in frequency domain.

removal rate by the slider may not be fast enough to create a meaningful difference compared to the free vibration case. Other control schemes need to be applied.

4.3.3 Performance of control employing stiffness variation mechanism only

The control strategy employing stiffness variation was investigated. This mechanism, as our first proposed vibration control strategy in Chapter 2, was implemented here in the experiment by adding onto the slider a clamping mechanism that has an on/off locking capability. This clamping device, implemented using an electromagnetic brake, can constrain the slope or the rotational displacement around the contact point. By locking/releasing the clamping device, a on/off joint is then created similar to the method described in Section 2.3, but with the difference that the joint works on a continuous beam and it can change its position by sliding.

The threshold for the on/off clamping brake to be activated was set to be 1° , meaning that the

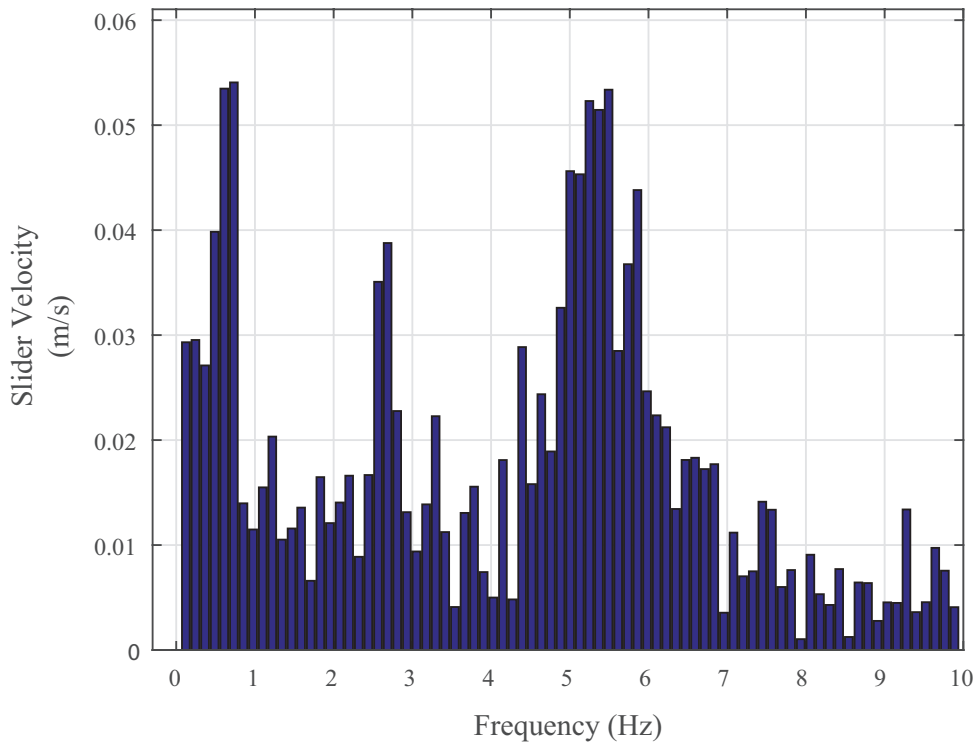


Figure 4.15 Slider velocity in frequency domain.

brake was activated and applied a rotational constraint when the encoder measured that the slope at the contact point fell below 1° . For each action, the clamping brake was kept activated for 0.05 sec, locking the slope during this time interval. It was then deactivated and released the slope for another 0.05 sec. After that the clamber waited for the next instance of activation and the cycle went on. In this experiment the slider had no translational motion. Therefore, the control employs stiffness variation method only.

Results are shown in Fig. 4.16. Brief pauses can be seen in the slider slope plot, as the result of activating the clamber. The immediate effect that activating the clamber each time had was the generation of high frequency vibrations. This can be seen in the acceleration plots. As explained in Chapter 2, the energy of the high frequency vibration was shifted from low frequency vibration. The redistribution of vibration energy in frequency domain is the results of stiffness variation. The vibration suppression was enhanced by internally damping out the high frequency vibration at a

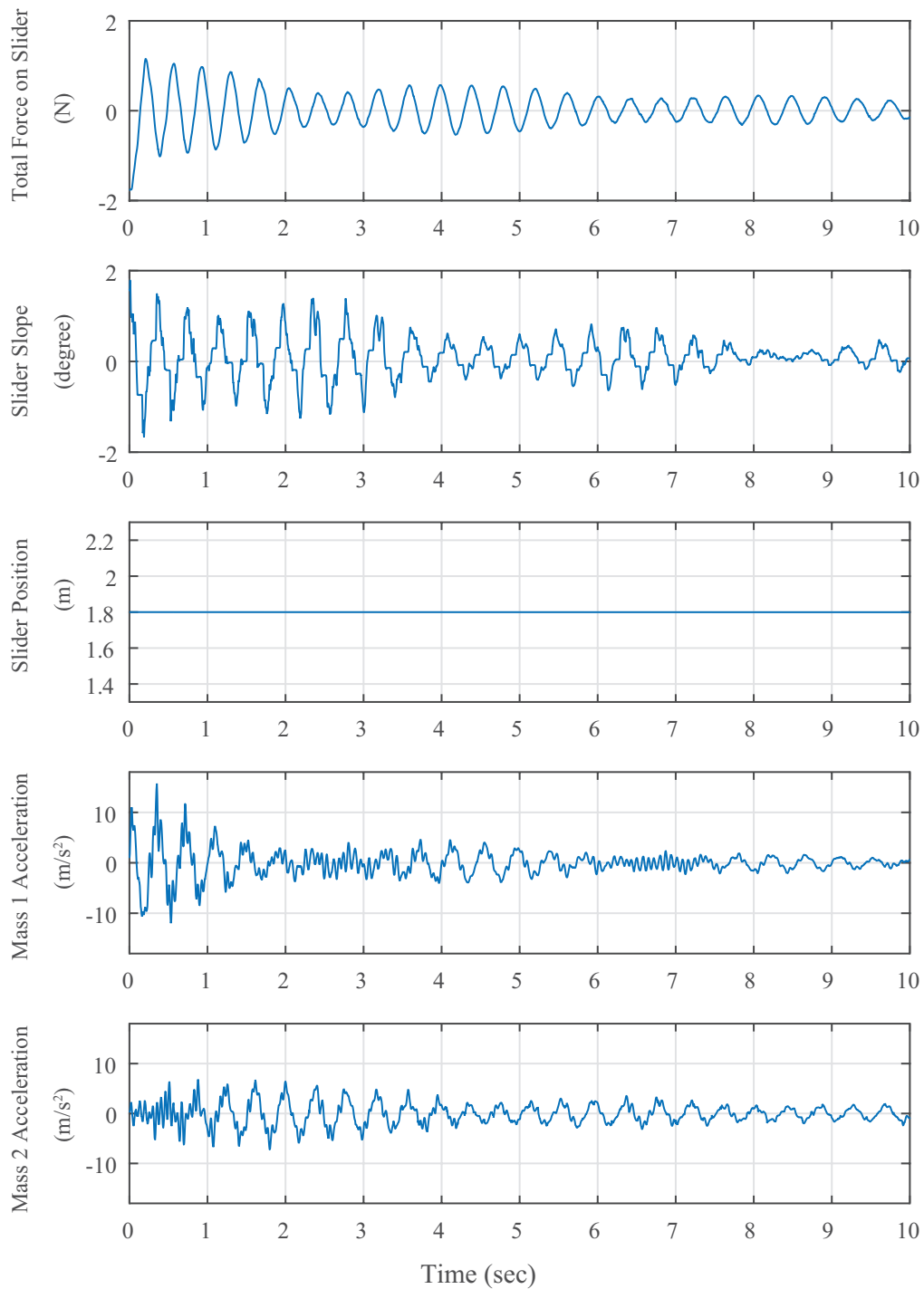


Figure 4.16 Experiment results of the system under stiffness variation control only. Plots from top to bottom: total force measured on the slider, applied by the beam; slider slope, or rotational displacement; slider position, measured from left end of the beam; acceleration of mass 1; acceleration of mass 2.

faster rate. As the beneficial outcome, the acceleration of mass 1 started at the level of 10 m/s^2 . At 10 sec, it decreased to $\approx 1 \text{ m/s}^2$, 10% of the initial level. Compared to the free vibration case in which the value became 2 m/s^2 , here the acceleration level was suppressed by an extra 10%. Mass 2, not directly excited by the initial disturbance, had the initial acceleration of 0. As the vibration propagated from mass 1 and reached mass 2, acceleration of mass 2 started to increase and vary. At 10 sec, mass 2 had the acceleration of $\approx 2 \text{ m/s}^2$, almost the same compared to the free vibration case.

Performance of control employing the stiffness variation mechanism showed a moderate vibration suppression effect on mass 1 but no effect on mass 2. Considering only one on/off joint was used in the structure, this result is not surprising. But room for improvement needs to be explored.

4.3.4 Performance of control combining stiffness variation and sliding mechanism

As described before, stiffness variation was implemented using a clamper on the slider that can be activated/deactivated as an on/off joint. In the following experiment, the sliding motion was independent from the activating/deactivating operation for stiffness variation, meaning that the slider could still move regardless of the clamper status. The slider motion was only determined by the algorithm that takes the computed axial force as the main input.

Using the same setting of stiffness variation and sliding control, the results of combining the two methods are shown in Fig. 4.17. The sliding motion has the direction controlled by the algorithm originally designed in Section 3.4, therefore referred to as "forwarding sliding", to be differentiated from the "reverse sliding", which will be investigated later.

It is interesting to see from the slider position plot that the slider motion went on in a positive direction almost monotonically until it reaches the material boundary and stopped on it after just 2 sec. One can understand this because the vibration energy is not evenly distributed on both sides of the slider. The motion of sliding plus the on/off stiffness variation provided by the clamper somehow blocked the vibration propagation over the contact point from the side of mass 1 to the

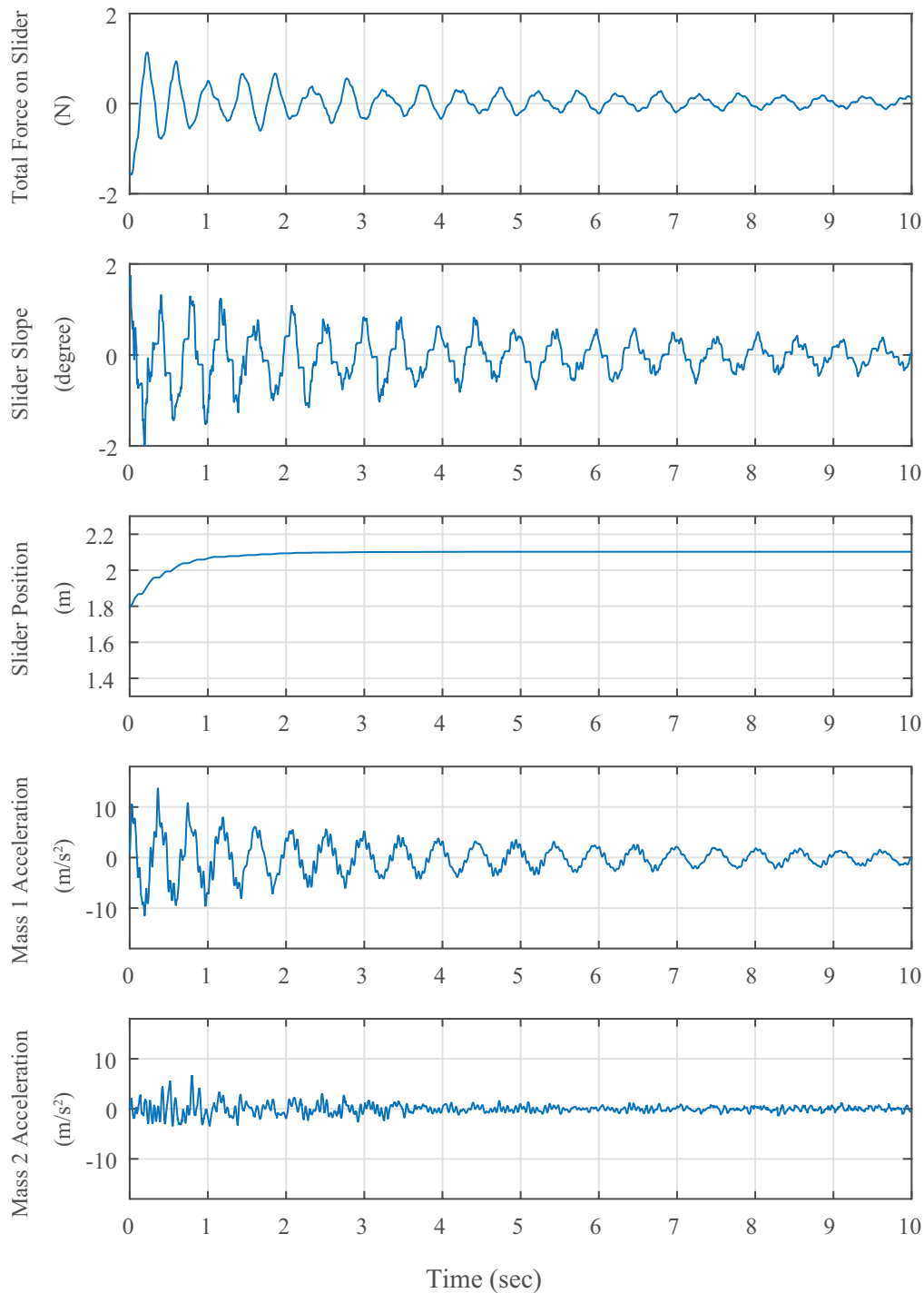


Figure 4.17 Experiment results of the system under combined control of stiffness variation and forward sliding mechanism. Plots from top to bottom: total force measured on the slider, applied by the beam; slider slope, or rotational displacement; slider position, measured from left end of the beam; acceleration of mass 1; acceleration of mass 2.

side of mass 2. That explains that the mass 2 side of the beam lack the energy to compete with the mass 1 side and to push the slider back in negative direction. The stiffness variation by the clamper still continued to be applied after the translational sliding motion stopped.

The acceleration of mass 1 started at the level of 10 m/s^2 . At 10 sec, it decreased to $\approx 1.5 \text{ m/s}^2$, 15% of the initial level. Compared to the free vibration case in which the value became 2 m/s^2 , here the acceleration level was suppressed by an extra 5%. Mass 2, not directly excited by the initial disturbance, had the initial acceleration of 0. As the vibration propagated from mass 1 and reached mass 2, acceleration of mass 2 started to increase and vary. At 10 sec, mass 2 had the acceleration of $\approx 0.8 \text{ m/s}^2$, suppressed by an extra 12% compared to the free vibration case.

Performance of control combining stiffness variation and the forward sliding mechanism show a moderate vibration suppression effect on both mass 1 and mass 2. In an effort to improve the performance using the current experimental configuration, the combination of stiffness variation and reverse sliding was also explored. This strategy also combines stiffness variation and the sliding mechanism. But instead of sliding according to the algorithm presented before, the sliding motion was carried out in the reverse direction.

Results are shown in Fig. 4.18. Since the algorithm was modified, the slider position plot shows the sliding is taking the opposite motion compared to Fig. 4.17. The moment after the beam was released from the initial condition, the slider quickly moved towards mass 1, where the initial disturbance occurred. The slider stopped after $\approx 3 \text{ sec}$ when it reached the material boundary. The stiffness variation by the clamper still continued to apply after the translational sliding motion stopped.

The effect of vibration suppression was significant. Both mass 1 and mass 2 accelerations decreased to $\approx 0.5 \text{ m/s}^2$, compared to 2 m/s^2 in the free vibration case. This gives the best results among all control strategies. This shows that the new strategy of combining stiffness variation and reverse sliding effectively pushed the vibration energy into high frequency region and created much faster energy decay rate through internal material damping. One can observe from the acceleration plots that high frequency components continuously showed up and the curves were never smooth.

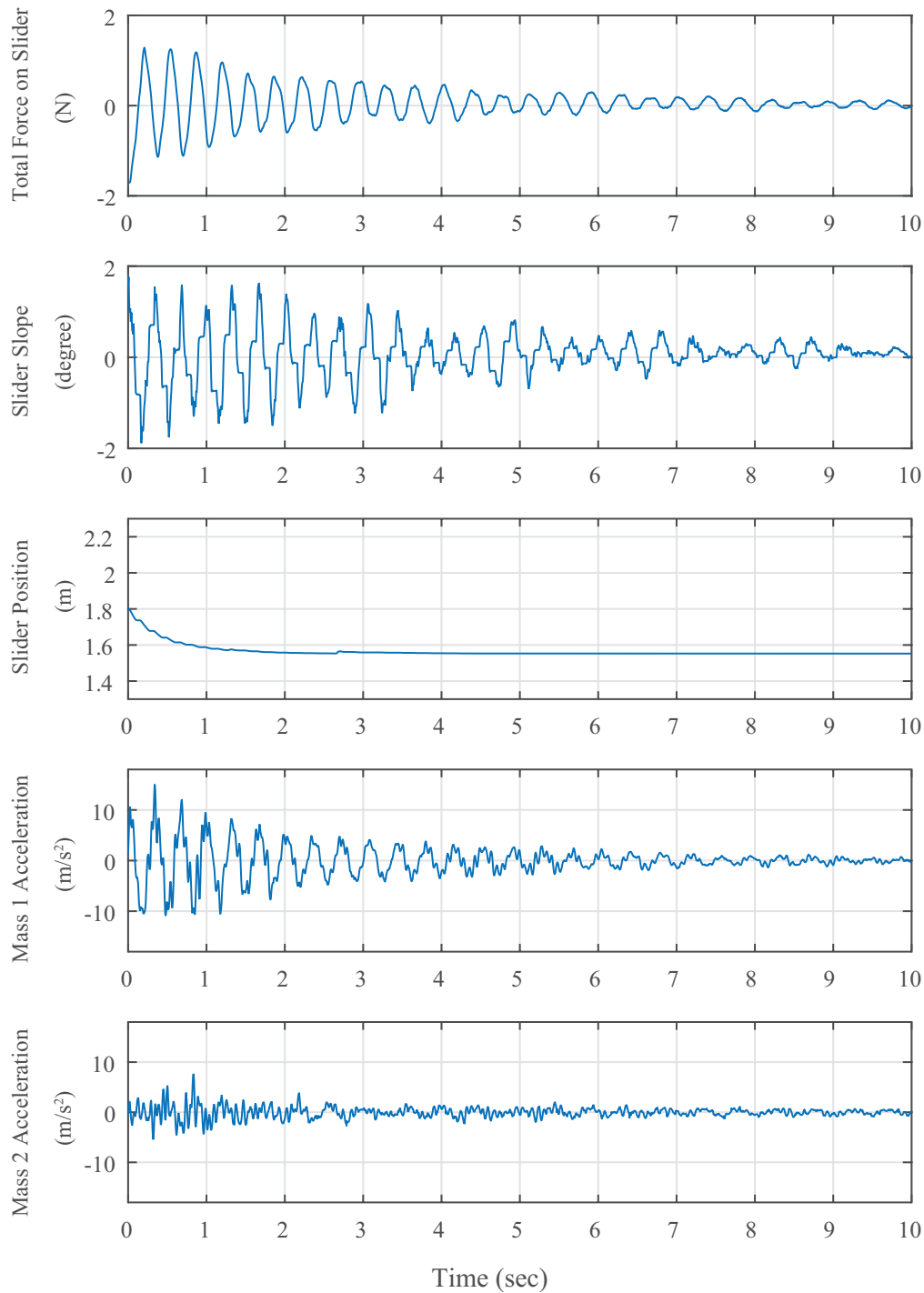


Figure 4.18 Experiment results of the system under combined control of stiffness variation and reverse sliding mechanism. Plots from top to bottom: total force measured on the slider, applied by the beam; slider slope, or rotational displacement; slider position, measured from left end of the beam; acceleration of mass 1; acceleration of mass 2.

Table 4.2 Comparison of performance of different control strategies. All relative values were computed using the mass 1 initial acceleration as reference.

Control Condition	Mass 1 Relative Accel at 10 sec	Mass 2 Relative Accel at 10 sec
Free Vibration	20%	20%
Sliding Only	40%	15%
Stiffness Variation Only	10%	20%
Forward Sliding and Stiffness Variation	15%	8%
Reverse Sliding and Stiffness Variation	5%	5%

The energy redistribution was very effective that the total energy including the energy added by reverse sliding itself was dissipated all together quickly enough. A comparison of all experiment cases are summarized in Table 4.2. In the table the percentage was computed using the mass 1 initial acceleration of 10 m/s^2 as 100% reference.

4.3.5 Discussion

Experiments show various vibration suppression effects using different control methods. The most effective method, which combines stiffness variation and sliding mechanism, was predicted in Chapter 3. This method applies stiffness variation through a clamper while controls the slider to move in a reverse way. It constantly adds energy directly but also excites high frequency vibration in the system. Overall, through internal damping enhanced by stiffness variation, the net effect is that the decay rate of the system vibration is significantly higher than in other cases such as forward sliding.

Investigation with numeric simulation in Chapter 3 revealed the important relationship between the two energy removal mechanisms. These two mechanisms are 1) direct energy reduction through sliding and 2) indirect energy reduction through material damping. It was verified in the experiment that given the moderate damping rate of the system, direct energy removal through sliding motion did not perform as the dominant factor of vibration suppression. The major portion of energy dissipation has to rely on internal material damping. To maximize the damping

effect, sliding motion can be used as a secondary role to facilitate damping process. Together with stiffness variation implemented using the on/off clamper which does not change energy directly, sliding, especially reverse sliding, effectively reshapes the energy distribution in the frequency domain. It keeps funneling the energy into high-frequency domain where damping effectively turns the vibration energy into heat.

This scenario is similar to the system presented in Chapter 2, where the damping level is also moderate. In Chapter 2 vibration suppression is achieved through stiffness variation alone, at the price of employing multiple actuators. As the number of controlled hinges or springs decreases, vibration suppression gets less and less efficient. As in the experiment, with sliding mechanism added, actuators and sensors are all lumped on one sliding device. With a similarly moderate damping level, the same vibration suppression target can be achieved using less actuators but more sophisticated sensor design, signal processing and control logic.

It is fairly clear that the control strategy needs to be formulated differently towards systems with different damping levels. For lightly damped structures, it is better to use direct energy removal method such as sliding, as shown in Chapter 3. For moderately damped structures, damping facilitated by sliding and/or stiffness variation seems to be a better choice. For heavily damped structures, which are not within the scope of this thesis, traditional treatment using passive method such as optimizing the damper location should suffice as an affordable and practical solution.

CHAPTER 5

SUMMARY AND FUTURE WORK

Tension-aligned structures have shown great potential of providing mass efficiency, ease of transport and a high-degree of accuracy. Such features are highly valuable in space-based applications. To study the vibration suppression strategy in simple tension-aligned structures, models of structural dynamics were built with careful consideration of the tension's role in the structural vibration behavior. Analysis showed that the tension enters the vibration dynamics mainly through geometric nonlinearity. Several models illustrated in this study all share the similar bow-string like topology. They are comprised of a support structure in compression, which provides tension to sensor surfaces via the connections at ends. In the examples used, the support structure varies from absolutely rigid object, to a curvedly deformed rod, and further to a three-dimensional, more realistic, truss-like space structure. The sensor surface under tension ranges from a simple beam to hinged panel arrays.

Two different control strategies were proposed and applied on those structure models. The first strategy is vibration suppression through stiffness variation. This semi-active method sequentially applies and removes constraints in the structure. The process varies the system stiffness and funnels vibration energy from low-frequency where damping rate is low to high-frequency modes where internal material damping rate is naturally high. By leveraging material damping, energy is then indirectly but effectively dissipated. The second strategy, an active method, employs a sliding mechanism where the constraint force is measured in real time and used as feedback to prescribe the motion of the slider itself. The prescribed slider motion keeps doing negative work to the structure thereby vibration energy gets directly removed. This strategy uses a straightforward idea and very few sensors. It requires more sophisticated actuators and more powerful real-time computation.

Numeric results show that the two strategies work effectively to achieve the vibration sup-

pression goal. The stiffness variation method was demonstrated on both two-dimensional and three-dimensional numeric models where moderate material damping was presented. Compared to free vibration (no control), the control method provided significantly faster energy decay. The concept of modal disparity was investigated in the process to further the understanding of the relationship between stiffness variation and control efficacy. The strategy using sliding mechanism was validated numerically using a one-dimensional nonlinear beam model where light damping was presented. Several filtering and signal processing techniques were studied to address the practical issues such as limited actuator bandwidth. Overall the design idea of doing negative work by the slider to the structure met the expectation of successful vibration suppression. Furthermore, an experiment platform was built to test both control strategies in a realistic environment. It was found that to achieve the best vibration suppression results in a moderately damped beam structure, one shall combine both control strategies in a way such that the stiffness variation method serves as a primary role, facilitated by the sliding mechanism. This combination delivered the most effective result by leveraging the structural damping to the most.

All the numeric and experimental studies led to the conclusion that vibration control strategy needs to be formulated differently towards systems with a different damping level. For lightly damped structures, it is better to use direct energy removal method such as sliding. For moderately damped structures, damping facilitated by stiffness variation and/or a sliding mechanism seems to be a better choice. For heavily damped structures, which are not within the scope of this study, traditional treatment using passive methods should be an affordable and practical solution.

In the numeric investigation of the sliding mechanism, the contact problem showed to be a challenge for it cost a great deal of computation time and power. This numeric issue comes from the root that if the contact problem is formulated using Lagrange multipliers, a DAE system emerges and needs to be tackled using special solvers. On the other hand, if the problem is formulated using a penalty method, a very stiff ODE system then needs to be solved. Both seem to be expensive numerically. To fasten the simulation process of the sliding mechanism, more understanding of numeric method dealing with the contact problem needs to be gained. In the future study a better

numeric tool is essential to produce more investigation results by constructing more scenarios.

In the experimental study, a comprehensive approach was taken to combine two strategies in different ways to find the most efficient combination for vibration suppression. However, the search was still limited and not exhaustive. It could only be concluded that the best results so far came from the combination that was the best among the combinations that were tested. It is expected in the future study that an accurate and mathematical model could be developed to characterize the system dynamics under both control methods, especially to accurately capture the contact behavior and damping behavior. In that way an optimal control method combination search could be performed and the control results could be well predicted.

More studies need to be conducted and better understanding needs to be gained to develop reliable, robust and practical vibration suppression solutions, for tension-aligned structures to have greater application in space missions and in other fields.

BIBLIOGRAPHY

BIBLIOGRAPHY

- Adler, A., M. M. Mikulas, J. M. Hedgepeth, M. Stallard & J. Garnham. 1998. Novel phased array antenna structure design. In IEEE aerospace conference, Aspen CO.
- Barhorst, A. A. 2004. On the efficacy of pseudo-coordinates. part 1: Moving interior constraints. *International Journal of Non-Linear Mechanics* 39(1). 123–135.
- Bauchau, O. A. 2010. *Flexible multibody dynamics*. Springer.
- Clark, W. W. 2000. Vibration control with state-switching piezoelectric materials. *Journal of Intelligent Material Systems and Structures* 11(4). 263–271.
- Corr, L. R. & W. W. Clark. 2001. Energy dissipation analysis of piezoceramic semiactive vibration control. *Journal of Intelligent Material Systems and Structures* 12(11). 729–736.
- Diaz, A. R. & R. Mukherjee. 2006a. Modal disparity enhancement through optimal insertion of nonstructural masses. *Structural and Multidisciplinary Optimization* 31(1). 1–7.
- Diaz, A. R. & R. Mukherjee. 2006b. Topology optimization problem in control of structures using modal disparity. *ASME Journal of Mechanical Design* 128(3). 536–541.
- Diaz, A. R. & R. Mukherjee. 2008. Optimal joint placement and modal disparity in control of flexible structures. *Computers and Structures* 86(13-14). 1456–1462.
- Dill, E. H. 1992. Kirchhoff's theory of rods. *Archive for History of Exact Sciences* 44(1). 1–23.
- Fang, J. & G. J. Lyons. 1996. Structural damping of tensioned pipes with reference to cables. *Journal of Sound and Vibration* 194(3). 891–907.
- Fischer-Cripps, A. C. 2007. *Introduction to contact mechanics*. Springer.
- Footdale, J. N., S. K. Jeon & T. W. Murphey. 2012. Static shape and modal testign of a deployable tensioned phased array antenna. In *53rd AIAA structures, structural dynamics, and materials conference*, .
- Hong, D. & G. Ren. 2011. A modeling of sliding joint on one-dimensional flexible medium. *Multibody System Dynamics* 26(1). 91–106.
- Issa, J., A. R. Diaz & R. Mukherjee. 2009. Energy dissipation in dynamical systems through sequential application and removal of constraints. *ASME Journal of Dynamic Systems, Measurement and Control* 131(2).
- Issa, J., A. R. Diaz, R. Mukherjee & S. W. Shaw. 2008. Modal disparity and its experimental verification. *Journal of Sound and Vibration* 311(3-5). 1465–1475.
- Issa, J., R. Mukherjee & S. W. Shaw. 2010. Vibration suppression in structures using cable actuators. *ASME Journal of Dynamic Systems Measurement and Control* 132(3).

- Jeon, S. K. & T. W. Murphey. 2012. Fundamental design of tensioned precision deployable space structures applied to an x-band phased array. In *53rd AIAA structures, structural dynamics, and materials conference*, .
- Jones, T. C., H. Bart-Smith, M. Mikulas & J. Watson. 2007. Finite element modeling and analysis of large pretensioned space structures. *Journal of Spacecraft and Rockets* 4(1). 183–193.
- Jones, T. C., J. J. Waston, M. Mikulas & H. Bart-Smith. 2008. Design and analysis of tension-aligned large aperture sensorcraft. In *49th AIAA structures, structural dynamics, and materials conference*, Schaumburg IL.
- Kemerley, R. T. & S. Kiss. 2000. Advanced technology for future space-based antennas. In *IEEE MTT-S international microwave symposium digest*, vol. 2, 717–720. Boston MA.
- Khalil, H. 2002. *Nonlinear systems*. Prentice Hall.
- Love, A. E. H. 1944. *A treatise on the mathematical theory of elasticity*. Dover Publications.
- Mikulas, M., T. Murphey & T. C. Jones. 2008. Tension-aligned deployable structures for large 1-d and 2-d array applications. In *49th AIAA structures, structural dynamics, and materials conference*, Schaumburg IL.
- Nudehi, S., R. Mukherjee & S. W. Shaw. 1992. Active vibration control of a flexible beam using a buckling-type end force. *ASME Journal of Dynamic Systems Measurement and Control* 128(2). 278–286.
- Onoda, J., T. Endo, H. Tamaoki & W. Watanabe. 1991. Vibration suppression by variable-stiffness members. *AIAA Journal* 29(6). 977–983.
- Onoda, J., T. Sano & K. Kamiyama. 1992. Active, passive, and semiactive vibration suppression by stiffness variation. *AIAA Journal* 30(12). 2922–2929.
- Perkins, N. C. 1990. Planar vibration of an elastica arch - theory and experiment. *ASME Journal of Vibration and Acoustics* 112(3). 374–379.
- Perkins, N. C. & C. D. Mote, Jr. 1987. Three dimensional vibration of a translating elastic cable. *Journal of Sound and Vibration* 114(2). 325–340.
- Popov, V. L. 2010. *Contact mechanics and friction: Physical principles and applications*. Springer.
- Ramaratnam, A. & N. Jalili. 2006. A switched stiffness approach for structural vibration control: Theory and real-time implementation. *Journal of Sound and Vibration* 291(1-2). 258–274.
- Rao, S. S. 2007. *Vibration of continuous systems*. Wiley.
- Sakamoto, H. & K. C. Park. 2006. Localized vibration isolation strategy for low-frequency excitations in membrane space structures. *Journal of Vibration and Acoustics: Transactions of the ASME* 128(6). 790–797.

- Shampine, L. F. & M. W. Reichelt. 1997. The matlab ode suite. *SIAM Journal on Scientific Computing* 18(1). 1–22.
- Shampine, L. F., M. W. Reichelt & J.A. Kierzenka. 1999. Solving index-1 daes in matlab and simulink. *SIAM Review* 41(3). 538–552.
- Spencer, A. J. M. 1980. *Continuum mechanics*. Longman Group Limited.
- Winslow, C. 1993. Space station freedom solar array design development. *IEEE Aerospace and Electronic Systems Magazine* 8(1). 3–8.
- Wittbrodt, E. 2006. *Dynamics of flexible multibody systems: Rigid finite element method*. Springer.